The Optical and Electronic Properties of Organic-Inorganic Hybrid Perovskites

Azarhoosh, Pooya

Awarding institution:
King's College London

The Optical and Electronic Properties of Organic-Inorganic Hybrid Perovskites

Pooya Azarhoosh

A thesis submitted in partial fulfilment
of the requirements for the degree of
Doctorate of Philosophy in Physics

Department of Physics
King's College London
United Kingdom
2017

Dedicated to my parents

Farhad and Farah

with eternal love and gratitude

Publications

The research carrier out for fulfilment of this dissertation has contributed to the following publications:

- "**Experimental and theoretical optical properties of methylammonium lead halide Perovskites**", A. M. A. Leguy, P Azarhoosh, M. I. Alonso, M. Campoy-Quiles, O. J. Weber, J. Yao, D. Bryant, M. T. Weller, J. Nelson, A. Walsh, M. van Schilfgaarde and P. R. F. Barnes, **Nanoscale, 2016,8, 6317**
- "**Research Update: Relativistic origin of slow electron-hole recombination in hybrid halide perovskite solar cells**", P. Azarhoosh, S. McKechnie, J. M. Frost, A. Walsh and M. van Schilfgaarde, **APL Materials, 2016, 4, 091501**
- "**Quasi-particle electronic band structure and alignment of the V-VI-VII semiconductors SbSI, SbSBr, and SbSeI for solar cells**", K. T. Butler, S. McKechnie, P. Azarhoosh, M. van Schilfgaarde, D. O. Scanlon and A. Walsh, **Appl. Phys. Lett., 2016, 108, 112103**
- "**A photon ratchet route to high-efficiency hybrid halide Perovskite intermediate band solar cells** *", J. M. Frost, P. Azarhoosh, S. McKechnie, M. van Schilfgaarde, A. Walsh, **arXiv:1611.09786**
- "**Dynamic Symmetry Breaking and Spin Splitting in Metal Halide Perovskites***", S. McKechnie, J. M. Frost, D. Pashov, P. Azarhoosh, A. Walsh, M. van Schilfgaarde, **arXiv:1711.00533**
- "**Reversible Hydration of $CH_3NH_3PbI_3$ in Films, Single Crystals, and Solar Cells**", A. M. A. Leguy, Y. Hu, M. Campoy-Quiles, M. I. Alonso, O. J. Weber, P. Azarhoosh, M. van Schilfgaarde, M. T. Weller, T. Bein, J. Nelson, P. Docampo, and P. R. F. Barnes, **Chem. Mater., 2015, 27 (9), 3397**

*These publications are yet to be peer reviewed.

Acknowledgements

I would like to firstly thank Prof. Mark van Schilfgaarde whose continuous encouragement and support made this thesis possible. Throughout my PhD, his never-ending enthusiasm and guidance drove me to challenge myself. Working with him has been a pleasure and for these reasons I shall be forever grateful.

I am also thankful to Dr. Scott McKechnie for his support and discussions, which made the past four years far more interesting and fruitful, I greatly appreciate our long and often divergent conversation. I am also thankful to Prof. Aron Walsh and Dr. Jarvist Frost for their inputs and valuable discussions, through our collaboration I have learned much and gained invaluable experience. I am hugely thankful to Dr. Dimitar Pashov for all his help and all that he has taught me.

Throughout my PhD I have been surrounded by the most amazing group of people. I could always rely on many people at King's College London to lighten my day and lend a hand when I needed it the most. I am grateful to D. Allen, K. Bozek, M. Caio, A, Le Marois, M. Caccin, M. Fulford, A. Vishna, G. Zanda, G. Peralta, M. Bieniek, L. Sponza, M. de Cesare, T. Hefler, A. Pithis, J. Heal et al.. I will forever treasure our friendship. I am thankful to J. Aluko, S. Dimitriadis, A. Lane, M. Ogunkolade, S. Popat for the adventures and making the past four years more enjoyable.

I want to thank J. Kilpatrick, M. Greys-Hues, R. Peake, J. French and L. van Shilfgaarde for their help and constant effort to ensure our ambitious projects become realities. I would especially like to thank Dr. P. Le Long who has saved my academic career from being short and fruitless on many occasions, I am grateful for him being a friend when I needed it most.

I am grateful to Chandni for standing by me and unconditionally supporting me. I thank her for her understanding and kindness, especially towards the end of my PhD.

Finally, I am forever in debt of my parents and brother without whom I would certainly not be where I am today. All of my achievements are because of their never-ending support and encouragement. Their guidance and understanding throughout my PhD is worth more than I can express.

Abstract

The primary focus of this thesis is the study of a novel family of materials known as organic-inorganic hybrid Perovskites (OIHP), which have recently demonstrated to possess remarkable photovoltaic efficiency. The fundamental properties of these materials related to photovoltaic (PV) applications are studied to characterise electronic and optical behaviours. An all-electron implementation of the Quasi-particle Self-consistent GW (QSGW) is used to perform first principles calculations. The quasi-particle energy bands are analysed for a number of Perovskites, to identify trends and characteristics within this family of materials, and to understand the dielectric response. The dielectric function and refractive index were studied for 4 OIHP and compared to experimental work carried out collaboratively with Leguy *et al.* [1]. It is found that the relativistic effects are extremely important in characterisation of these materials. The presence of strong spin-orbit interaction combined with significant internal electric fields yields anomalously large Rashba splitting of both valence and conduction states near the band edges. This significantly perturbs the electronic and optical properties of these materials. Such effects have not been previously investigated in the context of photovoltaic materials. The effect of the Rashba splitting on the radiative recombination lifetime of charge carriers is investigated. A model for reciprocal space trapping mechanism of carriers was developed and implemented within the Questaal package. The slightly indirect gap induced by Rashba splitting results in a strongly suppressed photoluminescence when compared to conventional III-V direct-gap semiconductors with an otherwise approximately similar band structure. Such suppression of the radiative recombination enhances the diffusion length and can significantly increase the power conversion efficiency of a solar cell.

Contents

List of Tables

List of Figures

Abbreviation

- BOA : Born-Oppenheimer approximation
- CB : Conduction band
- CBM : Conduction band minimum
- CP : Critical point
- DFT : Density functional theory
- DOS : Density Of States
- DSOC : Dresselhaus spin orbit coupling
- EQE : External quantum efficiency
- GGA : Generalised gradient approximation
- GS : Ground state
- GW : G(Green's function) W (Screened coulomb interaction)
- GWA : GW approximation
- JDOS : Joint density of states
- IQE : Internal Quantum efficiency
- KS : Kohn-Sham
- LDA : Local density approximation

- LHS : Left hand side
- MBPT : Many-body perturbation theory
- OIHP : Organic-Inorganic hybrid Perovskite
- PCE : Power conversion efficiency
- PSC : Perovskite solar cell
- QSGW : Quasi-particle self-consistent GW
- RHS : Right hand side
- SOC : Spin orbit coupling
- SOI : Spin orbit interaction
- VB : Valence band
- VBM : Valence band maximum
- VHS : van Hove singularity

Preface

Global Energy Demand and Production

The average global rate of energy consumption in 2015 was estimated to be 17.41TW. This value represents a 1% increase from 2014, it is also expected to continue to increase with growing global population, advances in technologies and their increased availability [2]. Currently around 85% of the global final energy demand is met through non-renewable sources such as coal, oil and natural gasses [3]. Such methods of energy production release immense amounts of CO_2 and in some cases additional gases which contribute to the greenhouse effect. Consequently the current level of CO_2 in the atmosphere is 40% higher than pre-industrial revolution; additionally the atmospheric levels of greenhouse gases, such as methane and nitrous oxide, have reached levels unprecedented in the past 800,000 years [4]. It is due to such findings that the Intergovernmental Panel on Climate Change (IPCC) has stated with a 95% confidence that the primary source of global warming is human activity [5].

The continuous depletion of limited oil reserves to meet this energy demands, along with the environmental consequence of such methods of energy productions are truly unsustainable. To be able to meet the global energy demand it is necessary to move away from traditional energy sources and find new sustainable renewable methods. Such paradigm shift in our methods of energy production is more important now than ever before.

Photovoltaic (PV) solar cells are a potential alternative to more traditional and unsustainable methods for large scale global energy production. These devices convert light directly into electricity without any emission and can use sun light as a fuel. The total solar energy incident on earth amounts to ≈ 174 PW, approximately 30% of this energy is absorbed or reflected by the upper atmosphere, leaving ≈ 121.8 PW incident on the surface of earth. This value is nearly

four orders of magnitude greater than the global energy demand. However, in 2015 below 2% of global electricity was produced through solar energy, corresponding to a 28.1% increase in the global capacity for solar energy from the 2014 to 2015 [3,6]. However there still remains an opportunity to significantly increase installation of PV solar cells and produce a major part of our energy demand through solar energy. This fact along with the environmental needs and the existence of a virtually endless source of energy has led to a huge surge in photovoltaic research and the solar cell market. The recent financial, academic and industrial attention has led to a 40% average increase in the global solar energy capacity over the past 5 years [3].

Established solar cell technologies such as mono-crystalline and poly-crystalline silicon which dominate the market have experienced negligible increase in their efficiencies over the past 20 years, reaching 25.8% and 22.3% respective records (shown in figure 2) [7]. To increase the global PV solar energy capacity there is a need for new, efficient and cheaper materials to challenge current commercial solar cells. The latest contenders for this position are a group of materials known as hybrid halide Perovskites. These organic-inorganic compounds were first introduced to the field of PV in 2009, since then they have experienced the most rapid increase in power conversion efficiency(PCE) among all PV technologies [7,8]. Due to the rapid progress in PCE and the potentials of Perovskites solar cells, these devices were selected as one of 2013 biggest scientific breakthroughs by both *Nature* and *Science* editors [9, 10]. As these materials have reached above 20% PCE in less than 10 years they have attracted a large amount of attention both from the academia and PV industries [11].

Photovoltaic Solar Cells

In semiconducting materials unlike metals the energy states available to electrons are separated by a gap. These energy states are separated into bands, once a band is completely full, it is inert and hence unable to conduct. For a material to be conducting electrons need to be present within bands which are only partially filled. This condition for conducting in semiconductors can be achieved by promoting an electron above the band gap to a state within the conduction band. As the bands above the gap are only minimally filled due to thermal energy, electrons can conduct. The empty states left within the valence band after promotion of an electron are referred to as a holes. Much like electrons, holes can transfer charge only within bands which are

partially filled by holes. Holes can be treated as particles with opposite charge to electrons. The excited charge carriers in semiconductors can be collected and used as electrical energy. This is the underlying process of a photovoltaic solar cell and was first demonstrated by Edmond Becquerel in 1839 [12].

In photovoltaic devices the excitation of electrons from the valence band to the conduction band is due to the absorption of photons emitted by the sun (or an alternative light sources). In such cases a photon of energy equal or higher than that of the band gap can be absorbed by an electron within the valence band; to conserve the total energy, the electron is promoted to the conduction band.

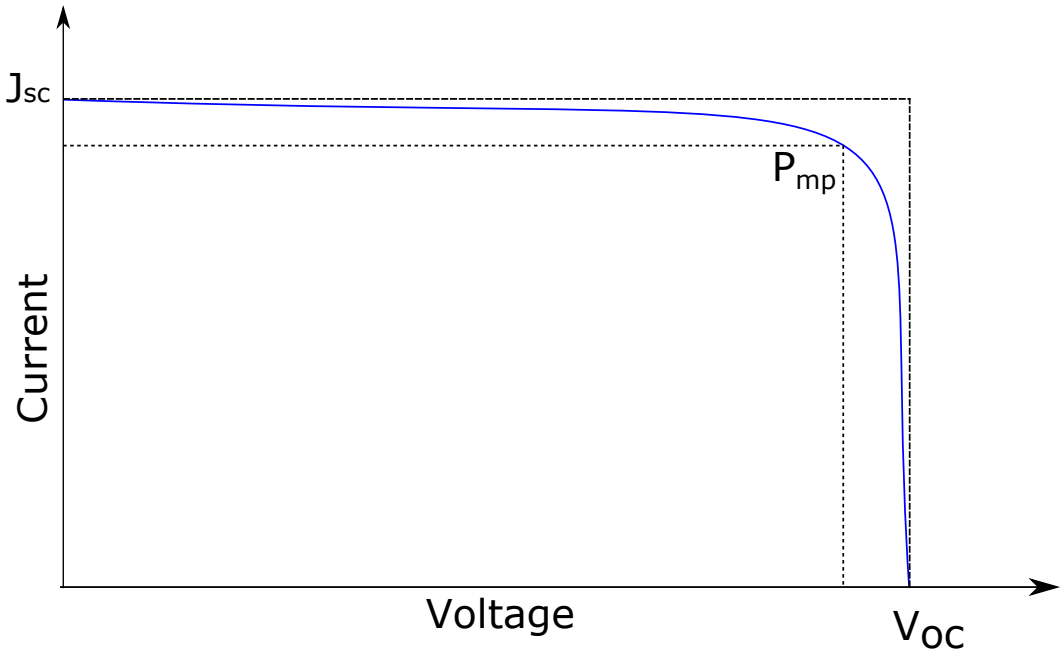

Figure 1: The current-voltage curve for a PV solar cell, indicating the open-voltage (V_{OC}), closed circuit current (I_{SC}) and maximum power point (P_{MP}).

Photovoltaic devices convert photons to electron-hole pairs, separate the charges at different leads, which generate a voltage. Excitation of the electron-hole pairs is subject to energy and momentum conservation [1]. The reverse of this process is known as radiative carrier recombi-

[1]The total energy and momentum of the valence electron, nuclei and photon are equal to that of the excited electron and nuclei after excitation

nation and occurs when an electron in the conduction band and a hole from the valence band combine and emit a photon. The energy of the emitted photon is equal to the energy difference of the electron-hole pair.

The product of the voltage and current produced from photovoltaic devices due to the excitation and collection of electron-hole pairs is the power produced by the device. The current-voltage measurement graph of a solar cells are similar to that of figure 1.

Solar Cell Efficiency

The total power conversion efficiency of photovoltaic solar cells (η) is given by

$$\eta = \frac{V_{OC} J_{SC} FF}{P_{in}} \tag{1}$$

where P_{in} is the total incident light power, V_{OC} is the open-circuit voltage, J_{SC} is the short-circuit current density and FF is the fill-factor. Some of the parameters of equation 1 are shown in figure 1. V_{OC} is the voltage measured across a cell when the terminals are not connected i.e. the circuit is open. This is the maximum voltage the device can produce and in a single junction solar cell is limited by the band gap of the absorber layer and excited carriers recombination. The reason behind this limitation is the thermalisation of excited carriers. A carrier excited by absorbing a photon with higher energy than the band gap quickly thermalises to the band edge releasing excess energy to the phonon population. J_{SC} is the photon-current density extracted from the system while the voltage across the cell is zero i.e. the circuit is closed. The photo-current density (or the short-circuit current density) is related to the absorption strength of the semiconductor layer [13].

An ideal solar cell would generate power equal to $J_{SC} \times V_{OC}$, however there is no power outputted at J_{SC} or V_{OC}. So the ratio between the maximum power generated and $J_{SC} \times V_{OC}$ is FF.

Important sources of efficiency loss in photovoltaic solar cells are the degradation of absorber material which reduces absorption and induces defects, the latter can increase the rate of carrier recombination which is often enhanced by defects. There are a number of channels which excited carriers can recombine through, these channels are often due to impurities or radiative recombination discussed previously.

Maximum Theoretical Efficiency

The maximum possible efficiency achievable by a single junction solar cell is determined by the bang gap of the absorbing layer. This theoretical upper bound know as the Shockley-Queisser limit was proposed by William Shockley and Hans-Joachim Queisser in 1961 [14]. In their seminal work a number of approximations (such as instantaneous carrier relaxation, infinite carrier mobility and zero non-radiative recombination) were utilised to relate thermodynamic principles with quantum mechanic to approximate the maximum efficiency of an ideal device. It is demonstrated that a device with a large band gap produces large voltage while the current is small, the reverse of this is true for small band gaps. As such the identification of the ideal band gap size involves the consideration of this trade off. The maximum efficiency achievable by a device was derived to be $\sim 30\%$ with a band gap of 1.34eV [14].

The Shockley-Queisser limit only applies to single junction cell and can be overcome by a number of device architectures including hot carrier, intermediate band and multi-junction solar cells. The latter of which have reached efficiencies of over 40% and have a much higher limit of 86% [7, 15–18]. However complex architectures such as these remain expensive and challenging to produce at large scales.

Improving Power Conversion Efficiency

Producing energy through solar cells at a competitive level with other sources of energy production requires the design and production of efficient, durable and cheap photovoltaic devices. These three criteria encompass the vast majority of research areas within the solar cell research community.

The research for low cost devices is driven by the synthesis and discovery of compounds with abundant constituents which are readily available while having low processing costs. Solar cell devices based on materials such as GaAs and Si are relatively efficient, however such devices can be undesirable due to the scarcity of the constituents elements (in the case of GaAs) or the high cost of refining and production (such as the case of Si). The durability of solar cell devices is immensely important and is achieved through passivisation, containment or optimisation of synthesis procedure [19, 20]. These improvements increase the overall functional lifetime, minimise the reduction in PCE over time and can lead to higher overall efficiency. This results

in lower production energy costs and shorter energy payback time which is approximately 2.5-7 years depending on photovoltaic technology and location [21].

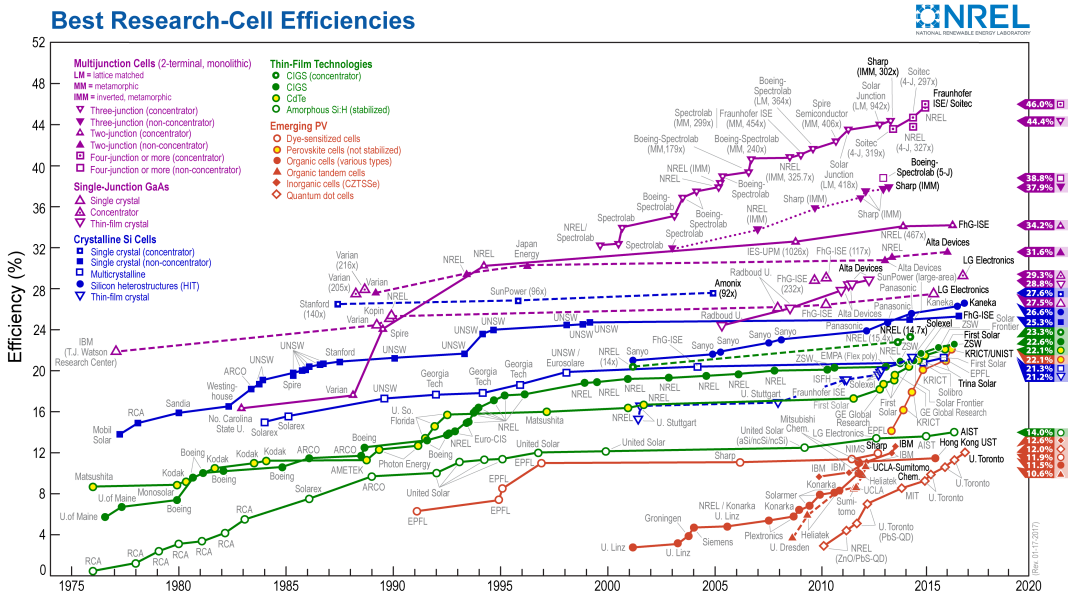

Figure 2: National Renewable Energy Laboratory (NREL) efficiency chart for various photovoltaic technologies [7].

The highest efficiency solar cells currently are multi-junction devices operating under concentrates. Such solar cells have reached efficiencies as high as 45%, however due to the higher cost, difficulty to scale up and increased complexity in implementation such devices are used in specialised roles, for example aerospace applications [7].

Over the past 45 years many new materials have been discovered and tested for photovoltaic applications. Figure 2 shows the efficiency progress of the most significant solar cell materials and architectures. Single junction silicon devices have had very little improvement over the past 20 years, however more than 90% of all solar cell devices produced are silicon based. Although GaAs devices have higher efficiencies than Si devices due to their direct band gaps (discussed in chapter 3); however their higher cost has hindered their domination of the PV market.

Chapter 1

Overview

The primary focus of this dissertation is the study of organic-inorganic hybrid Perovskites to gain an understanding of the fundamental properties of this family of materials related to photovoltaic applications.

Characteristics of interest in this works are the ones which are directly linked to the electronic properties for this family of compounds. In the next chapter inorganic, hybrid and other variants of Perovskites are introduced with attention paid to their relevance for photovoltaics. The theoretical background of the methodologies used and applied to some of the observed phenomena is presented in chapter 3; although rigorous derivations and full descriptions of these methods are beyond the scope of this work, sufficient information is provided to aid discussions in later chapters. The electronic and optical properties of a number of Perovskites form part of the findings of this work and are presented in chapter 4. The findings of this chapter related to the photovoltaic applications are discussed and a number of trends among this family of materials are identified.

In the second part, results in this work relating to the radiative recombination rate of charge carriers within hybrid Perovskites are presented. The theory, literature and the findings are discussed in chapter 5. Finally the conclusions drawn from this work along with current research in progress and future directions of this research are provided in chapter 6.

Chapter 2

Perovskites

2.1 Overview

This chapter of the thesis will introduce the Perovskites crystal structure with a focus on the organic-inorganic hybrid form. An overview of Perovskites within the field of photovoltaics, from their introduction to the current efficiency records is provided. Finally a number of observation from experimental findings related to these materials and their application in PV cells are discussed.

2.2 Introduction

In 2009 Kojima *et al.* applied $[NH_3CH_3]PbI_3$ and $[NH_3CH_3]PbBr_3$ as organic-inorganic visible-light sensitisers on TiO_2 in a dye-sensitised solar cell and achieved power conversion efficiencies of 3.8% and 3.1% respectively [8]. These semiconductors belong to a group of materials known as organic-inorganic hybrid Perovskites (OIHP). This unconventional family of materials includes an organic molecule within a Perovskites structure. This application of $[NH_3CH_3]PbI_3$ and $[NH_3CH_3]PbBr_3$ by Kojima *et al.* was the first time organic-inorganic hybrid Perovskites were utilised within the context of photovoltaic solar cells. Shortly after, a variety of approaches to include these materials in solar cells were taken [22–24]. Just 3 years after the pioneering work of Kojima *et al.*, 10.9% PCE was achieved using mixed halide Perovskites $[NH_3CH_3]PbI_{3-x}Cl_x$ coated Al_2O_3 in a non-sensitised cell architecture by Snaith *et al.* [25]. By 2013 PCE as high

as 12% were obtained using a pillared architecture, where the pores in the mesoporous TiO_2 are filled with the hybrid Perovskites instead of the coating method [26]. It has also been demonstrated that a *p-i-n* junction architecture can perform just as well as or better than previous cell architectures [27]. The unprecedented increase in PCE gathered much attention among the photovoltaic community, currently hybrid Perovskites are one of the most researched topics within this field. Eight years on since the first PV solar cell application of $[NH_3CH_3]PbBr_3$ and $[NH_3CH_3]PbI_3$, PCE exceeding 22% have been demonstrated using hybrid Perovskite solar cells [7, 11]. This rapid rate of increase in the PCE of hybrid Perovskite solar cell represents the fastest gain of all PV technologies [7].

2.3 Perovskites

The name Perovskite refers to a family of materials with chemical composition A_nBX_{2+n} in their 3D phase[1]. Perovskites can exist in many forms and for n≥1 it is possible to create 3-,2-,1- and even 0-dimensional Perovskite structures [28–30]. In the 3-dimensional non-layered case, Perovskites have the chemical composition ABX_3 and their crystal structure is similar to that of calcium titanate. This crystal structure and calcium titanate which is also know as Perovskite are named after the Russian mineralogist Lev Perovski who first characterised its structure.

It has been shown that higher dimensional Perovskites can posses a wide range of polymorphs such as cubic, tetragonal, orthorhombic and rhomboidal. The high symmetry cubic Perovskite phase is shown in figure 2.1.

Single Perovskite

3-dimensional single Perovskites are a subgroup within this family of materials with the chemical formula ABX_3. The A constituent is surrounded by 8 corner sharing BX_6 polyhedrons. Tilting, rotating and stretching of these polyhedrons allows for a number of additional non-cubic Perovskite phases. Transitions between these Perovskite phases have been observed through varying temperature, pressure and other external factors [31, 32].

The phase and stability of a Perovskite are strongly dependent on the relative sizes of the

[1]Layered Perovskites are characterised by a different chemical composition, namely $A_{n-1}A'_2B_nX_{3n+1}$ in the Ruddlesden-Popper phase.

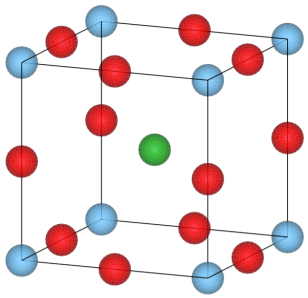

Figure 2.1: The high symmetry cubic Perovskite phase of $CaTiO_3$, where calcium, titanium and oxygen atoms are indicated by green, blue and red respectively.

constituent ions. These characteristics can be investigated through the Goldschmidt tolerance factor given by:

$$t = \frac{r_A + r_X}{\sqrt{2}(r_b + r_X)} \tag{2.1}$$

where r_A, r_B and r_X are the Shannon radii of the A, B and the X ions respectively [33,34]. At finite temperatures for values near the range of $0.8 \leq t \leq 1$ the material is likely to possess a Perovskite structure. For values of $t < 0.8$ lower symmetry Perovskite or non-Perovskite phases are obtained. Values of $t >> 1$ indicate that the A cation is too large to form a Perovskite phase, while $t \approx 1$ indicates a high symmetry Perovskite phase. Table 2.1 shows the tolerance factors for a number of known Perovskites and their observed phases.

Inorganic Perovskites	Perovskite phases	Tolerance factor
$SrTiO_3$	Tetragonal,Cubic	1.002
$BaTiO_3$	Rhombohedral, Orthorhombic, tetragonal ,cubic	1.062
$CaTiO_3$	Orthorhombic, tetragonal ,cubic	0.9666
$GdFeO_3$	Orthorhombic	0.813
$PbTiO_3$	tetragonal,Cubic	1.02

Table 2.1: The Goldschmidt factor can be used as a semi-empirical guide for the existence of Perovskite phases, for instance a tolerance factor close to 1 indicates a cubic Perovskite phase [35–37].

Equation 2.1 shows that a wide range of Perovskite compounds can and indeed have been predicted by the permutation of ions. Furthermore the flexibility in the constituents of the compound allows for a great degree of tuning for desired properties. Such level of control over the characteristics of Perovskites has resulted in a wide range of applications of these materials from water splitting, high temperature super conductivity, lasers and more recently photovoltaics [8, 38–40].

Double Perovskites

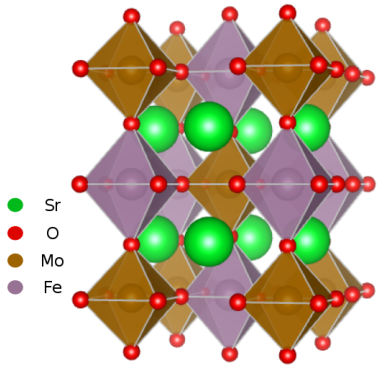

Figure 2.2: The crystal structure for the cubic double Perovskite phase of Sr_2FeMoO_6.

Double Perovskites have a similar crystal structure as that of single Perovskites, however they posses a chemical composition $A_2BB'X_6$. In these structures B and B′ form a checkered pattern alternating at the centre of the corner sharing polyhedrons. Therefore the unit cell is double that of the single Perovskite, hence the name. Figure 2.2 shows the cubic crystal structure of Sr_2FeMoO_6 a double Perovskite which has been extensively studied for spintronic applications [41].

Organic-Inorganic Hybrid Perovskites

Most Perovskites synthesised (e.g. $BiFeO_3$) or those which occur naturally (e.g. $PbTiO_3$) are oxides with chemical composition ABO_3 as shown in table 2.1. These compounds are formed by divalent A^{+2} ions, tetravalent B^{+4} metals and divalent oxygen anions. However the relatively

new group of Organic-Inorganic Hybrid Perovskites (OIHP) are not oxides, rather halide based compounds. Unlike their oxide counterparts these halide crystals are formed by monovalent A^+ organic molecules, divalent B^{+2} metals and monovalent halide anions. Other variants such as mixed cations, mixed anions or partial substitution of the halogen component by organic molecules have also been proposed and synthesised [42–44].

The first successful synthesis of a Perovskite was in 1893, while the existence of halide Perovskites in the form of $CsPbI_3$ has only been known since 1958 [45,46]. Unlike their inorganic counterparts, hybrid Perovskites have a much more recent history. Methylammonium triiodide plumbate (MAPI) which has the chemical composition $[NH_3CH_3]PbI_3$ is the first OIHP which was synthesised and reported as having a Perovskite phase in 1978 [47,48]. Through substitution of MAPI's constituent ions and often using the Goldschmidt tolerance factor as a guide, a large range of hybrid Perovskites have since been synthesised [49].

Much like inorganic Perovskites, the stability and formation of the hybrid Perovskites can also be investigated through the Goldschmidt tolerance factor. However as discussed by Travis *et al.* the application of equation 2.1 with the Shannon radii does not provide accurate predictive results for hybrid Perovskites [50]. This is due to a number of reasons: firstly the Shannon radii are calculated for the oxide and fluoride compounds only and hence are not applicable to iodine or bromine based Perovskites. Secondly an accurate description of the Shannon radii for organic molecules is non-trivial. Due to these reasons Travis *et al.* developed a method for predicting the formation of a single Perovskite structure in ABX_3 compounds where X=Cl, Br, I. This new approach which results in a higher predictive accuracy is based on equation 2.1 and a newly defined factor known as the octahedral tolerance factor given by

$$\mu = \frac{r_B}{r_X} \tag{2.2}$$

where r_B and r_X are the ionic radii of the B and X constituents. Using the hard sphere approach it can be shown that for a stable structure μ must be greater than 0.41. In this approach, the ionic radii of the organic molecules are calculated as suggested by Cheetham *et al.* given by:

$$r_A = r_{mass} + r_{ion} \tag{2.3}$$

where r_{ion} is the Shannon radii and r_{mass} the distance between the centre of mass and the furthest non-hydrogen atom [51].

With the reported success of $[NH_3CH_3]PbI_3$ and $[NH_3CH_3]PbBr_3$, the search for new hybrid Perovskites began, with the intent to produce more efficient and stable devices. It is clear from equation 2.1 that for a stable structure with $t \approx 1$, the radius of the ion at site A would need to be much larger than that at site B. Using the new predictive method it is found that for Perovskites with iodine at the X site and the smallest possible ion to satisfy $\mu > 0.41$ on site B, the site's A ionic radius for 12 coordination must be 0.9Å. The only possible non-radioactive element which can satisfy this is Cs^+ with a resulting tolerance factor of 0.91. This observation is the reason why larger organic molecules are utilised for halide Perovskites site A occupation. Using this approach and studying of known inorganic and hybrid Perovskite structures Travis *et al.* have identified a semi-empirical set of conditions for stable hybrid Perovskites. For a given structure with $\mu > 0.41$ and $t > 0.875$, the formation of a hybrid Perovskite phase is highly likely [50]. The tolerance factors of a number of known and predicted ABX_3 compounds are shown in table 2.2.

Compound	phase	tolerance factor
$[NH_3CH_3]PbCl_3$ (MAPC)	Orthorohmbic,Tetragonal,Cubic	0.985
$[NH_3CH_3]PbBr_3$ (MAPB)	Orthorohmbic,Tetragonal,Cubic	0.974
$[NH_3CH_3]PbI_3$ (MAPI)	Orthorohmbic,Tetragonal,Cubic	0.954
$[CH(NH_2)_2]PbI_3$ (FAPI)	Orthorhombic, Cubic	1.035
$[NH_4]PbI_3$ $(NH_4PI)^\dagger$	N/A	0.801
$[(CH_3C(NH_2)_2)_2]SrI_3$ $(ACSI)^*$	N/A	1.04
$[NH_3CH_3]DyI_3$ $(MADI)^*$	N/A	0.973
$[NH_3CH_3]SmI_3$ $(MASmI)^*$	N/A	0.931

Table 2.2: Synthesised ABX_3 compounds (where A is an organic molecule, B a metal and X a member of the halogen family) with their corresponding observed phases and tolerance factors. All of the compounds above have $\mu > 0.41$. The organic molecules of these compounds are shown in table 2.3.* These compounds have not yet been synthesised and hence information regarding their phases is not available† $[NH_4]PbI_3$ does not form a Perovskite phase and this is correctly predicted as $t = 0.81 < 0.875$ [50].

It should be noted that stable Perovskite phases for $MAGeI_3$, $FaGeI_3$ and $ACGeI_3$ have been reported where $\mu \approx 0.35$. These compounds fall outside the boundary conditions set by Travis *et al.*. This deviation is attributed to the presence of stereo-active lone-pairs on the Ge sites which in this case relaxes the octerhedon tolerance factor requirement [52].

Compound	Abbreviation	Ionic radii Å	Dipole Moment
NH_3CH_3	MA	2.16	2.29
$[CH(NH_2)_2]$	FA	2.53	0.21
NH_4	NH_4	1.46	0.0
$(CH_3C(NH_2)_2)$	AC	2.77	1.2

Table 2.3: Organic molecules for hybrid Perovskites [50, 53, 54].

The upper bound for the tolerance factor using the hybrid Perovskite approach is not clearly defined. To establish an upper limit for t, access to a larger number of hybrid compounds with structure ABX_3 is needed.

2.4 Application of Perovskites for Photovoltaic Solar Cells

Within the OIHP family $[NH_3CH_3]PbI_3$ and $[CH(NH_2)_2]PbI_3$ (henceforth refereed to as MAPI and FAPI respectively) are considered to be two of the most promising variants for photovoltaic applications. These materials have shown remarkable properties for PV solar cell applications while having relatively simple and cheap production procedures compared to more established photovoltaic materials such as silicon. Some of the characteristics of these materials which have drawn considerable attention include long carrier lifetimes, strong light absorption and low density of mid band gap defects; the combination of such features leads to high PCE [55–57]. As a consequence of long minority lifetimes and strong absorption of visible light observed in a number of lead based hybrid Perovskites, thin absorber layers with high quantum efficiencies have been fabricated [58–60]. Additionally the low density of mid band gap defect reduces the non-radiative recombination which can be detrimental to PV materials. Due to these factors hybrid Perovskite based solar cells have been hailed as potential materials for first large scale commercial realisation of a "3^{rd} generation" solar cells [16]. The combination of low production

cost, abundant constituent elements and high power conversion efficiencies are some of the extraordinary properties that Perovskite solar cells posses [22].

An overview of Perovskites (hybrid and inorganic) relevant to this work is provided below. Although not all of the materials in the following sections are explicitly studied within this thesis, a general review of the applications and properties of these Perovskites is essential for discussions in later chapters.

$\mathbf{NH_3CH_3PbX_3(X=Cl,Br,I)}$

As mentioned previously MAPI and MAPB are the first hybrid Perovskites which were utilised for photovoltaic applications [8]. However MAPI, MAPB and $[NH_3CH_3]PbCl_3$ (referred to as MAPC) were first synthesised much earlier [47, 48].

This group of OIHP possess three Perovskite phases, ranging from low temperature orthorhombic to high temperature pseudo-cubic as shown in table 2.2; The structures here are referred to as pseudo-cubic, this is due to the fact that the inorganic part of the lattice can be fairly well approximated as cubic structures, however due to the non-spherical nature of the organic constituents the cubic symmetry of the overall lattice is lost. In the case of MAPI the transition from the orthorhombic to tetragonal is a first order transition at $\approx$ 165K. While the transition from tetragonal to the pseudo-cubic phase is a gradual second order transition, with a complete pseudo-cubic phase at $\approx$ 337K [61]. In agreement with Goldschmidt tolerance factors, experimental findings show that MAPC is the most stable while MAPI is the least stable of the three [49].

These hybrid Perovskites form relatively open structures; the metal-halide bond length decreases with lighter halides. At room temperature MAPI has a pseudo-cubic structure with an experimental lattice constant $a = 6.26$Å, while MAPB and MAPC have smaller lattice constants of 5.9Å and 5.6Å respectively [62–64]. The open structure in MAPI allows for the rotation of $NH_3CH_3^+$ molecule. This has been observed both experimentally and through molecular dynamics simulations [65,66]. Figure 2.3 shows three orientations of $NH_3CH_3^+$ in the pseudo-cubic phase which are accessible at room temperature.

The experimental room temperature optical band gap for MAPI is $\approx$1.55eV, small variations due to synthesis method have been observed [1]. This energy gap is close to the optimal value for solar cells and has a Shockley-Queisser efficiency limit close to 30% [1,14]. With the substitution

of lighter halides in place of iodine which reduces the size of the unit cell, the band gap increases to ≈ 2.24eV for MAPB and ≈ 2.97eV for MAPC [1]. While the band gap energies of MAPB and MAPC are too high for single junction solar cells, multi-junction solar cell applications are feasible with such band gaps.

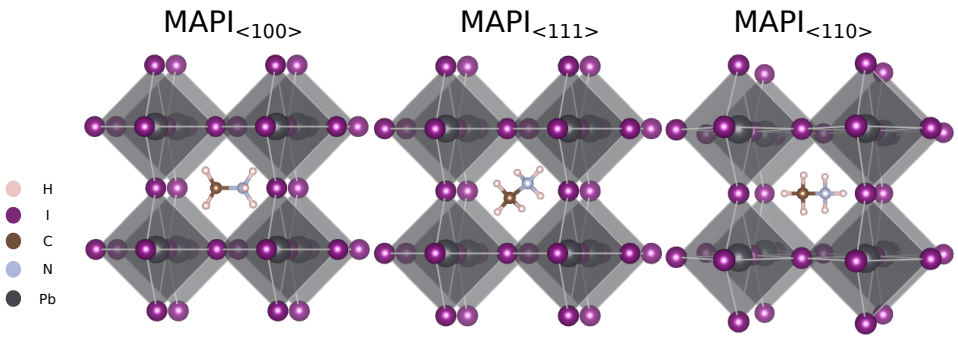

Figure 2.3: The room temperature pseudo-cubic structure of MAPI with 3 orientations of the organic moiety.

So far from these three hybrid Perovskites the highest PCE devices are based on MAPI and have reached 19% [67]. This is due to the more optimum band gap size compared to the other two Perovskites.

The high PCE achieved by these devices is surprising as the materials are produced through low temperature processing. Such methods often yield samples with impurities and small grain boundaries which reduce the overall device efficiency. However it has been observed that samples produced through relatively simple bench-top methods of synthesis, have sufficiently low density of mid gap defects. Furthermore the lead based hybrid Perovskites have demonstrated extremely long carrier lifetimes which for materials with relatively low carrier mobilities increase diffusion length and the overall PCE [68–70]. The long carrier lifetimes in these materials is discussed in detail in chapter 5.

Tin based hybrid Perovskites with chemical compositions $[NH_3CH_3]SnX_3$(X=I,Br,Cl) have also been investigated for photovoltaic applications. Although the band gap size is more ideal, these materials have not achieved the same success or attention as the lead based counterparts. The lower PCE is partially attributed to the significantly lower carrier lifetimes and stability

of tin based hybrid Perovskite devices. Tin based hybrid Perovskites are less stable in ambient atmosphere compared to MAPI, this is due to the instability of Sn^{2+} in its oxidation state [71,72].

$[CH(NH_2)_2]PbI_3$ (FAPI)

The substitution of methylammonium in MAPI by formamidinium (FA) increases the cell size and reduces the experimental optical band gap from $\approx$ 1.55eV to $\approx$ 1.48eV [73, 74]. This is due to the bigger size of formamidinium compared to methylammonium, as shown in table 2.3. The lower band gap of FAPI increases the maximum achievable theoretical efficiency [14]. In fact FAPI based Perovskite solar cells have recently achieved power conversion efficiencies of 20.1% [11]. Experimental findings show that at room temperature FAPI, much like MAPI, forms a pseudo-cubic structure with a larger lattice constant of a=6.362Å [66]; however FAPI is even less stable that MAPI, and has been reported to form a competing yellow hexagonal non-Perovskite phase [66, 75, 76]. The room temperature pseudo-cubic Perovskite structure for FAPI is shown in figure 2.4.

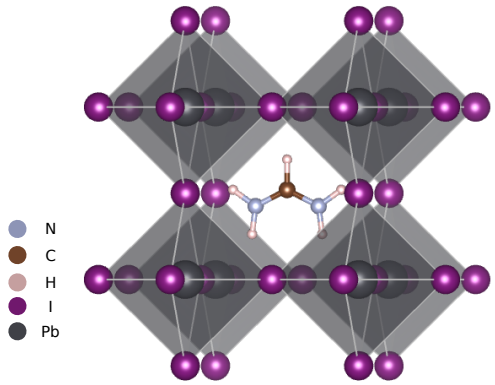

Figure 2.4: Pseudo-cubic room temperature structure of $[CH(NH_2)_2]PbI_3$ (FAPI).

Simulations of FAPI have shown that the organic molecule rotates at room temperature, similar to that found in MAPI, however on a slightly faster timescale [66]. The dipole moment of FA^+ is approximately 11 times smaller than that of MA^+, however the level of interaction between the two molecules and the inorganic cages are comparable. This is due to the larger size of $CH(NH_2)_2^+$ and the steric effect which compensates for the lower dipole moment.

Mixed Perovskites

Although pure MAPI and FAPI have shown a significant increase in power conversion efficiencies, the success of mixed Perovskites has been just as or even more impressive and important. This approach allows for overcoming many of the disadvantages associated with hybrid Perovskites such as band gap size and stability. Mixing of Perovskites comes in a variety of forms such as mixed halides, organic molecules and metals. These groups of novel materials are discussed n the following sections.

Mixed Halide

The first attempt at mixing hybrid Perovskites came in the form of mixed halides [25]. Structures with chemical compositions $MAPbI_{3-x}Cl_x$, $MAPbI_{3-x}Br_x$ and $MAPbBr_{3-x}Cl_x$ were synthesised and implemented in cells [77–80]. The aim of this approach is to combine the low band gap of MAPI, which is close to ideal, with the high stability of MAPC. Solar cells based on these mixed Perovskites displayed an increase in mobility, crystallinity and overall PCE compared to pure phase MAPI. However later studies found that the added Cl only enhanced the synthesis process and was only minimally present in samples [77].

Mixed Site A Cation

Mixing of the organic cations in hybrid Perovskites led to power conversion efficiencies as high as 14.52% in the form of $FA_{0.4}MA_{0.6}PbI_3$ [44]. More recent studies of mixed cations, where there is partial substitution of MA by FA and Cs leading to a triple cation Perovskite have shown remarkable stability, losing negligible PCE over 250 hours at room temperature, significantly out performing pure phase devices. In addition, power conversion efficiencies achieved by these materials are close to 21.1% [81]. Organic molecules mixing, along with halide mixing in the form of MA/FA and I/Br have have produced cells with PCE as high as 17.3% leading to yet another approach to creating stable and high efficiency PSCs [82]. Unlike in the case of mixed halide, experimental findings show that the FA and MA are present in the final sample and their roles are not limited to the synthesis enhancement.

Mixed Metals

Mix-metal hybrid Perovskites have been utilised in an attempt to overcome the barriers met by pure phase hybrid Perovskites, additionally these Perovskites have demonstrated promising properties. Much like mixed halide Perovskites, this group of hybrid Perovskites are formed by the partial substitution of the site B metal cation by another metal. $[NH_3CH_3Sn_x]Pb_{1-x}I_3$ is perhaps the most documented of this category. An interesting and significant characteristic of this solid solution was the violation of Vegard's law, which results in tuning the ratio of lead and tin to obtain band gaps below that of both the pure Sn and Pb phases [83, 84]. It is shown that for $x = 0.5$ optical band gaps as low as 1.17eV can be achieved. Such tunability of the band gap is ideal for tandem solar cells. Furthermore energy-dispersive x-ray spectroscopy has shown that both Sn and Pb are homogeneously present across the sample without any observed phase separation [83, 84].

Downfalls of Hybrid Perovskite Solar Cells

Although hybrid Perovskites may seem promising as a potential light harvesting material for commercial solar cells, a number of obstacles hinder this progress. The ionic crystal structure of organic-inorganic hybrid Perovskites can be dissolve in polar solvents such as water [54, 85, 86]. This instability is apparent at high relative humidity and causes significant degradation and reduction in PCE. Furthermore, the general stability of hybrid Perovskite is significantly lower than those of commercial devices and inorganic absorber layers. The rapid degradation of Perovskite solar cell under ambient environment and working conditions leads to a significant lose of PCE over relatively short period [87].

The best performing Perovskite solar cells (PSC) have thus far been lead based. Although the use of lead in PV solar cells is not expensive, as it is a heavy element it is highly toxic. This fact combined with low stability of hybrid Perovskites reduces the possibility of residential applications of PSC. Hence a substitute for lead which can perform just as well is highly desirable. These are some of the main challenges faced by the researchers working in the field of hybrid Perovskite solar cells.

Chapter 3

Theoretical Background

3.1 Overview

Electronic and optical properties are among the most important material characteristics for photovoltaic applications. Absorption coefficient, carrier mobility and band gap are a few of such parameters which among others determine the viability of a photovoltaic material. An accurate description of such parameters and mechanisms at work are hence crucial for solar cell device engineering. In this section the framework and methodologies used to obtain the electronic and optical parameters are described. The applicability, limitations and the advantages of each method are briefly discussed.

3.2 Introduction

The electronic and optical properties of periodic systems are related to the electronic states described through the system's electronic band structure. In isolated systems such as a molecule or an atom in vacuum, the electronic energy levels are quantised by orbitals, in these systems the discrete electronic energy states are uniquely identified by four quantum numbers (the principal quantum number n, orbital angular momentum quantum number l, magnetic quantum number m and spin s). This discrete quantization of energy states of an atom is shown in the left panel of figure 3.1. In crystalline material with infinite periodicity n, l and m cease to be quantum numbers which uniquely describe an electronic state; however they retain an

approximate meaning since eigenstates can be fairly well represented by a linear combination of atomic orbitals. According to Bloch's theorem, the wave-function of an electron in a periodic system has a basis of Bloch wave eigenstates [88]. A Bloch wave is written as:

$$\psi(\vec{r}) = e^{i\vec{k}\cdot\vec{r}}U(\vec{r}) \tag{3.1}$$

where $\vec{r}$ is position, $U(\vec{r})$ is a periodic potential with same periodicity as the crystal structure and $\vec{k}$ is the crystal momentum. Here $\vec{k}$ is a new quantum number necessary for uniquely describing electronic states within periodic potentials. For a given system there can be many Bloch wave eigenstates, these are known as bands. The electronic eigenstates in periodic systems form contentious energy states, this is contrary to the isolated atom case discussed. The band structure of a semiconductor is shown in the right panel of figure 3.1.

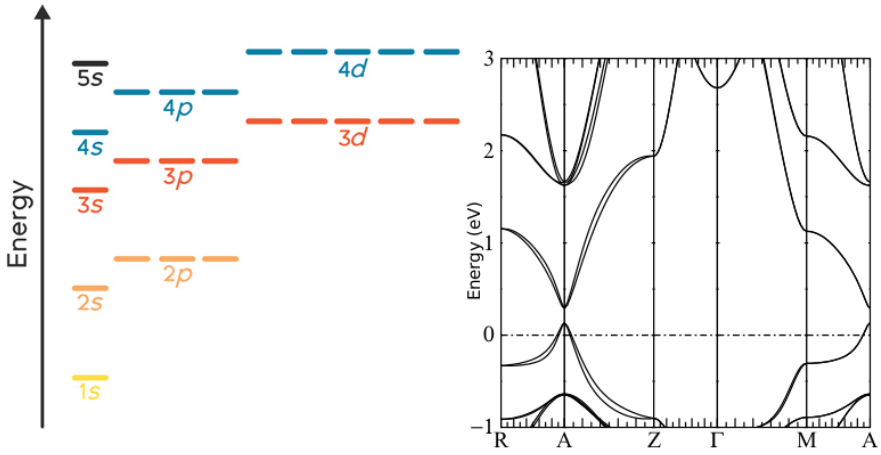

Figure 3.1: The electronic energy levels of an arbitrary atom (left panel) and a crystalline system, $CsPbI_3$ in the example above (right panel).

The following sections provide brief overviews of Density Functional Theory (DFT), GW and quasi-particle self-consistent GW (QSGW), which are some of the methods used to calculated such electronic band structures. A full derivation and comparison of such methods is beyond the scope of this thesis, however differences between the capabilities of these methods and their limitations which are important to the calculations in this work are discussed.

3.3 Electronic Properties

Density Functional Theory

In quantum mechanics all the information that can possibly be known about a system is contained within the corresponding wave function. As such when studying a quantum system often the aim is to obtain the wave function, to do this, it is necessary to solve the Schrödinger equation related to that system. The time-independent form of the Schrödinger equation is given by:

$$\hat{H}\Psi_i(\mathbf{x}_1, \mathbf{x}_2, \cdots, \mathbf{x}_n, \mathbf{r}_1, \mathbf{r}_2, \cdots, \mathbf{r}_N) = E_i\Psi_i(\mathbf{x}_1, \mathbf{x}_2, \cdots, \mathbf{x}_n, \mathbf{r}_1, \mathbf{r}_2, \cdots, \mathbf{r}_N) \tag{3.2}$$

where $\mathbf{x_i}$ is the position of the i^{th} electron and $\mathbf{r_i}$ is the position of the i^{th} nucleon. Equation 3.2 relates the system's Hamiltonian $\hat{H}$ with the i^{th} eigenstates $\Psi_i(\mathbf{x}_1, \mathbf{x}_2, \cdots, \mathbf{x}_n, \mathbf{r}_1, \mathbf{r}_2, \cdots, \mathbf{r}_N)$ and the corresponding eigenvalues for a system with n electrons and N nuclei.

The Hamiltonian for the total energy of an atomic system with electrons is

$$\hat{H}_{tot} = -\sum_I \frac{1}{2M_I}\nabla_I^2 - \frac{1}{2}\sum_i \nabla_i^2 + \frac{1}{2}\sum_{i\neq j}\frac{1}{|\mathbf{x}_i - \mathbf{x}_j|} + \frac{1}{2}\sum_{I\neq J}\frac{Z_I Z_J}{|\mathbf{r}_I - \mathbf{r}_J|} - \sum_{i,I}\frac{Z_I}{|\mathbf{x}_i - \mathbf{r}_I|} \tag{3.3}$$

$$= -\hat{T}_N - \hat{T}_e + \hat{V}_{ee} + \hat{V}_{NN} - \hat{V}_{eN} \tag{3.4}$$

where M_I, $\mathbf{r}_I$ and Z_I are the mass, position and the charge of the I^{th} nuclei respectively, while $\mathbf{x}_i$ is the position of the i^{th} electron (all equations are presented in atomic units unless stated otherwise) [89, 90][1]. The upper-case subscripts span over all nuclei while lower-case subscripts cover all electrons within the system. Each term within this equation accounts for contributions from a particular interaction. The first two terms in equation 3.3 are the electronic and the nuclei kinetic terms respectively, these terms account for the energy from the motion of the particles in the system. The last three terms are the electron-electron, electron-nucleon and nucleon-nucleon interactions, these terms arise from the charged nature of protons and electrons.

Nuclei are significantly heavier than electrons and as a result are considerably slower. As such in atomic systems nuclei are often assumed to be stationary, that is the electrons move through a field with static nuclei. This assumption is known as the Born-Oppenheimer approximation (BOA), within this approach the first term in equation 3.3 can be neglected and the nucleon-nucleon interaction can be added as a constant to the total energy [89, 91, 92]. With the BOA

[1] For the sake of brevity relativistic effects and spins are excluded

the Hamiltonian simplifies to that of electrons moving in an external field

$$\hat{H}_e = -\frac{1}{2}\sum_i \nabla_i^2 + \frac{1}{2}\sum_{i\neq j}\frac{1}{|\mathbf{x}_i - \mathbf{x}_j|} - \sum_{i,I}\frac{Z_I}{|\mathbf{x}_i \mathbf{r}_I|} \tag{3.5}$$

$$= -\hat{T}_e + \hat{V}_{ee} - \hat{V}_{eN} \tag{3.6}$$

where $i \neq j$ in the second summation ensures that self interaction is neglected. Hence the electronic Schrödinger equation

$$\hat{H}_e \Psi_i^e(\mathbf{x}_1, \mathbf{x}_2, \cdots, \mathbf{x}_n) = E_i^n \Psi_i^e(\mathbf{x}_1, \mathbf{x}_2, \cdots, \mathbf{x}_n) \tag{3.7}$$

where $\Psi_i^e(\mathbf{x}_1, \mathbf{x}_2, \cdots, \mathbf{x}_n)$ and E_i^n are the eigenfunction and eigenvalue of the i$^{\text{th}}$ electronic state [93]. The total energy of the system can be obtained by adding the nucleon-nucleon interaction. As the nucleons are assumed to be static the information regarding their position is contained within the Hamiltonian rather than the wave function.

Even with the simplifications of the BOA, solving the Schrödinger equation for a many-body system with such Hamiltonian is practically an impossible task. The difficulty arises from the electron-electron interaction and the correlation in the motion of the electrons caused by it. Hence a system with n electrons requires a $3n$-dimensional wave function[2]. For even relatively small systems with a handful of electrons computing equation 3.5 numerically is not feasible. The solution to equation 3.5 is the focus of band structure calculations

Hohenberg-Kohn Formalism

In their 1964 seminal paper Hohenberg and Kohn proposed a new approach to computing the electronic Hamiltonian. They established that for a system of electrons moving under the influence of an external potential V_{ext} and electron-electron interaction V_{ee}, the ground state total energy is a functional of the corresponding electron density $\rho(\mathbf{x})$ [94]. To demonstrate this, the energy functional is written as

$$E_e[\rho(\mathbf{x})] = \int \rho(\mathbf{x}) V_{ext}(\mathbf{x}) d\mathbf{x} + F[\rho(\mathbf{x})] \tag{3.8}$$

$$= \langle \Psi^e | \left(V_{ext} + F\right) | \Psi^e \rangle = \langle \Psi^e | \hat{H}_e | \Psi^e \rangle \tag{3.9}$$

where $\hat{F}[\rho(\vec{\mathbf{x}})]$ is a universal functional of electronic density and accounts for the kinetic energy and electron-electron interactions [89, 94]. Honhenberg and Kohn also demonstrated that the

[2]The factors of 3 accounts for three degrees of spatial freedom for each particle. As mentioned previously spin indices are omitted for sake of simplicity.

external potential uniquely defines the ground state density of the system to within an additive constant. To derive this lets assume there exist two external potentials $V_{ext}^{(1)}$ and $V_{ext}^{(2)}$ which produce the same ground state electronic density $\rho_0(\mathbf{x})$, there must also exist two set of Hamiltonians $H_e^{(1)}$ and $H_e^{(2)}$ with their corresponding wave functions $\Psi_{(1)}^e$ and $\Psi_{(2)}^e$ which both yield $\rho_0(\mathbf{x})$. In such case using the variational principle, it is clear that the ground state energy $E_g^{(1)}$ of $H_e^{(1)}$ is only given by $\Psi_e^{(1)}$, hence using any $\Psi_e^{(2)}$ as a guessed wave-function for $H_e^{(1)}$ will lead to an energy higher than that of the ground state,[3]. That is

$$E_g^{(1)} < \langle \Psi_e^{(2)} | H_e^{(1)} | \Psi_e^{(2)} \rangle \tag{3.10}$$

$$E_g^{(1)} < \langle \Psi_e^{(2)} | H_e^{(2)} | \Psi_e^{(2)} \rangle + \langle \Psi_e^{(2)} | H_e^{(1)} - H_e^{(2)} | \Psi_e^{(2)} \rangle \tag{3.11}$$

$$E_g^{(1)} < E_g^{(2)} + \int d\mathbf{x} [V_{ext}^{(1)} - V_{ext}^{(2)}] \rho_0(\mathbf{x}) \tag{3.12}$$

by interchanging the subscripts in expression above it is possible to obtain the counter part for $E_g^{(2)}$:

$$E_g^{(2)} < E_g^{(1)} + \int d\mathbf{x} [V_{ext}^{(2)} - V_{ext}^{(1)}] \rho_0(\mathbf{x}) \tag{3.13}$$

adding the last two expressions leads to the contradictory inequality

$$E_g^{(2)} + E_g^{(1)} < E_g^{(1)} + E_g^{(2)} \tag{3.14}$$

this contradiction demonstrates that there can not be two different external potentials which differs by more than an additive constant and lead to the same non-degenerate ground state charge density. Hence the total ground state energy of an electronic system is a functional of the ground state density.

The significance of this formalism is in the fact that the calculation of the ground state energy of an n-electron system is no longer a function of a $3n$-dimensional wave function but rather the 3-dimensional electronic density.

Kohn-Sham approach

Although the Hohenberg-Kohn (HK) provides a great simplification to solving the electronic Hamiltonian, there remain a number of barriers which render this approach inapplicable. The first issue with the HK formulation is that the universal functional $\hat{F}[\rho(\vec{\mathbf{x}})]$ (which maps the

[3] assuming non-degenerate ground states

electronic density to the kinetic and internal interaction energy contributions) is unknown and has to be replaced by an approximate form, this reduces the HK theorem from an exact method to an approximation. However the greatest simplification to the HK approach came from a 1965 paper by Kohn and Sham (KS). In their approach the $3n$-dimensional wave-function of the n interacting electrons system was replaced by n 3-dimensional non-interacting single particle wave-functions [95]. By choosing to use non-interacting auxiliary single particle wave functions a number of simplifications are automatically incurred. One such simplification is that the kinetic term can be rewritten in the single particle form and not as a functional of the electronic density. By rewriting the kinetic contribution the single particle Hamiltonian is given by

$$\hat{H}_{KS} = \frac{1}{2}\nabla^2 + \hat{V}_{KS}(\vec{r}) \tag{3.15}$$

where $\hat{V}_{KS}(\vec{r})$ is the KS potential which accounts for all electronic interactions as shown in the expression below

$$\hat{V}_{KS}(\vec{r}) = \hat{V}_{ext}(\vec{r}) + \hat{V}_H(\vec{r}) + \hat{V}_{XC}(\vec{r}) \tag{3.16}$$

where the terms on the right hand side are the external potential, the Hartree term and the exchange-correlation potential respectively [89, 90]. In this approach the external potential will include the contribution from electron-nucleon interaction and other external potentials. The Hartree potential accounts for the Coulomb interaction which the electrons experience.

The exchange-correlation potential is a universal function which arises due to the electron-electron interactions and Pauli's exclusion principle, similar to the universal functional $\hat{F}[\rho(\vec{\mathbf{x}})]$ the exact form of the exchange-correlation potential

$$\hat{V}_{XC}(\vec{r}) = \frac{\delta E_{XC}}{\delta n(\vec{r})} \tag{3.17}$$

is unknown. This term contains all the many-body interactions which have to be added due to using the single particle approximation which intrinsically neglects all such effects. As the true form of this potential is unknown and is likely to be highly complex and potentially non-analytical, approximate potentials have to be used for this method to be applicable [96]. Since the 1965 seminal paper many *ab initio* and empirical potentials have been developed for this task.

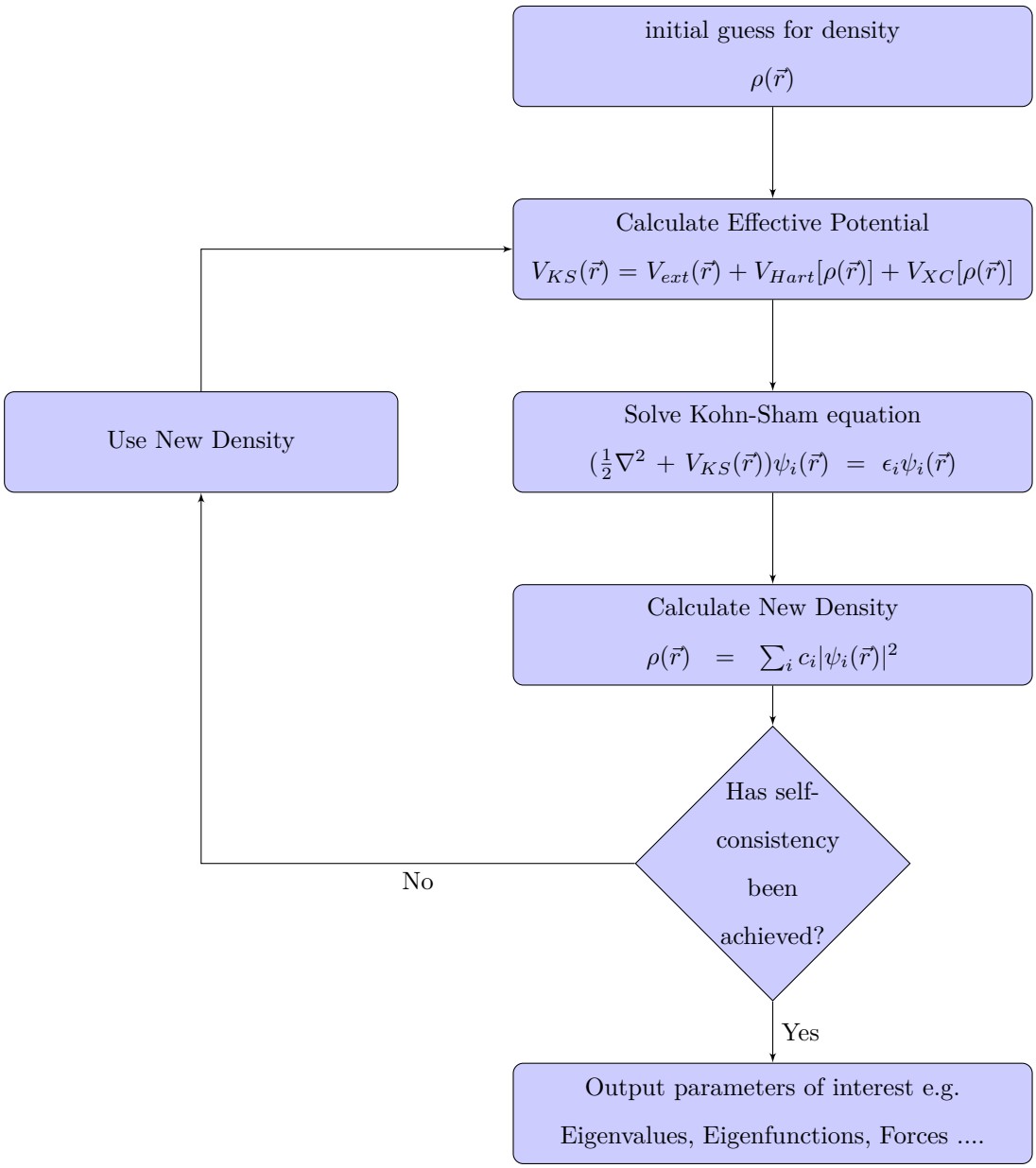

Figure 3.2: Schematic diagram showing the iterative process of solving the Kohn-Sham equation to obtain self-consistent electronic density.

Using the Kohn-Sham approach the eigenvalues of non-interacting wave functions can be

calculated through a Schrödinger-like equation known as the Kohn-Sham equation given by

$$(\frac{1}{2}\nabla^2 + \hat{V}_{KS}(\vec{r}))\,|\phi_n\rangle = \epsilon_n\,|\phi_n\rangle \tag{3.18}$$

where ϕ_n and ϵ_n are the eigenfunctions and eigenvalues of the n^{th} single particle wave function.

Due to the non-linear nature of equation (3.18) an iterative method is used to solve for the ground state wave functions $\{\psi_n\}$ and hence the electronic contribution to the total ground state energy. This iterative process starts by choosing a starting guessed electronic density which is used to calculate the effective KS potential. This potential is used within equation 3.18 to obtain new set of wave functions which are used to obtain a new electronic density. The newly obtained and the starting densities are compared, if their difference is within the set convergence limit the process is stopped. However if the changes are too large the process is repeated with the new density used as the starting point. This iterative process is shown in diagram 3.2.

As the eigenfunctions of the KS equation are that of fictitious non-interacting particles, their individual eigenvalues ϵ_n do not correspond to electronic energies of the real system, however the highest eigenvalue is minus the ionisation energy [89,97]. The KS eigenvalues and eigenfunctions shown in equation 3.18 are often used as the real system's counterparts without a rigorous justification. This leads to significant under estimation of band gaps in semiconductors as discussed in the following sections. The approximations for the exchange-correlation functional often aim to reduce induced errors due to the use of non-physical eigenfunctions and eigenvalues.

Local Density Approximations

One possible approximation for the exchange-correlation functional is to model the electron-electron interactions in the system of interest as that of a homogeneous electron gas (i.e. Jellium) [89, 95]. In this form the exchange-correlation energy functional simply is given by

$$E_{xc}[\rho(\mathbf{r})] = \int d^3r\rho(\mathbf{r})\epsilon_{xc}^{hom}(\rho(\mathbf{r})) \tag{3.19}$$

where $\epsilon_{xc}^{hom}(\rho(\vec{r}))$ is exchange-correlation energy per unit density at $\vec{r}$ [90, 95]. The benefit of this approach is that the exchange function of Jellium is known analytically and the correlation functional has been approximated to a high degree of accuracy [89]. The use of this functional is known as the Local Density Approximation (LDA) and it provides a simple and computationally fast approximation due to the local nature of the potential.

LDA is applied in many fields of condensed matter and is one of the most popular tools among the DFT community, however it has many limitations. As the system is modelled after Jellium it can only be applied to systems with uniform or slowly varying electron densities. One well documented failure of LDA is the treatment of strongly correlated systems where the electrons can not be well described through non-interacting auxiliary wavefunctions within a local potential, this is due to the high interaction and correlation among constituent particles. This failure is in part due to the single particle approach and the use of KS eigenvalues as electronic energies. However the local electron-electron interaction approximation is insufficient for strongly correlated materials [89, 90, 98].

Generalised-Gradient Approximation

After the initial proposal and success of the LDA method by Kohn and Sham, many new approaches were proposed to improve on LDA. One such method was the Generalised-Gradient Approximation (GGA), where by the exchange correlation potential is a functional of the local electronic density and its gradient. The expression for such functional can be given by

$$E_{xc}[\rho(\mathbf{r})] = \int d^3r \rho(\vec{r}) \epsilon_{xc}(\rho(\mathbf{r}), \nabla\rho(\mathbf{r})) \tag{3.20}$$

Although GGA functionals tend to agree well with each other for small gradient magnitudes, for the cases where the gradient of the electronic density is large the level of agreement is far less. In such cases GGA may even perform worse than the LDA approach. There are currently a wide range of GGA functionals with a variety of treatments for both cases of large and small density gradients [99, 100].

Hybrid Functionals

The approach which generally produces the best results from DFT calculations are hybrid functionals. In this approximation the exact exchange form from the Hartree-Fock theory is mixed with the exchange-correlation of some DFT functional. Hartee-Fock theory is an approach to solving the many-body Hamiltonian, in this approach the many-body wave-function of a system is approximated by a single Slater determinant of spin-orbitals. This approximation neglects correlation between electrons and leads to poor quantitative results for crystalline systems. Such methods result in better band gap agreement with experimental data. This is due to the over-

estimation of electron-electron interactions in the Hartree-Fock approach which is compensated for by the underestimation of eigenvalues intrinsic to local and semi-local density functionals as discussed [96, 101, 102].

Shortcomings of DFT

Density functional theory is the most popular method of calculating electronic properties, however as discussed previously DFT lacks a rigorous derivation for using the KS eigenvalues and eigenfunctions of the auxiliary system as those of the real system [89]. A well known consequence of this approach is the severe underestimation of fundamental band gaps in semiconductors. The severity of these errors varies for each material. Silicon's band structure can be calculated fairly well by DFT with only a systematic band gap problem; while some transition metal oxides which are in reality Mott insulators are predicted to be semiconductor or even metallic in certain cases. The origin of these inaccuracies are the insufficient treatment of the exchange-correlation contribution through local or semi-local functionals and the use of KS eigenvalues [96, 98, 103].

The band gap issue can be addressed by a judicial use of semi-empirical hybrid functionals. However the choice of the exchange-correlation functional is non-trivial and there exist many options tailored for a range of material. The result from different approximation can produce significant discrepancies, often it is not clear which potential is more suitable for a given system.

3.4 Many Body Perturbation Theory: A Green's Function Approach

A natural framework for electronic properties of materials is the many-body perturbation theory (MBPT) as it is explicitly a theory of excitations and excited systems. This method also benefits from a rigorous derivation for electronic eigenfunctions and eigenvalues. In the DFT approach the key parameter for calculations is the ground state density while in the MBPT counterpart, Green's functions are the key components. Green's functions are mathematical tools which are used to describe propagators in quantum field theory. As MBPT is extensively used through out this work an introduction to the Green's function approaches is provided in the following sections, more rigorous derivation has been provided by others [104, 105].

Green's Functions

In the second quantization approach the Hamiltonian of an n-electron system in a static potential is given by[4]

$$\hat{H} = \int d(\mathbf{x})\hat{\psi}^{\dagger}(\mathbf{x})h(\mathbf{r})\hat{\psi}(\mathbf{x}) + \frac{1}{2}\int d(\mathbf{x})d(\mathbf{x}')\hat{\psi}^{\dagger}(\mathbf{x})\hat{\psi}^{\dagger}(\mathbf{x}')\nu(\mathbf{r},\mathbf{r}')\hat{\psi}(\mathbf{x}')\hat{\psi}(\mathbf{x}) \tag{3.21}$$

where $\mathbf{x}$ specifies position ($\mathbf{r}$) and spin (σ) while $\hat{\psi}^{\dagger}$ and $\hat{\psi}$ represent the creation and annihilation field operators [105]. In equation 3.21 the one electron Hamiltonian $h(\mathbf{r})$ is given by

$$h(\mathbf{r}) = -\frac{\hbar^2}{2m}\nabla^2 + V(\mathbf{r}) \tag{3.22}$$

where $V(\mathbf{r})$ is a local static potential and $\nu(\mathbf{r},\mathbf{r}')$ is the Coulomb interaction. By introducing a static non-local potential $U(\mathbf{x},\mathbf{x}';t)$ the time-dependent field operators can be written within the interaction picture as

$$\hat{\psi}(\mathbf{x}) \equiv \hat{\psi}(\mathbf{x_1},t) = \exp(i\hat{H}t_1/\hbar)\hat{\psi}(\mathbf{x_1})\exp(-i\hat{H}t_1/\hbar) \tag{3.23}$$

with the interaction Hamiltonian $\hat{H}_I$ given by

$$\hat{H}'_I = \exp(i\hat{H}t_1/\hbar)\hat{H}'(t)\exp(-i\hat{H}t_1/\hbar) \tag{3.24}$$

$$= \int d\mathbf{x}d\mathbf{x}'\hat{\psi}^{\dagger}(\mathbf{x},t^{+})U(\mathbf{x},\mathbf{x}';\mathbf{t})\hat{\psi}(\mathbf{x}',\mathbf{t}) \tag{3.25}$$

where $t^{+} = t + \delta$ with $\delta \to 0$. By introducing a scattering operator

$$\hat{S} = \exp(-\frac{i}{\hbar}\int_{-\infty}^{\infty} dt\hat{H}'_I(t)) \tag{3.26}$$

it is possible to define the generalised one- and two-particle Green's functions as

$$G_1(\mathbf{1},\mathbf{2}) = -\frac{i}{\hbar}\frac{\langle N|\,T[\hat{S}\hat{\psi}(\mathbf{1})\hat{\psi}^{\dagger}(\mathbf{2})]\,|N\rangle}{\langle N|\,T[\hat{S}]\,|N\rangle} \tag{3.27}$$

$$G_2(\mathbf{1},\mathbf{2};\mathbf{1}',\mathbf{2}') = \big(-\frac{i}{\hbar}\big)^2\frac{\langle N|\,T[\hat{S}\hat{\psi}(\mathbf{1})\hat{\psi}(\mathbf{2})\hat{\psi}^{\dagger}(\mathbf{2}')\hat{\psi}^{\dagger}(\mathbf{1}')]\,|N\rangle}{\langle N|\,T[\hat{S}]\,|N\rangle} \tag{3.28}$$

where $\mathbf{1},\mathbf{2},\mathbf{3}\cdots$ represent 3 dimensions of space, and one dimension of spin and time. $|N\rangle$ is the ground state of an N-electrons unperturbed system and T is the Wick's time-ordering operator which ensures all creation operators are to the left of all annihilation operators in their product. The physical quantity calculated by equation 3.27 is the probability amplitude that an electron

[4] relativistic contributions have been neglected for the sake of simplicity

injected into the system at state **1** will be at state **2** after $t_2 - t_1$ (assuming $t_2 > t_1$, the order of processes are reversed), while equation 3.28 gives the two particle counterpart.

Through Fourier transformation and slight manipulation it is possible to write the one particle Green's function within the energy domain so that

$$G_1^0(\mathbf{r_1}, \mathbf{r_2}, \omega) = \sum_j \frac{\Phi_j^*(\mathbf{r_1}, \omega)\Phi_j(\mathbf{r_2}, \omega)}{\omega - E_j + i\delta} \tag{3.29}$$

where Φ is the eigenfunction with eigenvalue E_j. The poles of equations 3.29 correspond to energies of excited state system of $|N+1\rangle$ minus the ground state energy of $|N\rangle$.

Hedin's Equations

In his 1965 seminal paper Lars Hedin provided a derivation for an approach to obtaining the interacting Green's function of a system, this was through the five equations shown below:

$$G_1(1,2) = G_1^0(1,2) + \int d34 G_1^0 \Sigma(3,4) G_1(4,2) \tag{3.30}$$

$$\Sigma(1,2) = i \int d34 G_1(1,3) W(4,1) \tilde{\Gamma}(3,2,4) \tag{3.31}$$

$$\tilde{\Gamma}(1,2;3) = \delta(1,3)\delta(2,3) + \int d4567 \frac{\delta\Sigma(1,2)}{\delta G_1(4,5)} G_1(4,6) G_1(7,5) \tilde{\Gamma}(6,7;3) \tag{3.32}$$

$$\tilde{P}(1,2) = -i \int d34 G_1(1,3) G_1(4,1) \tilde{\Gamma}(3,4;2) \tag{3.33}$$

$$W(1,2) = \nu(1,2) + \int d34 \nu(1,3) \tilde{P}(3,4) W(4,2) d3 d4 \tag{3.34}$$

the equations above represent the Green's function, self-energy, vertex functional, polarisation operator and the screened Coulomb interaction respectively; in equation 3.30, $G_1^0(1,2)$ is the Green's function of a non-interacting system [104–106]. These equations which are derived from the equation of motion of the Green's functions describe the screening of the Coulomb interaction due to the presence of electrons, electron-hole interactions and the energy of the system among other quantities. Using these five coupled equations it is possible to calculate the self energy and the Green's function of an interacting system. The interacting equivalent of equation 3.29 would have the quasi-particle energy levels at its broaden peaks which replace the poles. Quasi-particles in this context are the screened electrons in semiconductors, which interact more weakly than their bare counterparts.

The first step in using Hedin's equations to calculate quasi-particle energy levels is to construct a starting non-interacting Green's function, the most common approach is to use KS

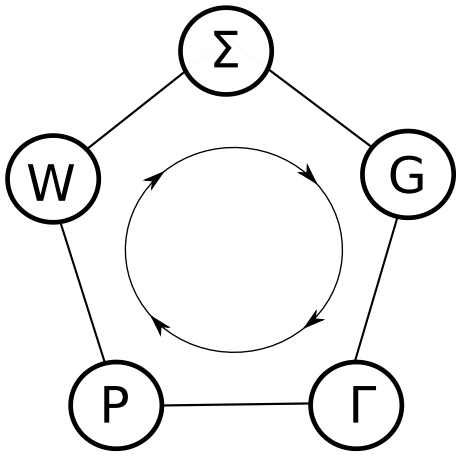

Figure 3.3: Hedin's pentagon showing the iterative method of solving the Hedin's equations

eigenfunctions and eigenvalues with equation 3.29. Once a guess starting Green's function is constructed the vertex function $\tilde{\Gamma}$ can be calculated through equation 3.32 which is in turn used to calculate the irreducible polarisability given by equation 3.33 and the screened Coulomb interaction from equation 3.34. From a screened W, the self energy can be obtained through equation 3.31 and hence using the Dyson's equation 3.30 a single particle interacting Green's function can be retrieved, this procedure is repeated till the point of self consistency, similar to DFT as previously discussed [107]. Figure 3.3 show the iterative process through Hedin's pentagon.

GW Approximation

Much like the Hohenberg-Kohn method outlined in section 3.3 the iterative approach described above is an exact method, however difficulty arises from the irreducible vertex function $\tilde{\Gamma}$. The numerical calculation of equation 3.32 for a given system is computationally highly expensive due to the recursive nature of the vertex. As a result the 0^{th}-order calculation of the Hedin equation is performed by neglecting the second term in equation 3.32. This approach is known as the GW approximation (GWA) and provides a practical method of using the Hedin equations [107]. As a result GWA calculates the screened Coulomb interaction within the random

phase approximation (RPA) [108–110]. GW approximation simplifies the 3-point vertex function in equation 3.32 to

$$\tilde{\Gamma}(1,2;3) = \delta(1,3)\delta(2,3) \tag{3.35}$$

and hence the irreducible polarisation is given by

$$\tilde{P}(1,2) = -i \int d34 G_1(1,2) G_1(2,1) \tag{3.36}$$

this approximation suggested by Hedin significantly reduces the difficulty in the iterative approach to Hedin's pentagon (figure 3.3) and makes the GW approximation feasible for realistic systems. In GWA electrons and holes independently interact with the system however electron-hole interactions are neglected.

Self-Consistency

Self-consistency in Green's function

The most common approach to self-consistency is to start from a non-interacting Green's functions which will be used to compute the iterative equations 3.31 to 3.34, finally computing equation 3.30 will produce a new interacting Green's function. This new Green's function which includes the self-energy serves as the input for the next iteration. This process is repeated until the point of self-consistency. The criteria for consistency can be a range of parameters such as eigenfunctions or eigenvalues. It is found that this approach of self consistency may in fact induce errors, as such partial self consistency or one-shot approaches are more commonly utilised [111].

Quasi-particle Self-Consistent GW

Another methods of obtaining self-consistency through the GW approach within RPA is the Quasi-particle self-consistent GW theory (QSGW) [112, 113]. The fundamental principal behind QSGW is to perturb the non-interacting Hamiltonian with the self-energy so that it will more closely resemble the interacting Hamiltonian. That is the self-energy obtained through equation 3.34 is used to construct a new non-interacting Green's function which will serve as the input for the next iteration. The exchange-correlation for the new non-interacting system

is obtained though:

$$V_{XC} = \frac{1}{2}\sum_{i,j} \langle \phi_i | \operatorname{Re}(\Sigma(E_i) + \Sigma(E_j)) | \phi_j \rangle \tag{3.37}$$

this expression for V_{XC} potential is obtained by minimising a norm parameter, which is a measure of $\Delta V = \Sigma - V_{XC}$ [112, 113]. Self-consistency is reached once the eigenstates from the initial non-interacting Green's function match those of the interacting system.

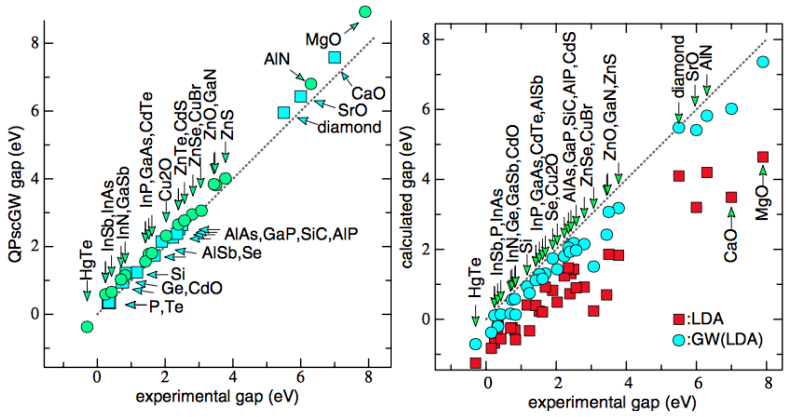

Figure 3.4: Fundamental gaps of zinc-blend (circles) and other compounds (squares) calculated through QSGW (left panel) and the through LDA (red squares) and GW_{LDA} (blue circles, left panel) [112].

This approach to self-consistency has shown better agreement with experimental measurements compared to LDA based GW calculations. As shown in figure 3.4 the error within the QSGW method is small. Furthermore unlike DFT based implementations of GW, this error is systematic and is due to the random phase approximation whereby the electron-hole interactions are neglected. This approach removes the dependency on the DFT method used for the starting Green's function. Hence different starting points result in identical final results.

Although QSGW has a higher level of accuracy compared to DFT and DFT based implementations of GW (partial or fully self-consistent), it is computationally far more expensive than both approaches. As such for large systems the use of QSGW over DFT or one-shot GW may not be practical.

Feasibility of the GW Approach

The Green's functions approach to band structure calculations has the advantage of a rigorous framework for excited state properties unlike DFT. Due to this, GW approaches generally have better agreement with experimental findings and discrepancies among different GW approaches are significantly smaller than those among different DFT approaches. However Green's functions methods are significantly more computationally expensive than DFT calculations, as a result applying GW methods to large systems is not always viable; systems which posses unit cells with more than ≈ 50 electrons become too computationally expensive for QSGW. However as a parameter free approach it can provide insight into properties of materials which may be missed through lower level theory methods such as DFT.

3.5 Spin-Orbit Interaction

Spin-orbit interaction (SOI) or spin-orbit coupling (SOC) are general terms used to describe a number of phenomena which arise from the coupling of the spin and the motion of the electron [114]. In the following sections a brief theoretical introduction to two types of this interaction are provided as their descriptions are highly related to the analysis of data in later chapters.

Spin-Orbit Coupling in centrosymmetric systems

The first case of SOC presented here occurs within systems which possess centrosymmetry, that is for every $\vec{k}$-point in the unit cell there exist an indistinguishable point $-\vec{k}$. Although the full derivation of this phenomena requires the use of the Dirac equation and quantum electrodynamics (QED) such description would be beyond the scope of this dissertation. However the qualitative description outlined below provides good agreement with observation.

In an atomic case without an external fields, in the rest frame of the nucleus there isn't a magnetic field; however in the frame of reference of a bound electron the electric field generated by the nucleons acts as an effective magnetic field given by

$$\vec{B} = -\frac{\vec{\nu} \times \vec{E}}{c^2} \tag{3.38}$$

where $\vec{\nu}$ is the velocity of the electron, $\vec{E}$ the electric field and c the speed of light in vacuum. The Hamiltonian for the interaction between a magnetic field and an electron is given by

$$H_{SOI} = g_s \mu_B \frac{\vec{S} \cdot \vec{B}}{\hbar} \tag{3.39}$$

where g_s is the electron g-factor, $\vec{S}$ is the spin angular vector and μ_B is the Bohr magneton describing the magnetic moment of an electron [89]. As the electric field in equation 3.38 is radial, the effective magnetic field can be written as

$$\vec{B} = \frac{\vec{r} \times \vec{\nu}}{c^2} \left| \frac{E}{r} \right| \tag{3.40}$$

similarly the velocity operator can be rewritten in terms of momentum so that

$$\vec{B} = \frac{\vec{r} \times \vec{p}}{m_e c^2} \left| \frac{E}{r} \right| \tag{3.41}$$

where $\vec{r} \times \vec{p}$ is the angular momentum ($\vec{L}$)of a particle, and hence the expression above can be rewritten as

$$\vec{B} = \frac{\vec{L}}{m_e c^2} \left| \frac{E}{r} \right| \tag{3.42}$$

Inserting equation 3.42 in expression 3.39, the Hamiltonian for the spin-orbit interaction of an electron bound to an atom in a centrosymmetric system is given by

$$H_{SOI} = g_s \mu_B \frac{\vec{S} \cdot \vec{L}}{\hbar m_e c^2} \left| \frac{E}{r} \right| \tag{3.43}$$

Such effects can often be neglected as only electrons with relativistic speeds experience appreciable perturbation to their energy levels, this can be readily seen from equation 3.38. In the case of heavier atoms and crystal with large constituents such effects can have significant impact on the electronic energy levels, this is due to higher velocity of electrons in heavier elements [115].

Rashba SOI

In systems which are non-centrosymmetric (i.e. lack inversion symmetry) more complex forms of spin-orbit interactions can be present. One such a phenomena is the Rashba splitting and unlike the SOC described above, within crystalline systems the band dispersion can also be significantly

effected [116, 117]. Rashba interactions have been previously studied for spintronic applications and in the context of quantum computers, however within the field of photovoltaic it is far less studied as this effect is only significant in heavy elements [118]. For solar cell applications the most important consequences of this SOI are the lifting of the band edge degeneracy, re-normalisation of the energy levels and shifting of the bands in $\vec{k}$-space as discussed below.

As mentioned previously one of the focuses of this dissertation is the significance of relativistic effects such as SOC on the power conversion efficiency of hybrid Perovskites, as such a brief theoretical overview of the Rashba effect is presented here.

Origin of the Rashba effect

Rashba interaction (also referred to as Rashba splitting) is due to the breaking of inversion symmetry and the presence of an electric field. This breaking of symmetry can be due to external or internal fields. A simple toy model description of the Rashba effect is presented below. Much like the discussion provided in the previous section, a full rigorous description of the Rashba interaction requires the use of Dirac equation and QED which are beyond the scope of this work. However the description below is sufficient for an intuitive insight, and will provide an aid to discussions in later chapters.

Toy model

To derive a toy model for the Rashba contribution to the Hamiltonian we start by adding a term which breaks the symmetry of the system, in this case an electric field along the z axis given by:

$$H_E = -E_0 \hat{z} \tag{3.44}$$

As described in the previous sections electrons moving through an electric field at relativistic speeds experience an effective magnetic field in their frame of reference, where this magnetic field is described by equation 3.38. Unlike the case in the previous section the electric field here does not possess spherical symmetry and is taken to be along $\hat{z}$. This effective $\vec{B}$ will interact with electrons' spins introducing an additional spin dependent term to the Hamiltonian, such that the Rashba Hamiltonian is written as:

$$H_R = \frac{g_s \mu_B}{2c^2} (\vec{v} \times \vec{E}) \cdot \vec{S} \tag{3.45}$$

this can be rewritten as

$$H_R = \frac{g_s \mu_B}{2c^2}(\vec{\sigma} \times \vec{p}) \cdot \hat{z} E_0 \tag{3.46}$$

by explicitly rewriting the vectors the interaction Hamiltonian reduces to

$$H_R = \frac{g_s \mu_B E_0}{c^2}\left(\begin{bmatrix} \frac{1}{2}\hbar\sigma_x \\ \frac{1}{2}\hbar\sigma_y \\ \frac{1}{2}\hbar\sigma_z \end{bmatrix} \times \begin{bmatrix} p_x \\ p_y \\ p_z \end{bmatrix}\right) \cdot \begin{bmatrix} 0 \\ 0 \\ 1 \end{bmatrix} = \alpha_R(\sigma_x p_y - \sigma_y p_x) \tag{3.47}$$

where $\vec{\sigma} = (\vec{\sigma_x} \quad \vec{\sigma_y} \quad \vec{\sigma_z})^T$ and $\vec{\sigma_x}, \vec{\sigma_y}, \vec{\sigma_z}$ are the three Pauli spin matrices and α_R is known as the Rashba parameter and is a measure of the strength of the spin orbit interaction, this parameter is proportional to the strength of the electronic field [116, 117].

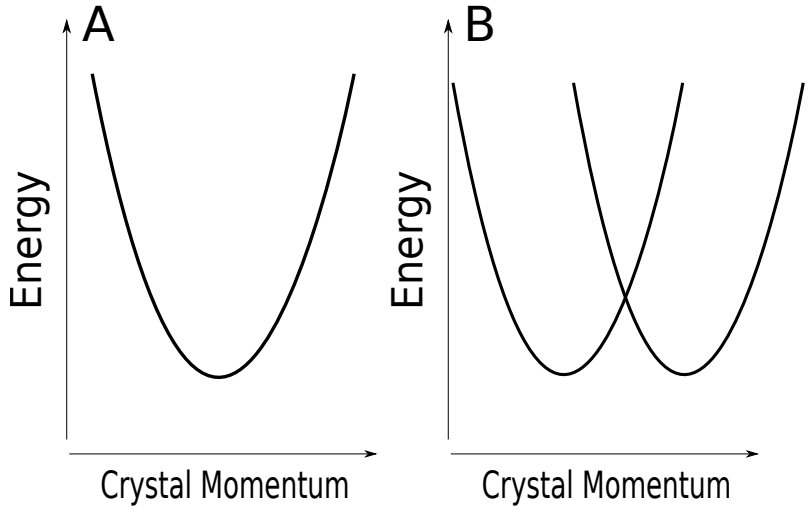

Figure 3.5: Schematics showing doubly degenerate conduction bands in the cases of without (A) and with (B) Rashba splitting. In the left panel two bands overlap, this is equivalent to $E_0 = 0$ in equation equation 3.44, as E_0 increases the bands split in opposite directions from the original minima, this shift can be seen from equation 3.48.

By computing H_R the energy contribution from the Rashba effect to the system becomes

$$E_R = \pm\alpha_R\sqrt{(k_y^2 + k_x^2)} \tag{3.48}$$

where the $\pm$ is related to the two possible spins of the electron.

The Rashba interaction can significantly effects the electronic band structure by transforming the doubly degenerate parabolic bands to two non-degenerate parabolic bands shifted from previous minima position in momentum space. Such transformation is shown in figure 3.5; such modification is anticipated from equation 3.48, furthermore it can be seen that this breaking of symmetry leads to

$$\epsilon(\vec{k})_{\uparrow} \neq \epsilon(\vec{k})_{\downarrow} \tag{3.49}$$

$$\epsilon(-\vec{k})_{\uparrow} = \epsilon(\vec{k})_{\downarrow} \tag{3.50}$$

Along with the dispersion of the bands the Rashba effect also changes the spin texture of the bands near the band edge. Such deformations have important effects for processes involving spin flip and carrier relaxation and are highly relevant to the field of spintronics; spin texture will be discussed in chapter 5 within the context of photovoltaics.

3.6 Optical Properties

The optical properties of materials determine the interactions of the material with light, and hence are of utmost importance for theoretical description and predictive calculations for photovoltaic materials. For photovoltaic applications the optical properties are used to determine the optimum thickness of the material for complete solar capture and the most appropriate architecture of devices (single junction, tandem...). Theoretical calculation of optical properties of a material is performed by calculating the strength of the coupling between a ground and an excited state due to the presence of a perturbing electromagnetic field.

The following subsections will provide a brief theoretical background to the calculation of optical properties, furthermore a number of approximations and approaches utilised are discussed.

Optical Transition

The interaction of a bulk material and a light field can be modelled using perturbation theory, this approach provides an expression for the rate of transition from an initial state (valence band in bulk semiconductors) to an excited state (conduction band in bulk semiconductors) [114].

All the optical properties of a material can be accessed through the complex index of refraction and the complex dielectric function. As these two functions are derived from the same processes it is possible to obtain one from the other. From perturbation theory it is possible to obtain an expression for the imaginary part of the dielectric function, this expression is given by:

$$\epsilon_i(\omega) = (2\pi e)^2 \sum_{\vec{k}} |P_{i,f}|^2 \delta(\hbar\omega - \hbar\omega_f - \hbar\omega_i) \tag{3.51}$$

where in equation 3.51 $P_{i,f}$ is the matrix elements which measures the coupling between the initial and final eigenstates due to the perturbing field. The term $\delta(\hbar\omega - \hbar\omega_f - \hbar\omega_i)$ ensures the energy of the photon absorbed is equal to the energy difference of the two states and hence conserving total energy. The sum in equation 3.51 is over the reciprocal space (first BZ in practice), as $\vec{k}$ is an essential quantum number in the case of crystalline material as mentioned previously. Equation 3.51 can be utilised within the single particle approach, however it is possible to calculate the imaginary part of the dielectric function using

$$\epsilon_m \equiv \lim_{q\to 0} \frac{1}{\epsilon^{-1}_{\mathbf{G}=0,\mathbf{G}'=0}} \tag{3.52}$$

where ϵ_m is the macroscopic dielectric function and ϵ^{-1} is given by

$$\epsilon^{-1} = [1 - \nu(\mathbf{q})P(\mathbf{q},\omega)]^{-}1 \tag{3.53}$$

where $P(\mathbf{q},\omega)$ is the non-interacting polarisation for reciprocal space vector $\mathbf{q}$, excitation angular momentum ω and $\nu(\mathbf{q})$ is the bare Coulomb interaction. Although both equations 3.53 and 3.51 are equal (in the case of $P(\mathbf{q},\omega) = 1$) the latter approach is more suited for implementation within the Green's functions approach as the same machinery is utilised, equation 3.53 also takes into account the screening of charges by electrons.

Using the Kramers-Kronig relation:

$$\chi_r(x) = \frac{1}{\pi}\mathcal{P}\int_{-\infty}^{\infty} \frac{\chi_i(x')}{x'-x}dx' \tag{3.54}$$

$$\chi_i(x) = \frac{-1}{\pi}\mathcal{P}\int_{-\infty}^{\infty} \frac{\chi_i(x')}{x'-x}dx' \tag{3.55}$$

where $\mathcal{P}$ is the Cauchy principal value, it is possible to relate the imaginary χ_i and real χ_r parts of complex analytic functions; hence the real part of the complex dielectric function can be obtained using equations 3.51 and 3.54 [119].

As mentioned previously it is possible to calculate the real and imaginary parts of the index of refraction through the complex dielectric function, these parameters are related through:

$$n = \sqrt{\frac{\sqrt{(\epsilon_r^2 + \epsilon_i^2)} + \epsilon_r}{2}} \tag{3.56}$$

$$\kappa = \sqrt{\frac{\sqrt{(\epsilon_r^2 + \epsilon_i^2)} - \epsilon_r}{2i}} \tag{3.57}$$

where κ and n are the imaginary and real parts of the complex index of refraction respectively. One of the crucial properties of materials for photovoltaic device engineering is the absorption coefficient given by

$$\alpha = \frac{4\pi\kappa}{\lambda} \tag{3.58}$$

This parameter is used to determine the optimum thickness for complete solar capture.

Direct and Indirect Bands

In bulk materials there are two class of optical transitions known as direct and indirect transitions. During a direct transition the crystal momentum associated with the electron is unchanged. Indirect transitions are phonon assisted transitions, this type of photo-excitation of electrons is indicated by a change in the in the crystal momentum of the electron. The change in momentum is due to an interaction between the electron and a phonon, this transfer of momentum from the electron to the lattice ensures conservation of momentum. Schematic diagram 3.6 shows direct and indirect optical transitions.

As indirect transitions are phonon assisted, the rate of excitation is lower and hence indirect transitions can often be ignored (unless there exist a large phonon population). Due to the slower rate of indirect transitions solar cells with indirect band gap semiconductors such as silicon have much thicker absorber layer compared to direct band semiconductors like GaAs, this is to ensure sufficient solar capture. Equations 3.53 and 3.51 only calculate transitions where $\vec{k}$ in the initial and final states are equal and hence indirect transitions are neglected [114].

Dipole Matrix Element for Local and Non-local Hamiltonian

The dipole matrix element in equation 3.51 measures the coupling of the valence and conduction bands in the presence of a light field. In equation 3.51 the matrix element is written within the

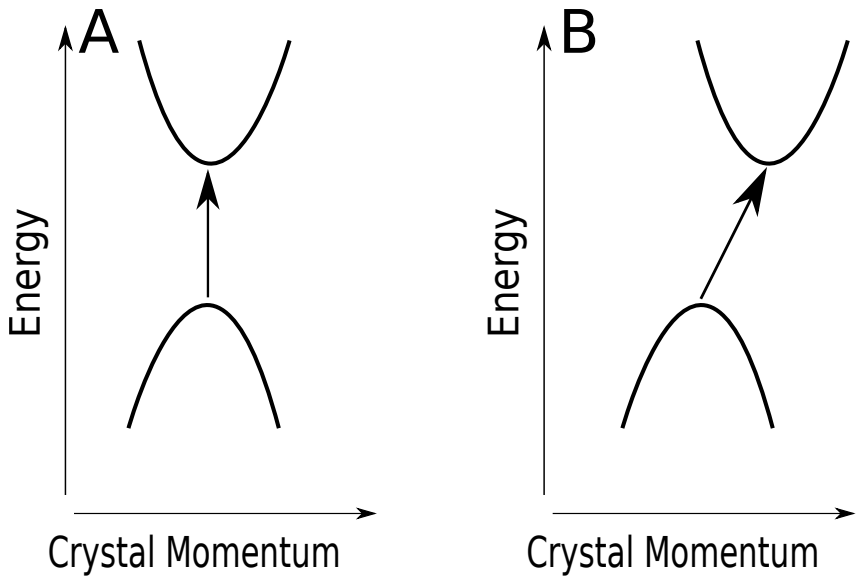

Figure 3.6: Schematic diagrams for direct (**A**) and indirect (**B**) optical transitions. Indirect transitions are important in the case of indirect band semiconductors where the conduction band minimum and valence band maximum occupy different points in k-space.

so called length gauge, that is

$$P_{i,f} = \lim_{q\to 0} \frac{1}{q} \langle c, \mathbf{k}+\mathbf{q}| \, e^{i\mathbf{q}\cdot\mathbf{r}} \, |v, \mathbf{k}\rangle \tag{3.59}$$

where for computational calculations $\vec{q}$ is set to a value close to zero. This numerical approximation may result in numerical instability and produce nonsensical results if the value of $\vec{q}$ is too small. If the $\vec{q} >> 0$ an error will be induced in the numerical results as the transitions computed are not truly direct. As such using the expression above for the dipole matrix element is not ideal. It is possible to rewrite this in terms of the velocity operator which is computationally more desirable, this can be achieved through

$$\mathbf{v} = \frac{d\mathbf{r}}{dt} = \frac{i}{\hbar}[\hat{H}, \mathbf{r}] \tag{3.60}$$

and due to the relation $\mathbf{v} = \frac{\mathbf{p}}{m}$ the dipole transition matrix can be written in momentum gauge, that is

$$\lim_{q\to 0} \frac{1}{q} \langle c, \mathbf{k}+\mathbf{q}| \, e^{i\mathbf{q}\cdot\mathbf{r}} \, |v, \mathbf{k}\rangle = \frac{1}{m_e\omega} \langle c, \mathbf{k}| \, \hat{\mathbf{e}}\cdot\mathbf{p} \, |v, \mathbf{k}\rangle \tag{3.61}$$

where the $\lim_{q\to 0}$ is handled analytically. Substituting the RHS of equation 3.61 into equation 3.51 gives

$$\epsilon_i(\omega) = \left(\frac{2\pi e}{m_e\omega}\right)^2 \sum_{\vec{k}} |\left\langle c,\mathbf{k}\right| \hat{\mathbf{e}}\cdot\mathbf{p}\left|v,\mathbf{k}\right\rangle|^2 \delta(\hbar\omega - \hbar\omega_f - \hbar\omega_i) \tag{3.62}$$

although this expression can be calculated without numerical approximations it is only valid for local Hamiltonians. In the case of non-local Hamiltonians (such as QSGW) the so called momentum gauge form of the dipole matrix is no longer equal to correct position or velocity gauge forms, this can be seen through the relation

$$\mathbf{v} = \frac{\mathbf{p}}{m} + \frac{i}{\hbar}[V^{NL}(\mathbf{r},\mathbf{r}'),\mathbf{r}] \tag{3.63}$$

where V^{NL} is the non-local contribution to the Hamiltonian. Calculations using the velocity gauge are not ideal due to the high computational cost arising from the non-local term [120]. Equation 3.62 does not include the non-local contributions to the dipole transition probability and hence will underestimate the imaginary part of the dielectric function which can be used to calculate all other parameters as discussed.

calculating the dipole transition matrix using the LHS of equation 3.61 has the benefit of being applicable to non-local potentials, however the numerical approximation induces a degree of error in the calculated results; furthermore compared to the RHS of equation 3.61 this method is slower as calculations need to be preformed for pairs of $\vec{k}$ and $\vec{k}+\vec{q}$ instead of only $\vec{k}$ for the momentum gauge approach. Additionally the optical matrix implemented in equation 3.62 has the advantage of taking $\lim_{\mathbf{q}\to\mathbf{0}}$ analytically and it is computationally faster, however as it is not applicable to non-local potentials it is not practical for realistic systems. The ideal approach will combine the advantages of both expressions, that is to take the $\lim_{\mathbf{q}\to\mathbf{0}}$ analytically and be computationally fast while being suitable for non-local potentials.

To include the non-local contributions to the dipole transition matrix in the momentum gauge it is possible to use an approximate form. With the assumption that the eigenfunction of the system of interest within local and non-local potential are similar, it is possible to use the following expression:

$$\begin{aligned}\lim_{q\to 0}\frac{1}{q}\left\langle c^{NL},\mathbf{k}+\mathbf{q}\right| e^{i\mathbf{q}\cdot\mathbf{r}}\left|v^{NL},\mathbf{k}\right\rangle = \lim_{q\to 0}\frac{1}{q}\sum_{c^{LDA},v^{LDA}}\left\langle c^{NL},\mathbf{k}+\mathbf{q}\right| \left|c^{LDA},\mathbf{k}+\mathbf{q}\right\rangle \left\langle v^{LDA},\mathbf{k}\right| \left|v^{NL},\mathbf{k}\right\rangle \\ \times\left(\frac{E_c^{NL}-E_v^{NL}}{E_c^{LDA}-E_vLDA}\right)\frac{\left\langle c^{LDA},\mathbf{k}\right| \hat{\mathbf{e}}\cdot\mathbf{p}\left|v^{LDA},\mathbf{k}\right\rangle}{E_c^{LDA}-E_v^{LDA}}\end{aligned} \tag{3.64}$$

where local and non-local eigenfunctions and eigenvalues are indicated with LDA and NL superscripts respectively. In equation 3.64 the matrix element is calculated using local eigenfunctions for which the momentum gauge is valid, to include the non-local contributions the matrix element is scaled by the difference of the eigenvalues of the local and the non-local Hamiltonians [121]. For systems where the non-local contribution has minimal effect on the electron density this approximation is valid. A detailed derivation of this approximation is provided in appendix B.

Chapter 4

Opto-electronic Properties of Hybrid Perovskites

4.1 Overview

In this chapter the electronic and optical properties of a number of hybrid Perovskites are presented. Beginning with a brief discussion of the computational set-up and crystal structures used throughout this thesis. The band gaps, trends and the effects of spin-orbit coupling are identified. From the electronic eigenfunctions and eigenvalues of the hybrid Perovskites the imaginary part of the dielectric functions are calculated. The complex refraction indices for MAPI, MAPB and MAPC are compared with ellipsometry data which were obtained through collaborative work. These verifications will be used to validate the *ab initio* results obtained and enable further analysis of the optical properties with confidence. Finally transient absorption spectroscopy (TAS) is simulated, the findings are used to interpret experimental data by accessing information which are not possible through experimental methods.

4.2 Computational Set-up

The crystal structures used for hybrid Perovskites throughout this thesis were obtained by Walsh *et al.* and have been reported previously [66, 122, 123]. Structural optimisations were

performed using the VASP package with the PBEsol functional [124, 125]; due to the good agreement between the experimental and predicted cell structures using non-relativistic PBEsol approaches, higher level of theories are not necessary.

The band structure calculations were performed using an all electron implementation of QSGW as provided through the Questaal package [112,113,126]. The self-energies were obtained on a $3 \times 3 \times 3$ k-mesh, more dense $\vec{k}$-meshes were utilised for the band structure and optical properties; The use of denser k-meshes for optical and band structure (between $12 \times 12 \times 12$ and $18 \times 18 \times 18$) calculations was to ensure k-convergence. Increasing the $\vec{k}$-mesh to $4 \times 4 \times 4$ for the calculation of the self energy affects the band gap by less than 0.1 eV while leaving the band dispersions fairly unperturbed. Relativistic effects were added as a one-shot correction to the final densities.

The high symmetry points within the first Brillouin zone are label following the guidelines provided by reference [127]. Furthermore diagrams depicting this convention for cubic, tetragonal and orthorhombic are shown in appendix C

4.3 Results: Electronic Band Structures

MAPI

At room temperature the crystal structure of MAPI can be approximated by a pseudo-cubic

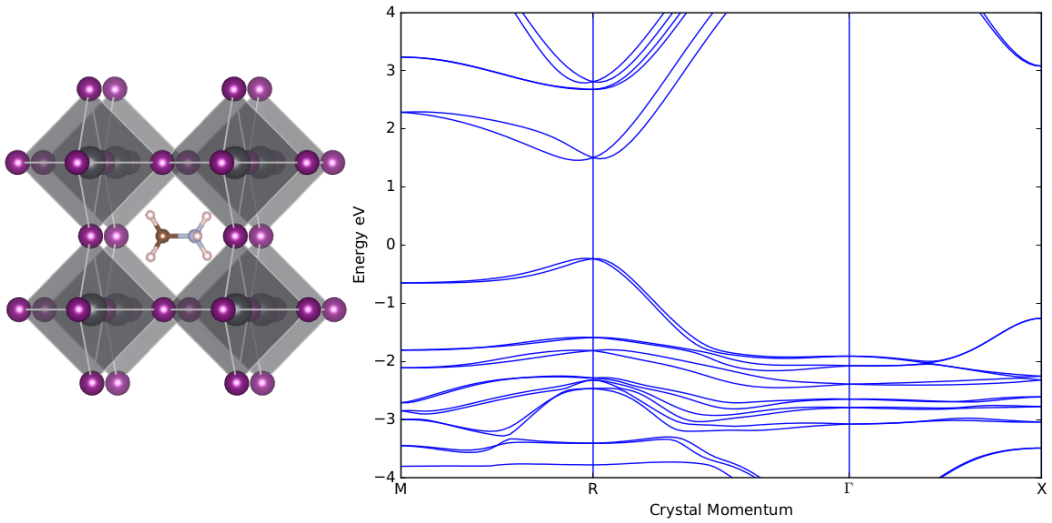

Figure 4.1: The pseudo-cubic unit cell (left) and quasi-particle electronic band structure (right) of $NH_3CH_3PbI_3$ with the C-N bond along $\langle 100 \rangle$.

crystal with experimental lattice constant $a = 6.26$Å [43,62,122]. As outlined in section 2, three local minima for $NH_3CH_3^+$ alignment are found. The quasi-particle band structure for these three crystal structures are shown in figures 4.1 and 4.2.

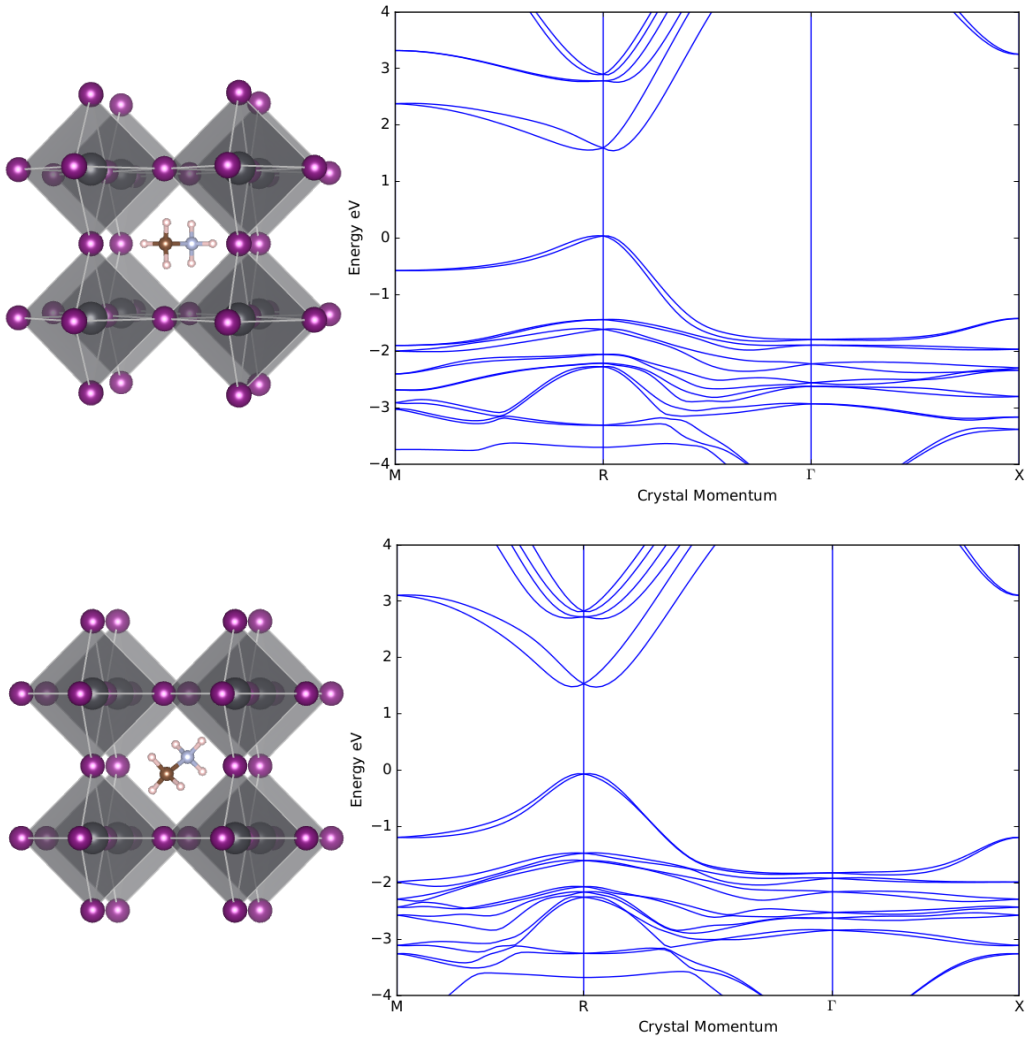

Figure 4.2: The pseudo-cubic unit cells (left) and quasi-particle electronic band structures (right) of $NH_3CH_3PbI_3$ with the C-N bond parallel to $\langle 110 \rangle$ (top) and C-N bond parallel to $\langle 111 \rangle$ (bottom).

In MAPI, the top valence band is formed of mainly I5p orbital while the bottom conduction band consists of majority Pb6p and a small contribution from Pb6s, with the former domi-

nating the band edge. The organic molecule forms dispersionless bands deep in the valence and conduction bands, suggesting the role of MA^+ in MAPI is mainly structural and charge compensation. However the orientation of the organic moiety effects the energy levels of the band edges. The three variations of MAPI have fundamental band gaps of 1.68 eV, 1.53 eV and 1.59 eV corresponding to $MAPI_{\langle 100\rangle}$, $MAPI_{\langle 110\rangle}$ and $MAPI_{\langle 111\rangle}$ respectively. As the organic molecule rotates rapidly, the band structure of MAPI also changes in time.

Contrary to band structures calculated through DFT the band dispersions around the band edges are not flat, especially in the direction of R$\rightarrow \Gamma$ [128].

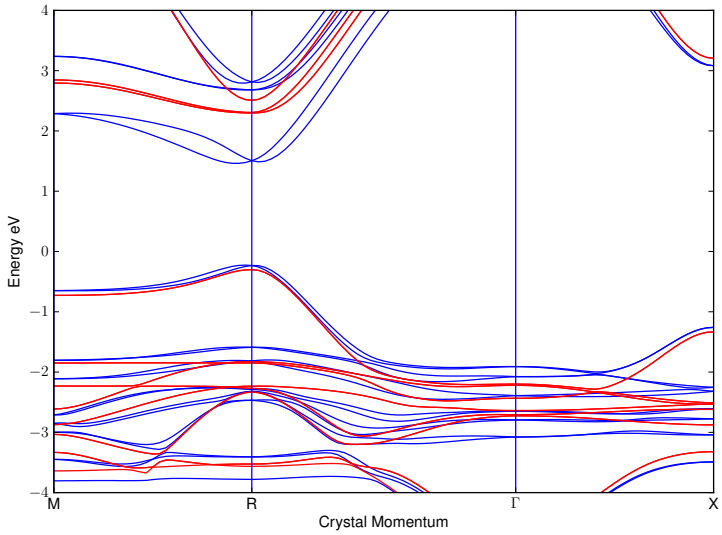

Figure 4.3: Quasi-particle electronic band structures of $NH_3CH_3PbI_3$ with the C-N bond parallel to $\langle 100\rangle$ with SOC included (blue) and without SOC contributions (red). SOC reduces the band gap by $\approx$1eV and significantly perturbs the band edge dispersions for both the conduction and valence bands.

In MAPI due to the heavy nature of lead and iodine the inclusion of SOC is extremely important. In fact spin-orbit effects can account for approximately $\sim$1eV of the band gap, this is shown in figure 4.3. Additionally the SOC significantly perturbs the band dispersion of both the conduction and valence band edges. An accurate description of the band dispersions is important as quantities such as effective masses and optical parameters are strongly dependent on it.

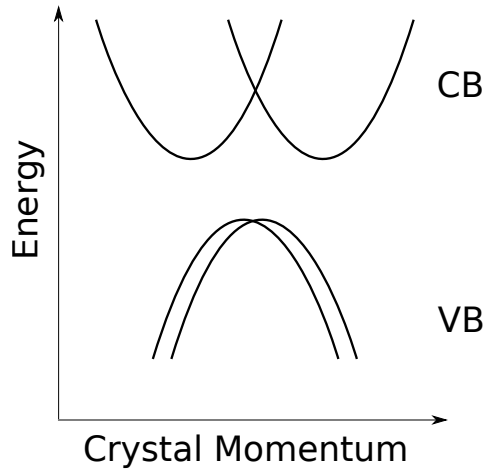

Figure 4.4: Schematic diagram of the band edge perturbation in MAPI due to the Rashba splitting.

Early local and semi-local density functional based band structure reports of MAPI which did not include spin-orbit coupling resulted in band gaps which were fortuitously close to the experimental values [1, 129]. This was due to the cancellation of errors from the severe underestimation of LDA and overestimation of the band gap due to the lack of SOC, both of which amounted to $\sim$ 1eV [128, 130].

Along with the significant narrowing of the band gap due to relativistic effects, the Rashba splitting adds perturbation to the conduction band minimum. This effect is also present in the valence band, however to a significantly lower degree. This is due to the heavier nature of lead based lowest conduction band compared to the mostly iodine top valence band; as mentioned previously the Rashba splitting is present to a larger degree in heavier atoms due to the more relativistic nature of these systems. The mismatch between the degree of splitting in the conduction and the valence band results in an indirect band gap. Figure 4.4 shows a schematic diagram of the conduction and valence band edges for MAPI.

The Rashba splitting produces two antipodes shifted away from the high symmetry R $\vec{k}$-point. The contour plot in figure 4.5 shows the deformation of the conduction band edges; similar plots for $\text{MAPI}_{<110>}$ and $\text{MAPI}_{\langle 111 \rangle}$ show that the conduction band minimum (CBM) and the valence band maximum (VBM) both change in value and position in reciprocal space

with the rotation of MA^+. As mentioned in section 3.5 Rashba phenomena exists due to the presence of an internal electric field which breaks centrosymmetry. In the case of MAPI this potential is attributed to the dipole moment of the organic molecule and the distortion of the inorganic cages.

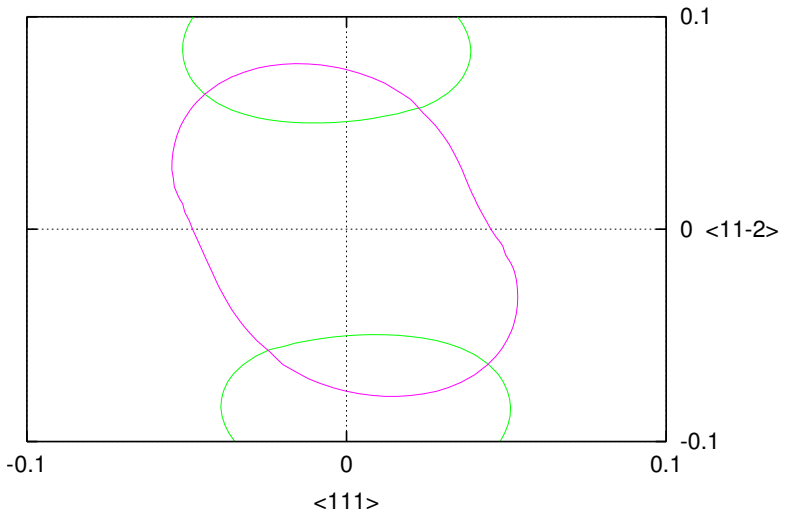

Figure 4.5: Contour plots of band edges of pseudo-cubic MAPI with MA^+ aligned along $\langle 100 \rangle$. The red and green lines correspond to $\approx k_B T_{RT}$ away from the conduction and valence band edges respectively.

As temperature decreases the pseudo-cubic approximation to the tetragonal form becomes invalid. The tetragonal unit cell consists of 48 atoms, it can be thought of as a $\sqrt{2} \times \sqrt{2} \times 2$ super-cell of the pseudo-cubic phase with additional stretching of the lattice constant along $\vec{z}$ and inorganic cage distortions. At temperatures just below 200K the motion of the organic molecules are significantly reduced compared to the room temperature case [131]. This reduction in the reorientation rate is due to the decreasing thermal energy and tilting of the inorganic cages which restrict the movement of MA^+. The quasi-particle band structure for the tetragonal phase of MAPI is shown in the top panel of figure 4.6. Within the tetragonal phase the band gap is at Γ, this deviation from the pseudo-cubic phase is due to the increase in the real space unit cell which results in band folding from R$\rightarrow \Gamma$.

Due to the lack of centrosymmetry, similarly to the pseudo-cubic phase the tetragonal MAPI

possess a Rashba splitting. However the effects of the splitting are less prominent. In this larger

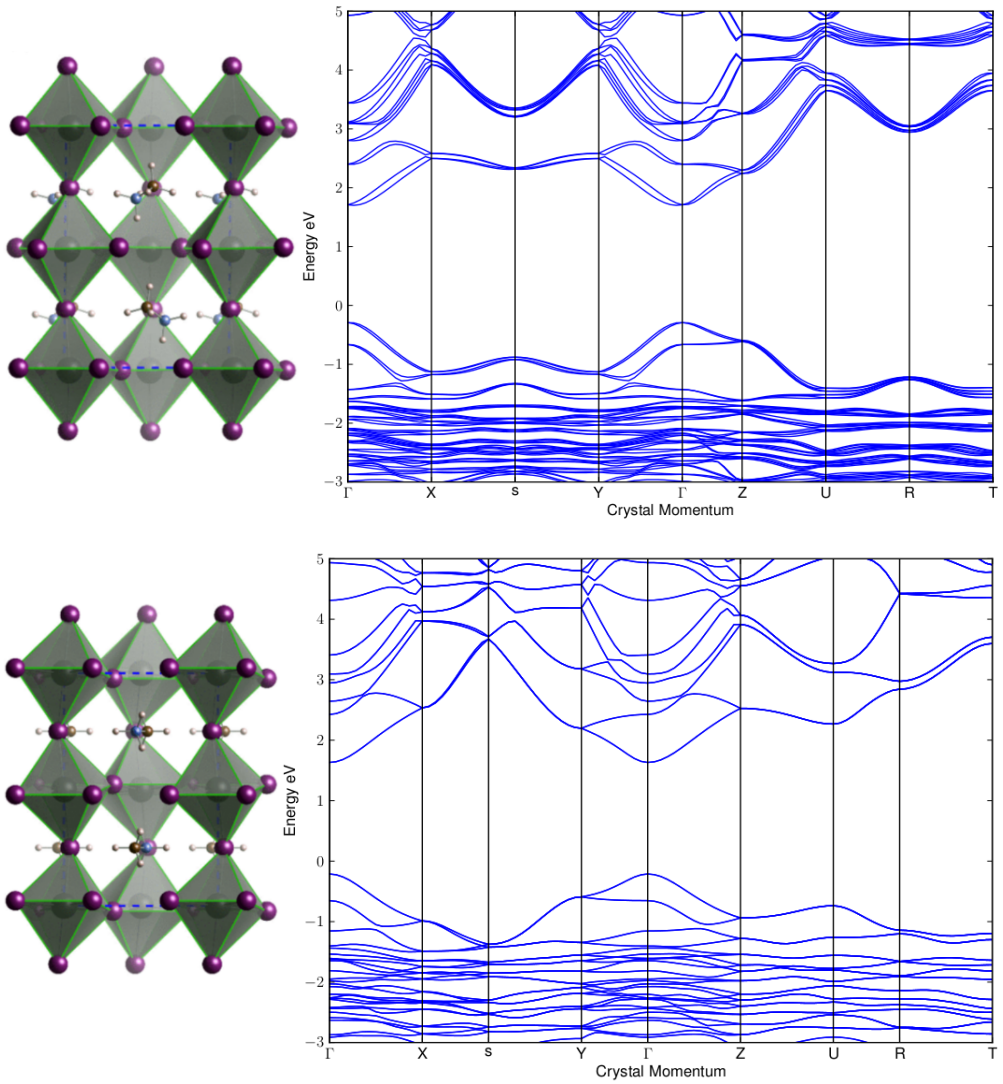

Figure 4.6: The unit cells and QSGW electronic band structures for tetragonal (top) and orthorhombic (bottom) MAPI phases (unit cell figures obtained from reference [132]).

unit cell the MA^+ molecules can be misaligned with respect to other organic molecules and hence effectively screen one another, reducing the total electric field present at the lead site. The reduction in the electric field reduces the Rashba splitting as discussed in chapter 3. The

misalignment of the organic molecules within the unit cell is contrary to the three structures used for pseudo-cubic calculations, where perfect alignment of the organic molecules throughout the sample was present.

The calculated band gap in the tetragonal phase is ∼2 eV, this is higher than the predicted pseudo-cubic band gap. This finding is larger compared to experimental measurements of the fundamental gap of 1.5-1.61 eV [133, 134]. As observed for the three orientations of MA^+ within the pseudo-cubic phase, the band gaps of these materials are strongly correlated with the orientation of the organic molecule within the unit cell. Experimental methods measure the average of the system, while predictive methods use a temporarily stationary sample of a unit cell within the bulk material. Additionally QSGW is known to overestimate band gaps (as shown in figure 3.4), mostly because of missing ladder diagrams in the polarisability.

MAPI undergoes a first order transition from tetragonal to an orthorhombic structure around 165K. In the low temperature orthorhombic Perovskite phase, the organic molecules are aligned with long range periodicity [61]. This arrangement reinstates inversion symmetry which the tetragonal and pseudo-cubic phases lack. Due to the presence of inversion symmetry the Rashba Splitting can not exist as discussed in chapter 3.

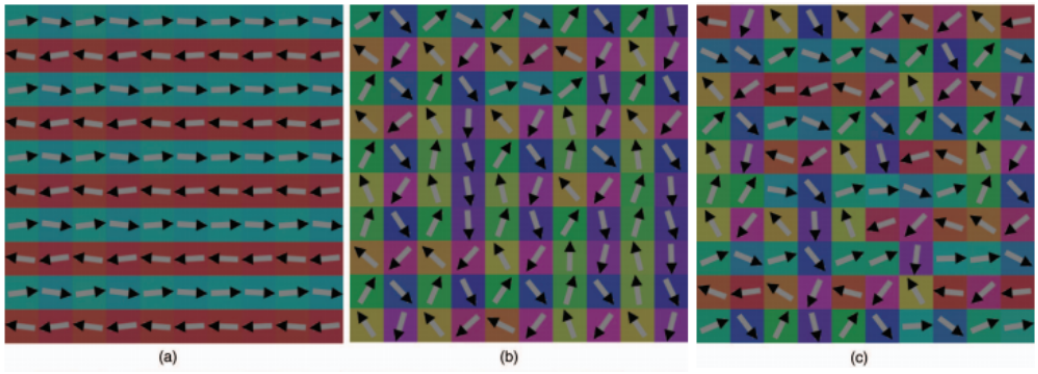

Figure 4.7: Molecular dynamic simulation of MA^+ alignment in MAPI at oK(a) 100K(b) and 300k(c). In the orthorhombic phase the organic molecules align to form an antiferromagnetic phase(figure taken from ref [135])

The orthorhombic Perovskite phase in MAPI has a predicted band gap of 1.84eV at the Γ point, this is slightly overestimates measured optical band gap as expected [133]. The quasi-

particle band structure of orthorhombic phase of MAPI is shown in bottom panel of figure 4.6.

MAPB and MAPC

As mentioned, in hybrid lead halide Perovskites the unit cell size decreases with lighter halogen constituent [43]. Both MAPB and MAPC posses pseudo-cubic structures at room temperature with lattice parameters 5.68Å and 5.92Å for MAPC and MAPB respectively (a pseudo-cubic hybrid Perovskite structure is shown in figure 4.8) [123]. In MAPB and MAPC the motion of the organic molecules is significantly more restricted compared to MAPI, and hence in this section only the most stable orientations of MA^+ are considered. The decreases in the bond length between the metal and halogen results in an increase in the fundamental band gaps, this is similar to to the case of III-V semiconductors [8, 136].

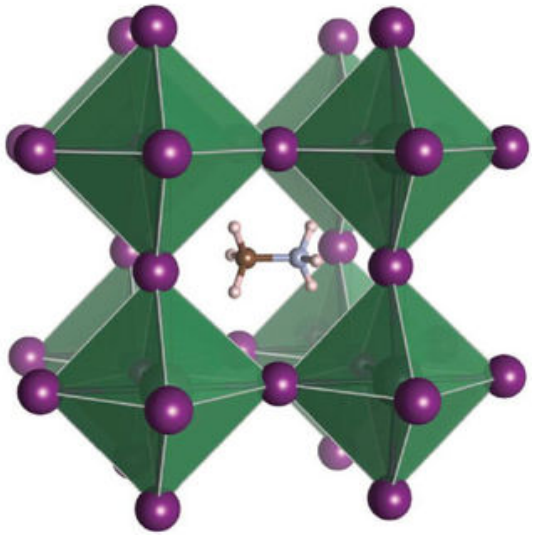

Figure 4.8: Pseudo-cubic hybrid Perovskite structure possessed by both MAPB and MAPC at room temperature. The reduced lattice parameter significantly restricts the motion of the organic molecule [65].

The calculated band gaps of MAPB and MAPC are 2.57eV and 3.44eV respectively. Figure 4.9 shows the quasi-particle band structures of MAPB and MAPC. The Rashba splitting is present in the conduction band of both Perovskites, however due to the significantly lighter nature of Cl and Br the splitting in the halogen based valence bands are negligible.

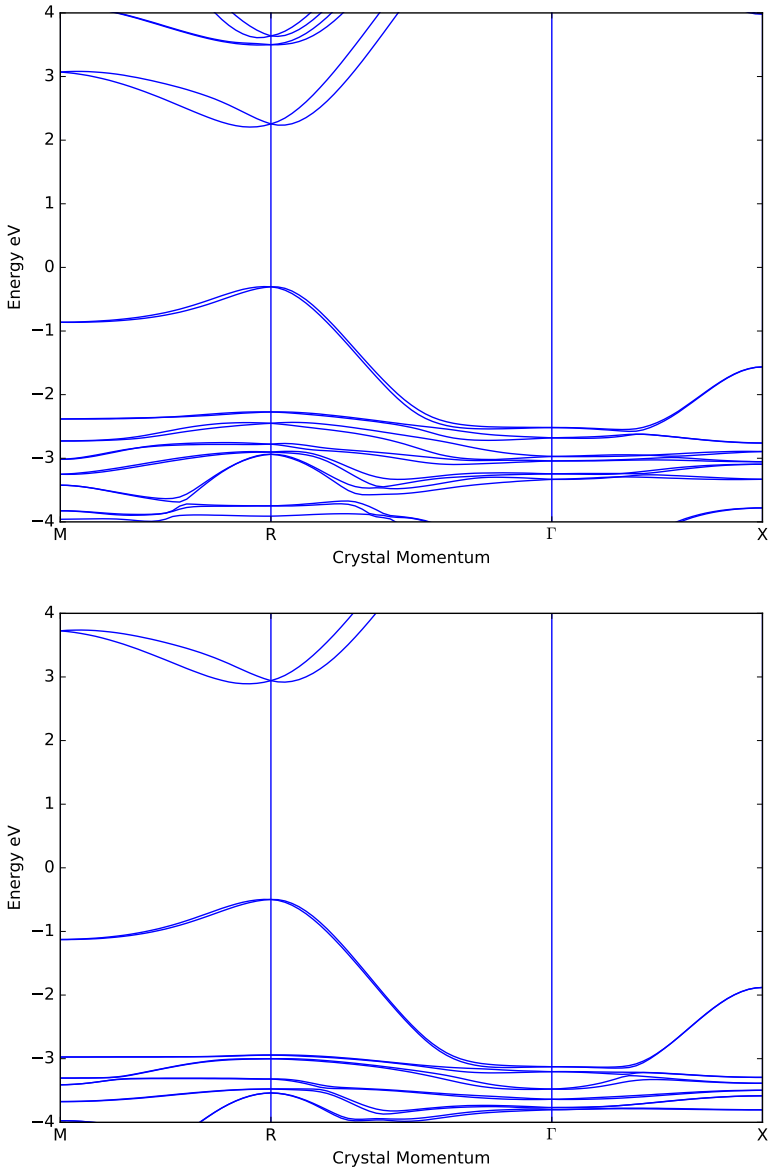

Figure 4.9: QSGW electronic band structure of MAPB (top) and MAPC (bottom) in their room temperature phase.

FAPI

At room temperature FAPI has a pseudo-cubic structure similar to MAPI; however the methylammonium molecule is replaced by the larger formamidinium (FA^+) molecule which has a

dipole moment 10 times smaller than that of MA^+ [66].

Much like the case of MAPI the bottom conduction band is mostly metallic while the highest valence band is formed of halide orbitals. Owing to the increase in the unit cell size compared to MAPI (lattice constant change from $a = 6.26$Å to $a = 6.362$Å), in FAPI the band gap decreases, the calculated band gap is 1.63eV, this value overestimates the experimental optical gap by 0.2eV[1]. This follows the relation between the cell and band gap sizes observed with regards to halide substitutions, discussed in the previous sections.

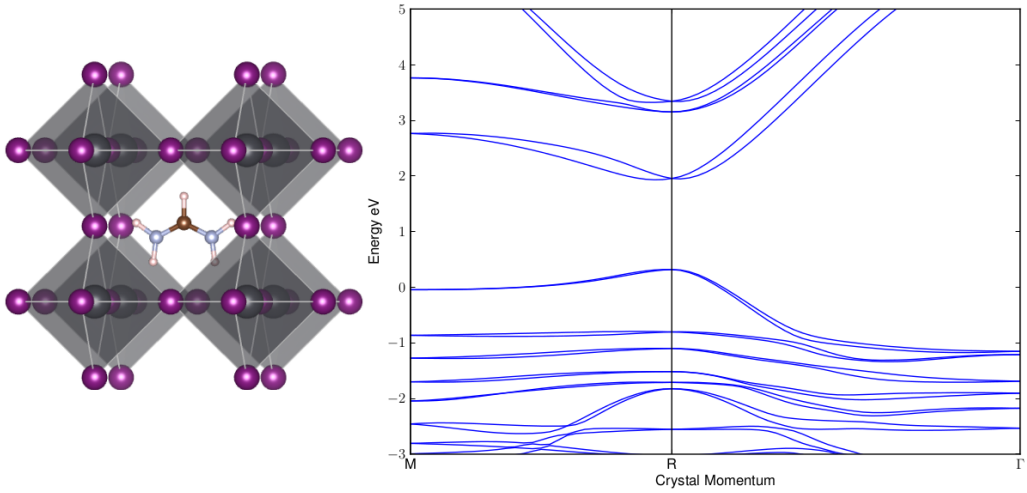

Figure 4.10: Pseudo-cubic unit cell and QSGW electronic band structure of FAPI in it's room temperature phase.

The Rashba splitting present in FAPI is comparable to that in MAPI, in spite of the much smaller dipole moment on the organic moiety (Table 2.3). This establishes that the distortion of the inorganic cages, may be the dominant contribution to the internal electric field that generates Rashba splitting, even in MAPI. This also suggests that a large atomic ion such as Cs in place of an organic moiety will give rise to a similar splitting [137].

[1]The self-energy for FAPI was calculated on a $4 \times 4 \times 4$ mesh

4.4 Results: Optical Properties

Optical Parameters

In this section the optical properties for the crystal structures from the previous section are presented. All calculations include SOC; also $\vec{k}$-mesh convergence for optical parameters was checked for all calculations, a mesh density of $18 \times 18 \times 18$ was employed. Additionally the imaginary part of the dielectric function was calculated for a range bigger than 175 eV to ensure Kramers-Kronig relation produced an accurate real part of dielectric function.

Theoretical Data

Much like the electronic band structure calculations from the previous section, the optical properties of MAPI are presented for the three orientations of the MA^+ ion. This enables us to observe the effects of the moieties' rotation on the band structure.

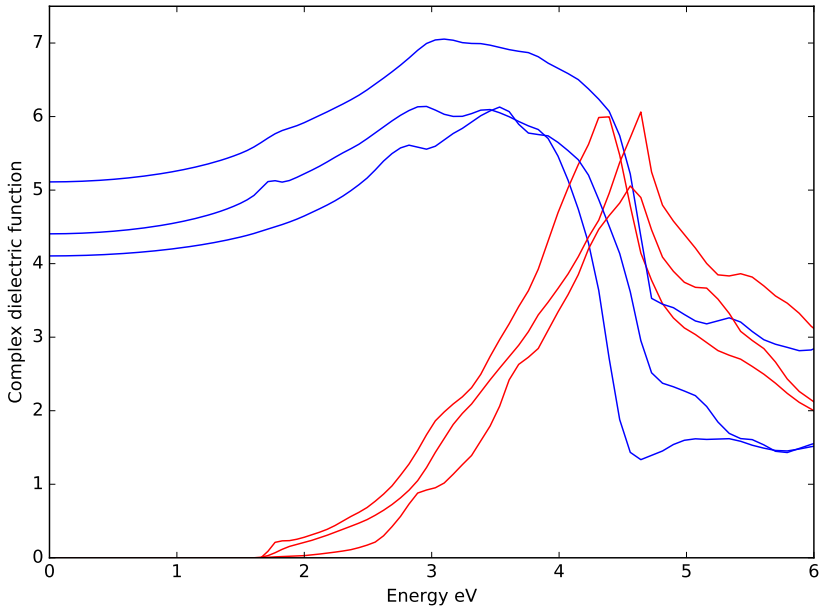

Figure 4.11: The real (blue) and the imaginary (red) parts of the complex dielectric function of $MAPI_{\langle 100 \rangle}$.

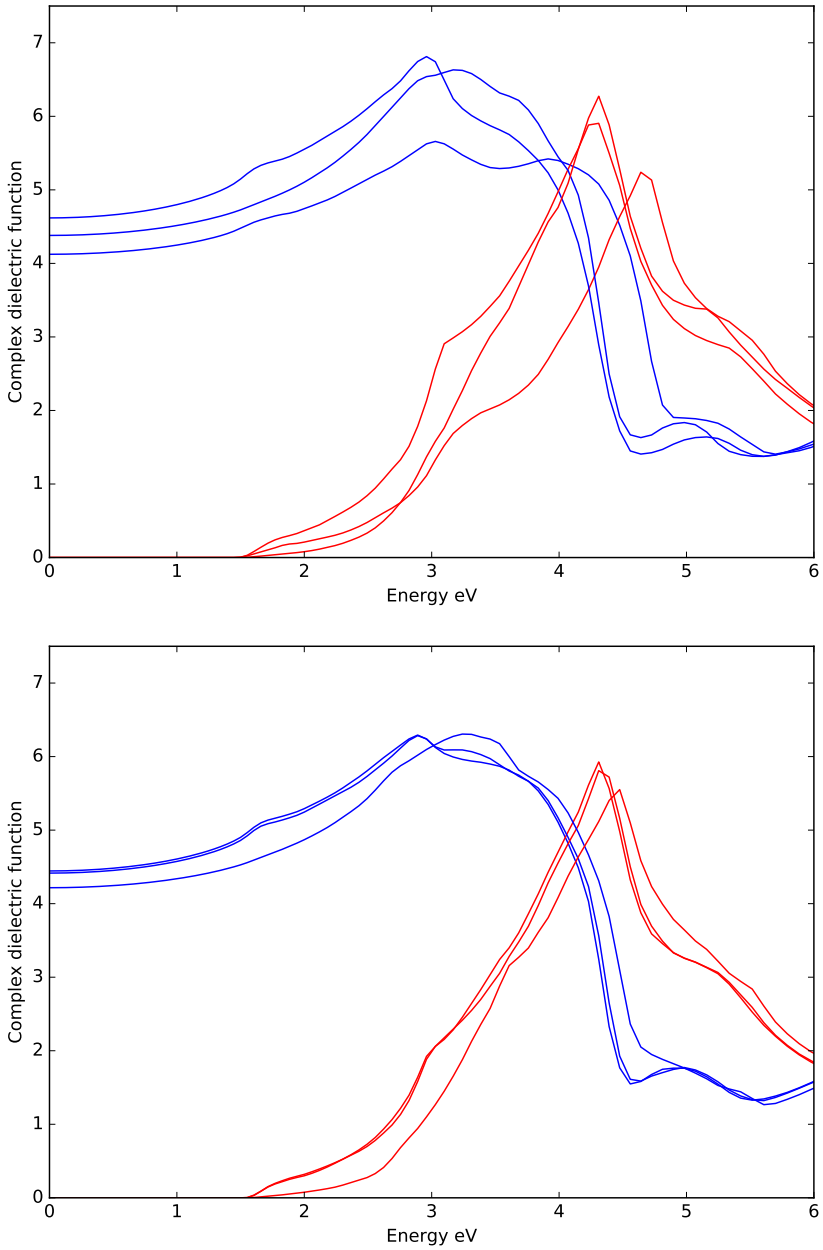

Figure 4.12: The real (blue) and the imaginary (red) parts of the complex dielectric function of $MAPI_{<110>}$ (top) and $MPI_{\langle 111 \rangle}$ (bottom).

The real and imaginary parts of the dielectric functions for MAPI are shown in figures 4.11 and 4.12. Owing to the presence of the organic molecules, MAPI has a pseudo-cubic structure

at room temperature: deviations from cubic symmetry will generate anisotropy in the optical response. Indeed we find that the intensity and the nature of the anisotropy is highly dependent on the orientation of MA^+. Anisotropy is also observed for MAPB, MAPC and FAPI. As previously suggested the local band gaps within crystal grains can vary owing to the short range alignment of the organic molecules. Figures 4.11 and 4.12 show that the same is true for spatial anisotropy of optical properties. Hence temporal local variations of both electronic and optical properties are intrinsic to organic-inorganic hybrid Perovskites.

The calculated imaginary part of the dielectric function for all the Perovskites show a sharp peak at the absorption edge, which has also been observed experimentally [138]. While such peaks may resemble excitonic excitations, electron-hole contributions are not included within the RPA framework. In this calculation the sharp peak is caused by the high density of states at the conduction band edge as a result of the Rashba splitting.

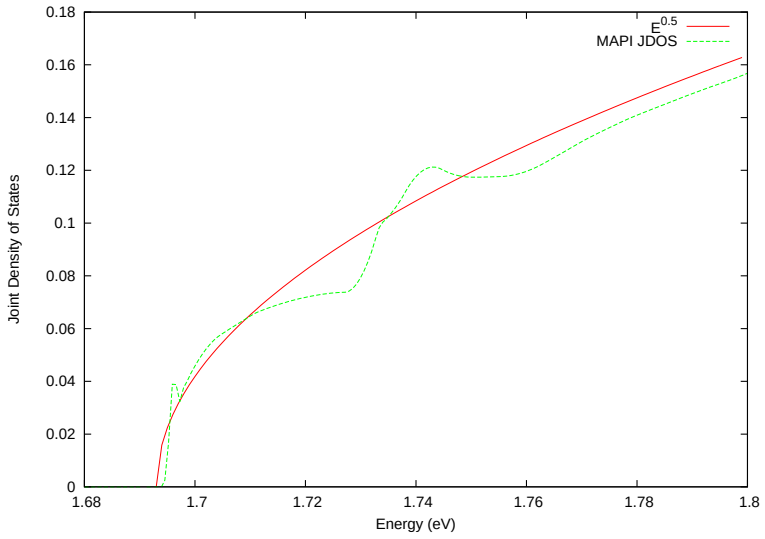

Figure 4.13: Joint density of states of $MAPI_{\langle 100 \rangle}$ (green) and parabolic bands (red) for transitions just above the band gap (1.68 eV). The Rashba splitting significantly perturbs the JDOS and enhances the absorption transitions at the band edge compared to standard parabolic bands.

Figure 4.13 shows the joint density of states for $MAPI_{\langle 100 \rangle}$ just above the band gap. Joint density of states gives the density of direct transitions possible from the valence band to the conduction band for a given energy per unit cell. The deviation from the $\sqrt{E}$ dependence on the JDOS, as occurs with direct band semiconductors with parabolic band edges, is apparent. The high density of states above the fundamental gap originate from the Rashba splitting of the bands, effectively widening the valley at the band edges. Similar properties are observed for MAPB, MAPC and FAPI, all of which have similar Rashba splitting in the conduction band.

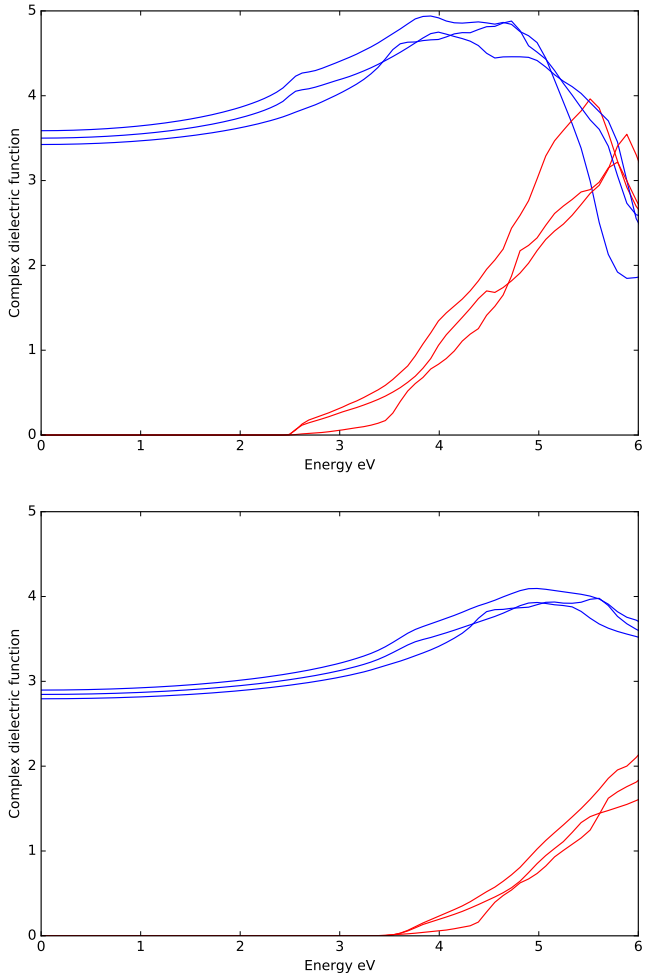

Figure 4.14: The real (blue) and the imaginary (red) parts of the complex dielectric function of MAPB (top) and MAPC (bottom).

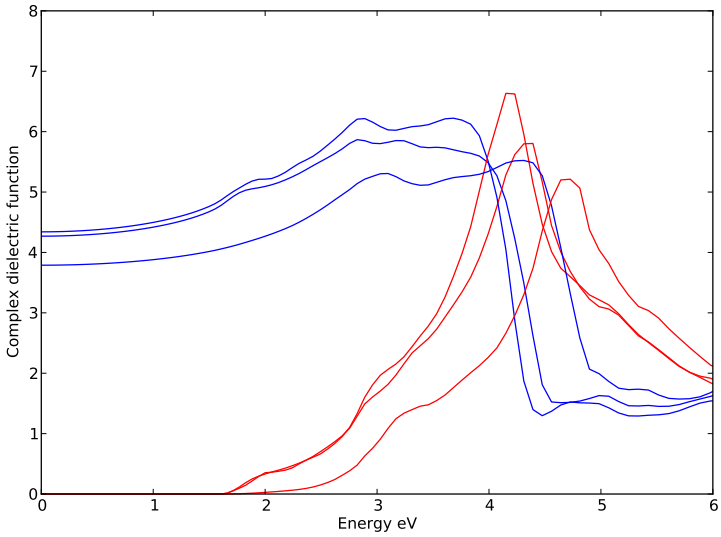

Figure 4.15: The real (blue) and the imaginary (red) parts of the complex dielectric function of FAPI.

Figure 4.16 shows the absorption coefficient of these Perovskites together with GaAs serving as a point of reference. Although the absorption coefficient of MAPI and FAPI are below that

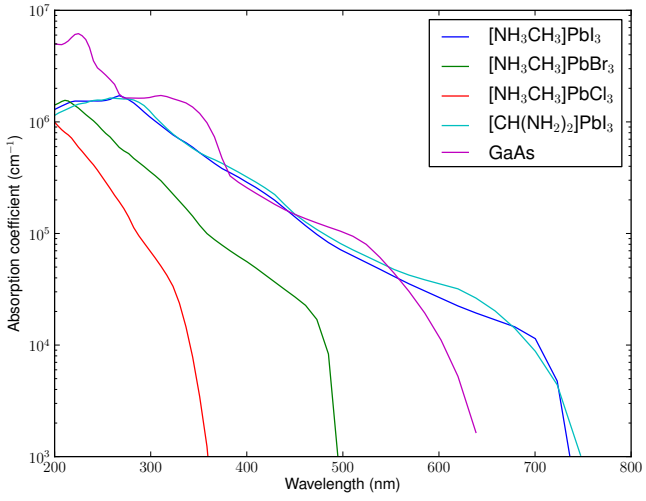

Figure 4.16: Absorption coefficient for a number of OIHP and GaAs.

of GaAs, they are nevertheless comparable. MAPB and MAPC, have absorption coefficients comparable to MAPI and FAPI, their larger band gaps render them less suitable for single junction PV applications.Among these materials GaAs currently has the highest efficiency certified for thin film solar cells (28.8%) while the highest Perovskite efficiency is recorded at 22.7% [7].

Comparison with experimental data

In the discussion that follows the energy bands above the band gap are referred to as CB_1, CB_2, $\cdots$, and the energy bands below the band gap are referred to as VB_1, VB_2, $\cdots$. A comparison between the optical constants of $MAPbX_3$ (X=Cl, Br, I) calculated from QSGW (orange dotted line) and those obtained by ellipsometry (solid blue line) are presented in figure 4.17. Qualitatively, both the shape and amplitude of the calculated spectra of n and κ show good agreement with experimental findings [1].

For MAPI the predicted band gap energy is 1.6 eV(Average of the three orientations of the organic molecule), close to the $1.5 - 1.6$ eV obtained experimentally without the introduction of any empirical parameters. The calculated QSGW band gaps are expected to be slightly over estimated, this is due to the exclusion of higher order diagrams in the self-energy as discussed in chapter 3. The computed and experimental extinction coefficient spectra show the same number of features in the visible spectral range. In figure 4.17 the features in the theoretical spectra are less well resolved than their experimental counterparts. This is because the optical properties calculated for different cation alignments and electric field polarisations have been averaged. The average is calculated based on the population ratio of each unit cell configuration within large samples, the weighting are based on molecular dynamic simulation preformed by Frost *et al.* [135][2].

The calculated optical constants for each material shows a blue shift of the optical features relative to the experimental values (a 'stretching' of the curves towards higher energies). This phenomenon is also attributed to the use of RPA. A better match between theory and experiment would be achieved by adding ladder diagrams to the RPA bubbles. The additional diagrams are thought to only slightly reduce the self-energy while having a far more pronounced effect on the dielectric function, as electron-hole pairs get attracted through the screened coulomb interaction W. This is discussed by Louie and Rohlfing in ref. [139]. They show that the blue

[2]At room temperature 42% of MA^+ molecules are aligned along the $< 100 >$, 31% along $< 110 >$ and 26% along $< 100 >$

shift resulting from the omission of electron-hole interactions in GW can exceed 0.5 eV in the case of Si, while it is as high as a few electron volts for LiF.

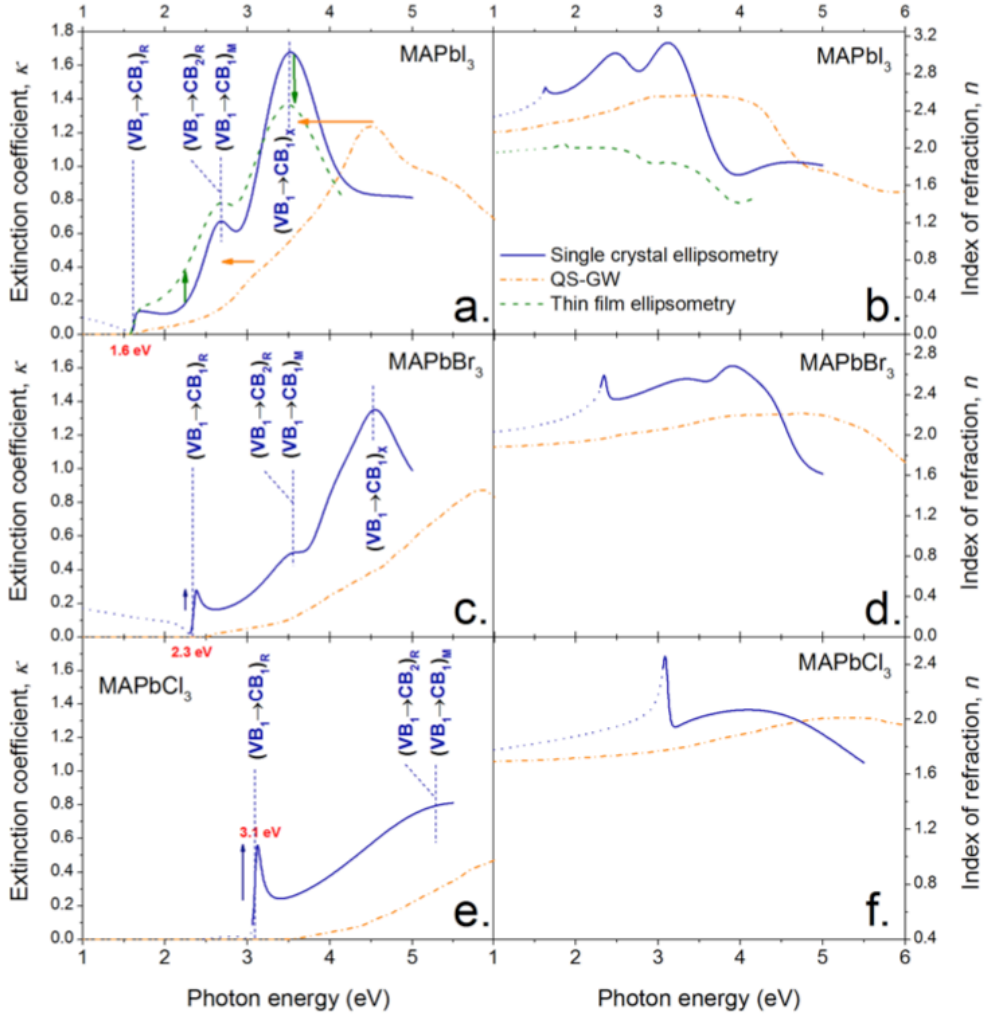

Figure 4.17: Optical constants (extinction coefficient (a, c, e) and index of refraction (b, d, f)) of $CH_3NH_3PbI_3$ (a and b), $CH_3NH_3PbBr_3$ (c and d) and $CH_3NH_3PbCl_3$ (e and f) derived from single crystal ellipsometry (solid blue lines), thin film $CH_3NH_3PbI_3$ (dashed green lines) and theory (chained orange lines). The three main optical features of $CH_3NH_3PbI_3$ are assigned to the appropriate inter-band transitions. The subscripts outside the brackets designate the symmetry point where the transition occurs in the first Brillouin zone, as defined in figure 4.18 [1].

The sharp absorption feature observed at the band edge in all three materials within the experimental data results from a discrete excitonic state enhancing absorption in this region. It should be noted again that the electron-hole interactions are not accounted for in QSGW and thus it cannot reproduce such feature. This accounts for the weaker computed absorption onset at the band edges for MAPI, MAPB and MAPC.

The discrepancies between optical constants determined by ellipsometry compared to the QSGW ones are larger for lighter halides. This larger error is consistent with the observed increase in exciton binding energies with lighter compounds, which indicates a larger contribution of electron-hole coupling to the opto-electronic properties of Perovskites [140–143]. This increase in the exciton binding energy is most likely due to a reduction in the static dielectric function with lighter halide, this decreases the screening of electron-hole pairs [144].

Due to the instability of FAPI experimental optical measurements are not reliable in its pure phase. However FAPI has similarly low excitonic binding energy as MAPI, hence electron-hole contributions are expected to be small [141]. As such the agreement of FAPI calculations with measurements should be comparable with MAPI's agreement.

Agreement between the theoretical and experimental data show that QSGW can be used to confidently describe the electronic and optical properties of hybrid Perovskites, specially ones with larger halides. The discrepancies observed between the theoretical and experimental data are systematic and can be addressed by the addition of higher order diagrams in the self energy calculations.

Band Assignment

Taking into account the omission of ladder diagrams, the quality of the agreement between the experimental and theoretical findings for MAPI enables unambiguous assignment of the three main optical features to their corresponding inter-band excitations routes.

The energy differences between conduction and valence bands are plotted in figure 4.19 (left panel) for different band pairs. Extrema of the curves in reciprocal space, where the conduction and valence band energies are close to parallel, correspond to critical points (CPs) of the joint density of states. Points where the conduction and valence bands track each other (i.e. where the gradient $\nabla_{\mathbf{k}}(E_c - E_v)$ is minimal) dominate the dielectric function.

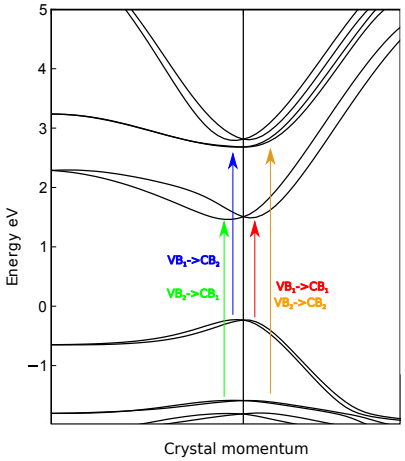

Figure 4.18: The band to band optical transitions for MAPI.

The right panel of figure 4.19 shows the contribution to the imaginary part of the dielectric function from three key transitions. In the figure above only direct transitions for valence and conduction band pairs are accounted. Notably it shows that the transition from the highest valence band VB_1 to the lowest conduction band CB_1[3] accounts for almost the entirety of the dielectric function.

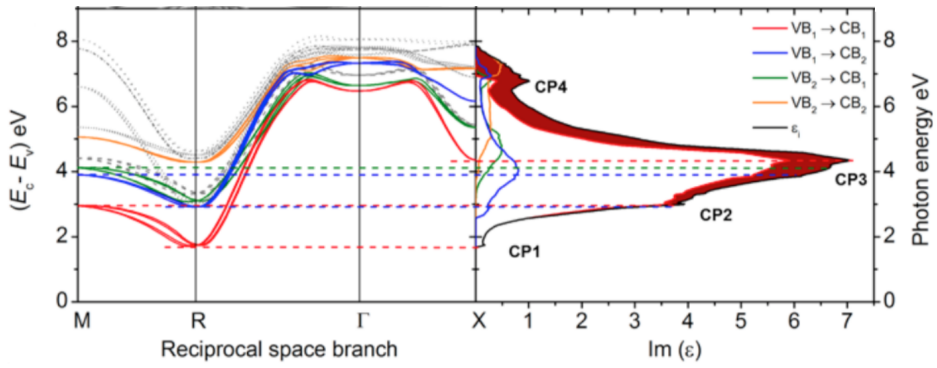

Figure 4.19: Band-to-band contributions to dielectric function for MAPI (right) and the origin of the CPs with in reciprocal space(left).

Additionally the right panel of figure 4.19 highlights the CPs for MAPI and their origin

[3] CB_1 and VB_1 each contain two spins.

in reciprocal space. Identification of CPs is important for interpretation of ellipsometry data. Although the parameters used within the final model are often different to theoretical findings, they can serve as a good starting point, as was done here.

Transient Absorption Spectroscopy

Transient absorption spectroscopy (TAS) measures the change in optical absorption of a material between an initial state without any excited electrons, and a secondary state where a number of electrons (holes) have been excited to the conduction (valence) band. Measurements are taken at time intervals to investigate carriers' relaxation dynamics. Although the main aim of experimental TAS is to characterise carrier relaxation, identification of the bands involved is non-trivial. Band assignment is the motivation behind theoretical TAS which can be used to interpret experimental data more accurately. To simulate TAS the imaginary part of the dielectric function is initially calculated using equation 3.51 which gives the expression for the imaginary part of the dielectric function for a system at equilibrium. The equilibrium state ϵ_{cv} is then compared with

$$\begin{aligned} \epsilon^*_{cv}(\omega_{cv}) &= (\frac{2\pi e}{m\omega})^2 \Sigma_{\vec{k}} |P_{cv}|^2 \delta(E_c(\vec{k}) - E_v(\vec{k}) - \hbar\omega_{cv}) \\ &\times [1 - f_n(E_c(\vec{k}, k_B T, n_0))][1 - f_p(E_v(\vec{k}, k_B T, n_0))] \end{aligned} \tag{4.1}$$

giving $\Delta\epsilon_{\omega_{cv}} = \epsilon_{cv}(\omega_{cv}) - \epsilon^*_{cv}(\omega_{cv})$ where $(1 - f_n(E_c(\vec{k}, k_B T, n_0)))$ and $(1 - f_p(E_v(\vec{k}, k_B T, n_0)))$ give the probability of a hole being in the conduction band and electron in the valence band for a given $\vec{k}$-point, temperature and excited carrier density n_0. The Fermi-Dirac distribution functions f_n and f_p (for electrons and holes, respectively) are only dependent on the density of photo-excited carriers n_0 and the temperature T which govern the quasi-Fermi levels for the carriers. This approach of calculating TAS data accounts for effects due to the electronic structure and the carrier population; however, it does not model the relaxation of the crystal structure due to the presence of excited carriers. Additionally, the excited electrons and holes are assumed to be thermally relaxed within their respective bands and form Fermi-Dirac distribution with distinct quasi-Fermi levels for each band.

To obtain the simulated TAS spectra, the DOS was calculated on a $120 \times 120 \times 120$ $\vec{k}$-mesh which enabled accurate calculations related to the number of electron (holes) in the conduction (valence) bands. The optical calculations were performed on a $30 \times 30 \times 30$ $\vec{k}$-mesh as this

provided sufficient resolution for the purposes of this calculation. Such dense k-mesh is necessary to capture the contribution and consequences of the band edge states which are perturbed by the Rashba splitting both in the DOS and optical calculations. Assuming a value for the photo-excited carrier density, the quasi-Fermi levels can be calculated for a given temperature. The absorption spectra for the system at equilibrium was also calculated using equation 4.1 without excited carriers. For the system with excited carriers the quasi-Fermi levels at room temperature for 10^{-5} carriers per unit cell were calculated. The calculation of quasi-Fermi levels is discussed in the next chapter.

Results

Figure 4.20 shows the simulated transient absorption spectrum and the relative contributions from different optical transitions for an electron density of 10^{-5} per unit cell ($\approx 4 \times 10^{16}$ cm^{-3}).

The simulated spectrum shows bleaching features at around 1.72 eV and 2.9 to 3.1 eV, that is a reduction in photoabsorption after excitation. These are likely to correspond to the main photobleach features observed experimentally at 1.63 eV and 2.58 eV [145,146]. Our calculations show that the low energy bleach is exclusively due to the population of photo-generated charges in VB1 and CB1 at the R point as expected. The second bleach at higher energy is likely to be due to a combination of transitions involving the VB_1 to CB_2, VB_2 to CB_1 and VB_1 to CB_3. The ratio of these three contributions are dependent on the excitation energy and intensity. This also implies that the relative magnitude of the bleach signal PB_2 will be greater immediately following a short wavelength excitation pulse ($\approx$2.6eV)) compared to excitation with a longer wavelength pulse close to the band gap. This is because directly after excitation with short wavelengths, PB_2 will have contributions from both the depletion of the electronic states at the top of VB_1 and VB_2 and by the filling of CB_1, CB_2 and CB_3. Thermalisation of photoexcited electrons from CB_3 and CB_2 to CB_1, and photoexcited holes from VB_2 to VB_1 will then occur on a picosecond time-scale. The magnitude of PB_2 will therefore be reduced since bleaching will arise solely from the filling of CB_1 and depletion of VB_1. Consequently thermalisation is expected to strengthen PB_1 relative to PB_2. Our calculations show that significant contributions to PB_2 from VB_1 to CB_2 and CB_3 transitions are important in addition to the VB_2 to CB_1 transition that has been hypothesised previously to explain the interpretation of experimental TAS spectra [145].

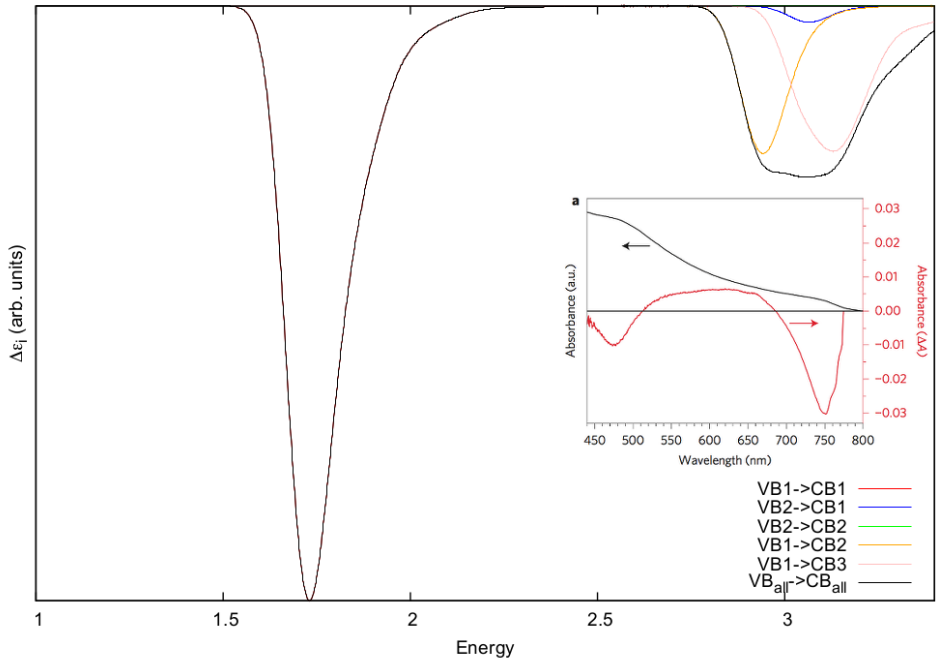

Figure 4.20: Simulated transient absorption spectroscopy for MAPI, the excitation population is 10^{-5} carriers per unit cell. The transitions are shown in figure 4.19. The inset represents experimental measurements performed by Manser *et al* [145].

The photoinduced absorption measured in MAPI between the main photo-bleaches is not reproduced by our approach. This effect might therefore be due to (i) relaxation of the structure after excitation of a charge carrier to the CB, for example local reorientation of methylammonium cation to screen the charge that was transferred from I to Pb orbitals and/or (ii) the Stark effect. The carrier relaxation dynamics are important in semiconductors as a guide to understanding defect mediated recombination and the change in absoprtion/emission rates under working conditions for solar cells and lasers.

Chapter 5

Radiative Recombination Rates

5.1 Introduction

The minority carrier lifetime, which is how long an electron-hole pairs can exist before recombining through radiative or non-radiative routes, plays a key role in photovoltaic devices. Recombination is very important for power conversion efficiency as the electron-hole pair must remain separated long enough to be collected by their respective contacts. A number of factors determine the nature and rate of the recombination process, including intrinsic effects such as the nature of the band structure (e.g. whether the gap is direct or indirect) and extrinsic factors which gives rise to defects.

Lead based hybrid Perovskites exhibit strong light absorption, a characteristic of direct gap semiconductors, while possessing the slow radiative recombination characteristic of an indirect gap semiconductor. Through time-resolved photoluminescent (TRPL) spectroscopy and other methods, minority carrier recombination lifetimes of microseconds have been observed in MAPI [70, 147–150], comparable to lifetimes measured in high-quality samples of crystalline silicon, the archetypal indirect gap semiconductor [151, 152]. The minority carrier diffusion lengths considerably exceeds the material thickness required for complete solar capture, while the reported carrier mobilities are orders of magnitude lower than conventional inorganic semiconductors. Therefore, internal quantum efficiencies (IQE) approach 100% [59, 60, 153, 154].

A variety of trap-based models have been used to interpret the TRPL data which show

extremely low recombination rates [148, 155, 156]. These models assume that the long lifetimes are due to immobilisation of charges in trap-states. However, samples (both single- and poly-crystalline) with trap density differences of five orders of magnitude have lifetime variations of only one order of magnitude [70, 148]. This suggests that lifetime is weakly correlated with measured trap density. Furthermore, longer lifetimes are observed in low trap-density monocrystalline samples.

This chapter introduces recombination routes and rates, discusses experimental findings for carrier lifetimes in hybrid Perovskites, and develops an *ab initio* computational approach to calculate carrier lifetimes. Finally the origins of such long carrier lifetimes are discussed.

5.2 Recombination Processes

In an atomic system in vacuum, the rate of excitation of an electron from the ground state to an excited state, due to coupling to a photon field, is equal to the reverse of this process. In bulk materials this process is made more complicated due to the introduction of the crystal momentum vector ($\vec{k}$) as a quantum number, and defect meditated non-radiative recombination.

Carrier recombination in semiconductors can occur through radiative processes where a photon is emitted, or through non-radiative routes where the excited carriers can relax through mid band gap states. In the latter process, the excess energy is released in the form of lattice vibrations. An ideal semiconductor for photovoltaic applications has long carrier diffusion lengths and zero non-radiative recombination, as discussed previously [13, 14].

Non-Radiative Recombination

Due to the interactions of a bulk material with ambient environment or introduction of impurities during the fabrication process, defects may be created. In semiconductors, these impurities may create new energy levels within the band gap. These localised states act as carrier recombination centres and can be detrimental to photovoltaic materials. Such states provide a route for non-radiative recombination, where an excited electron within the conduction band thermalises to the valence band, transferring energy to the lattice structure (phonon population).

Non-radiative recombination also known as Shockley-Read-Hall (SRH) process [157, 158], is extremely important for indirect band semiconductors which tend to have long radiative

lifetimes. In direct band semiconductors which tend to have much shorter radiative lifetimes, the SRH process becomes important for low excited carrier densities.

Radiative Recombination

The reverse process to photoexcitation in bulk materials is radiative recombination. Also known as spontaneous emission, this process is a result of an electron-hole pair recombining to release a photon. A schematic diagram of this process is shown in figure 5.1. Radiative recombination is constrained by the conservation of energy and momentum (the energy of the emitted photon is equal to the energy difference of the electron-hole pair). This process may be due to direct or indirect optical transitions, the latter being important where the phonon population is significant.

Similar to photoexcitation, the indirect radiative recombination rate is slower than the direct recombination rate; thus indirect band gap semiconductors such as silicon and germanium have slower radiative recombination rates than direct band semiconductors like GaAs and CdTe [151, 152,159–164]. For extremely high excited carrier populations, stimulated emission is important; however for carrier densities in solar cells under operation conditions this process can be ignored.

Total Rate of Radiative Recombination

The transition rate in a two-state system is given by Einstein's A coefficient

$$A_{cv}(\omega_{cv}) = \frac{n_r e^2 \omega_{cv}}{\pi \epsilon_0 \hbar c^3 m^2} |P_{cv}|^2 \delta(E_c - E_v - \hbar\omega_{cv}) \tag{5.1}$$

Here ω_{cv} is the energy difference between the two states[1], P_{cv} is the matrix element between two states, measuring the coupling of the two states and the electromagnetic field [165, 166]. n_r is the index of refraction, which is unity in vacuum; in solids usually n_r>1. The relation between the index of refraction and the complex dielectric function is given by equations 3.56 and 3.57.

[1] labels chosen in anticipation for recombination rate in bulk, where subscripts c and v will represent conduction and valence bands.

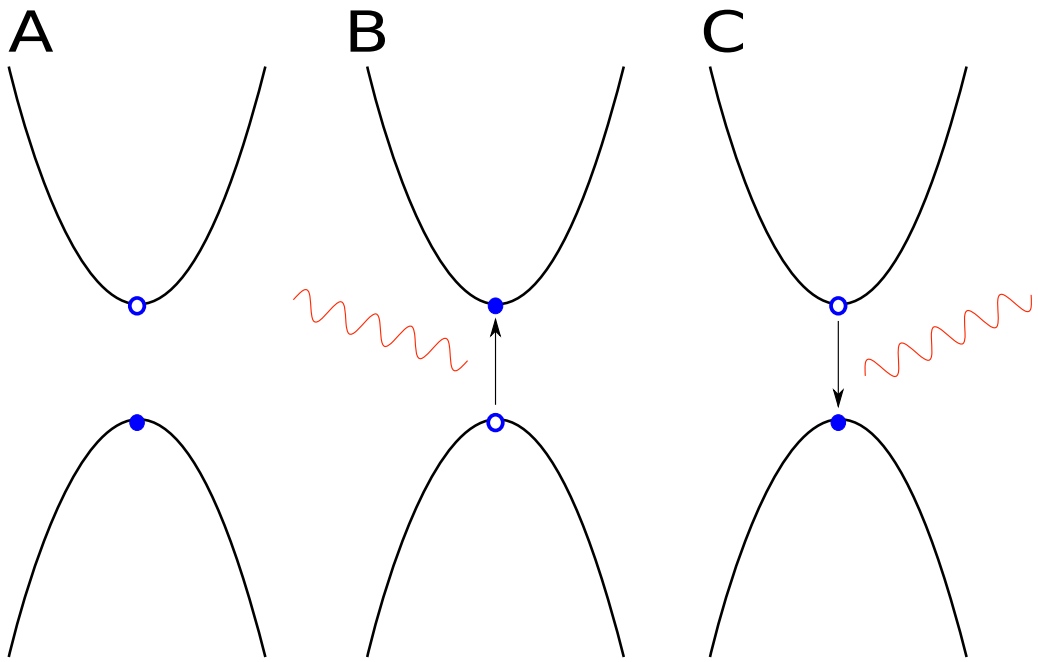

Figure 5.1: Schematic diagram showing the process of photoexcitations and radiative recombination. At ground state, electrons and holes occupy the valence and the conduction bands respectively (figure A); through absorbing a photon of energy equal or greater than that of the band gap an electron is promoted to the conduction band and a hole is promoted to the valence band (figure B). After a period of time the generated electron-hole pair recombine and release a photon of the band gap energy (figure C).

The matrix element in equation 5.1 is identical to that of equation 3.51 describing the imaginary part of the dielectric function; hence the total rate of recombination and the imaginary part of the dielectric function can be related through

$$\epsilon_i(\omega_{cv})\frac{\omega_{cv}^3 n_r}{4\pi\epsilon_0\pi^2 c^3\hbar} = \sum_k A_{cv}\,\delta[E_v(k) - E_c(k) - \hbar\omega_{cv}] \tag{5.2}$$

where each $\vec{k}$-point has been modelled as an individual two state system for each pair of conduction and valence bands. However, it must be scaled by Fermi functions for the electrons and

holes to satisfy the Pauli principle. Therefore, equations 5.1 and 5.2 are rewritten as[2]

$$A^*_{cv}(\omega_{cv}) = \frac{n_r e^2 \omega_{cv}}{\pi \epsilon_0 \hbar c^3 m^2} |P_{cv}|^2 \delta(E_c - E_v - \hbar\omega_{cv}) f_c(E_c, E^f_c)(1 - f_v(E_v, E^f_v)) \quad (5.3)$$

$$\epsilon^*_i(\omega) = (\frac{2\pi e}{m\omega_{cv}})^2 \sum_{\vec{k}} |P_{cv}|^2 \delta(E_c - E_v - \hbar\omega_{cv}) f_c(E_c, E^f_c)(1 - f_v(E_v, E^f_v)) \quad (5.4)$$

where $f_c(E_c, E^f_c)$ is the Fermi function for an electron with energy E_c in a system with quasi-Fermi level E^f_c. Fermi functions give the probability of an electron occupying an energy level E_c in the system. The expression $(1 - f_v(E_v, E^f_v)$ gives the probability that an electron is not occupying a state with energy E_v and quasi-Fermi level E^f_v (i.e. the probability that a hole is occupying a give state). The second term is due to the Pauli Exclusion Principle. From these new expressions a relation between the imaginary part of the dielectric function and the total transition for a given energy is derived to be[3]:

$$\epsilon^*_i(\omega_{cv}) \frac{\omega^3_{cv} n_r}{4\pi\epsilon_0 \pi^2 c^3 \hbar} = \sum_k A^*_{cv}\, \delta[E_v(k) - E_c(k) - \hbar\omega_{cv}] \quad (5.5)$$

Integration of equation 5.5 gives

$$R^{Tot}_{cv} = \frac{n_r}{4\pi^3 c^3 \hbar^4 \epsilon_0} \int_{E_g}^{\infty} dE \epsilon^*_i(E_{cv}) E^3_{cv} = \int_{E_g}^{\infty} dE \sum_k A^*_{cv} \delta[E_v(k) - E_c(k) - \hbar\omega_{cv}] \quad (5.6)$$

which is the total rate of transition over all energies per unit volume for all allowed direct transitions, where E_g is the band gap of the system. R^{Tot}_{cv} is the total rate of recombination and has units $\mathrm{cm}^{-3}\mathrm{s}^{-1}$ as it is conventionally written in units cgs, i.e.

$$R^{Tot}_{cv} = \frac{n_r}{\pi^2 c^3 \hbar^4} \int_{E_g}^{\infty} dE \epsilon^*_i(E_{cv}) E^3_{cv} = \int_{E_g}^{\infty} dE \sum_k A^*_{cv} \delta[E_v(k) - E_c(k) - \hbar\omega_{cv}] \quad (5.7)$$

Quasi-Fermi Level

As discussed, electrons in a semiconductor may occupy a state within the conduction band above the band edge with a given probability. This probability is given by the Fermi-Dirac function and is a function of the energy of the state, temperature and quasi-Fermi level. The quasi-Fermi level of a carrier within a system is in turn determined by the temperature, carrier density and the density of states of the bands. The relation between the total number of carriers,

[2]Here the superscript * indicates the non-equilibrium form of the equation.

[3]here $f_c(E_c, E^f_c)$ and $(1 - f_v(E_v, E^f_v))$ have been abbreviated to $f_c(1 - f_v)$.

temperature and DOS is given by:

$$n = \int g(E) f(E, E^f, k_B T) dE \tag{5.8}$$

where $g(E)$ is the DOS of the band structure, n is the total number of carriers and $f(E, E^f, k_B T)$ is a Fermi-Dirac function with quasi-Fermi level E^f for a state with energy E. The limits of the integration are dependent of the carrier of interest [13].

Equation 5.8 can be used to obtain the quasi-Fermi level for a given temperature and carrier population for a system of interest.

Minority Carrier Lifetime

The recombination dynamics of carriers within the bulk of an intrinsic semiconductor ($n = p$, where n and p are the excited electron and hole population density[4]) can often be accurately described by a third-order rate equation:

$$\frac{dn}{dt} = G - nA - n^2 B - n^3 C \tag{5.9}$$

Here n is the density of excited carriers and G is a source term describing photogeneration of carriers [167]. These parameters are often fit to experimental transient data across a large range of laser fluences and thus carrier densities [168]. An implicit assumption is that these coefficients do not vary across the carrier density regimes that are experimentally accessed. In the expression above A is related to the one-body non-radiative carrier recombination, which proceeds through crystal defect levels as intermediate states. The two-body coefficient B describes radiative recombination of free carriers and is closely connected with both absorption and emission. C is the three-body Auger recombination coefficient and becomes important under large excited carrier populations and high temperatures.

As the aim of this work is to investigate intrinsic effects on recombination, extrinsic effects such as defect mediated recombination are ignored; hence $A = 0$. Additionally the Auger recombination process occurs under conditions where the excited carrier densities are much larger than those encountered during PV solar cell operation and for higher temperatures, hence such process can also be ignored and $C = 0$. The remaining route of recombination is

[4] more details provided in appendix A

bi-molecular and gives the following decay equation:

$$\frac{dn}{dt} = G - n^2 B \tag{5.10}$$

by switching off the generation source (i.e. $G = 0$), the total rate of emission is the total rate of radiative recombination. The expression above can be related to equation 5.7, giving:

$$R_{cv}^{Tot} = n^2 B \tag{5.11}$$

The minority carrier lifetimes are conventionally expressed in terms of

$$\tau^{-1} = Bn = R_{cv}^{Tot}/n \tag{5.12}$$

where τ is the minority carriers' lifetime for a give excited carrier density and temperature.

5.3 Recombination Model in Lead Based Hybrid Perovskites

Figure 4.4 shows a schematic diagram of MAPI's (this diagram is also valid for other lead base hybrid Perovskites) band structure around the high symmetry R point (in the pseudo-cubic phase, Γ in the tetragonal structure); This schematic highlights the spin split nature of the band structure due to the Rashba splitting as discussed in chapters 3 and 4.

The joint density-of-states (JDOS) of MAPI, relevant for absorption, differs from that of a direct band semiconductor in a small energy range around E_g (shown in figure 4.13). The flattened valence band contributes to a large density of states available for optical transition at the fundamental gap. Thus absorption is only slightly affected by spin-splitting, that is MAPI absorbs visible light as though it was a direct band gap semiconductor. However, radiative recombination is dramatically suppressed. This is extremely unusual for a solar cell material where typically emission and absorption are the direct reverse of one another.

In MAPI photoexcited electrons (holes) rapidly thermalise to a small region of $\vec{k}$ space centred at the conduction (valence) band edges. The asymmetry in $\vec{k}_{min}^{CBM}$ and $\vec{k}_{max}^{VBM}$ means that there is a low JDOS of the thermalised minority carriers. Direct ($\vec{k}$ conserving) recombination is therefore reduced. This mismatch of carriers' momenta in hybrid Perovskites forbids a direct recombination of the carriers due to the law of conservation of momentum hence reducing the rate of radiative recombination.

Furthermore the nature of the band edge spin texture in hybrid Perovskites is a topic of discussion important for radiative recombination. It has been suggested that for MAPI structures where the iodine and lead are shifted from their ideal positions, the helicity of the spin texture for the VBM and CBM can be switched between parallel and anitparallel, these two cases are shown in figures 5.2A and 5.2B respectively [169–172]. This feature of opposite spin helicity has been experimentally observed in BiTeI which demonstrates similar Rashba characteristics to lead halide Perovskites [173]. The existence of antiparallel spin textures at the band edge will reduce the rate of bi-molecular radiative recombination. This is because to adhere to the spin selection rule, carriers must occupy states further away from their respective quasi-Fermi levels. In a perfectly periodic material only one spin alignment phase can exists, however for structures such as MAPI which are periodic only on a local scale both phases can coexists within a large sample.

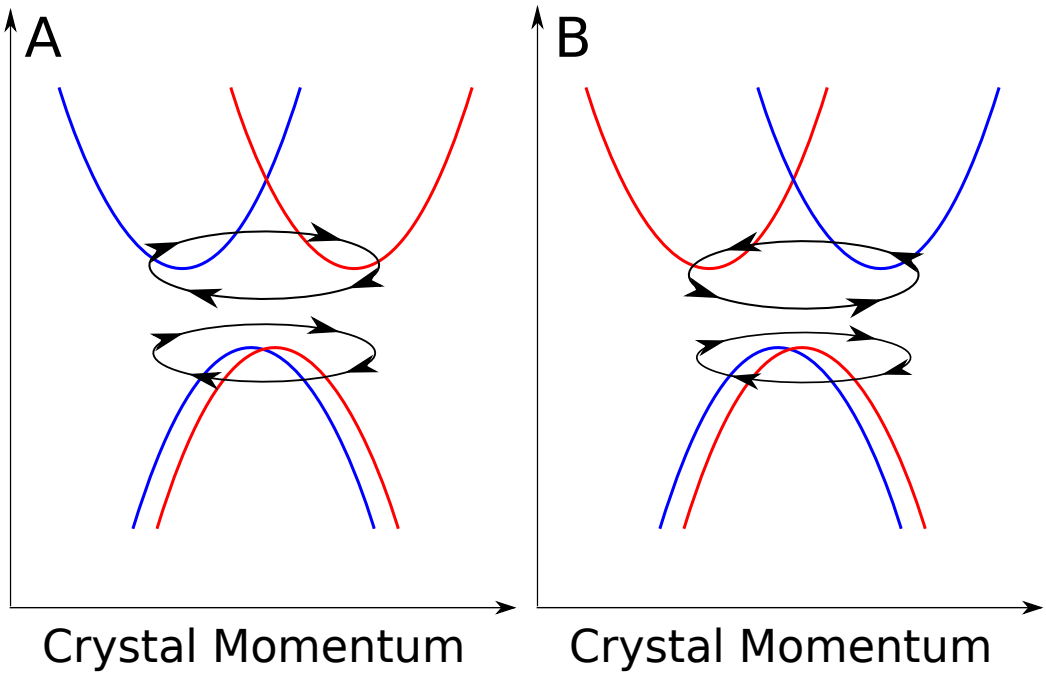

Figure 5.2: Schematic diagram showing parallel (A) and antiparallel (B) spin textures for the conduction and valence bands, where red and blue represent spin up and down respectively.

To investigate the effect of spin helicity on the radiative recombination in MAPI, the two configurations are artificially enforced during the calculations. It should be noted that the QSGW calculation performed on $\text{MAPI}_{\langle 100\rangle}$ resulted in parallel spin helicity. However as mentioned, the literature indicates that this is due to the pseudo-cubic nature of the structure used which did not include distortions of the inorganic polyhedron cages.

5.4 Results and Discussion

B, computed as a function of carrier density for MAPI(parallel spin helicity $\text{MAPI}^{P}_{<100>}$ and antiparallel spin helicity $\text{MAPI}^{A}_{<100>}$), CdTe, and GaAs at several temperatures are shown in figure 5.3.

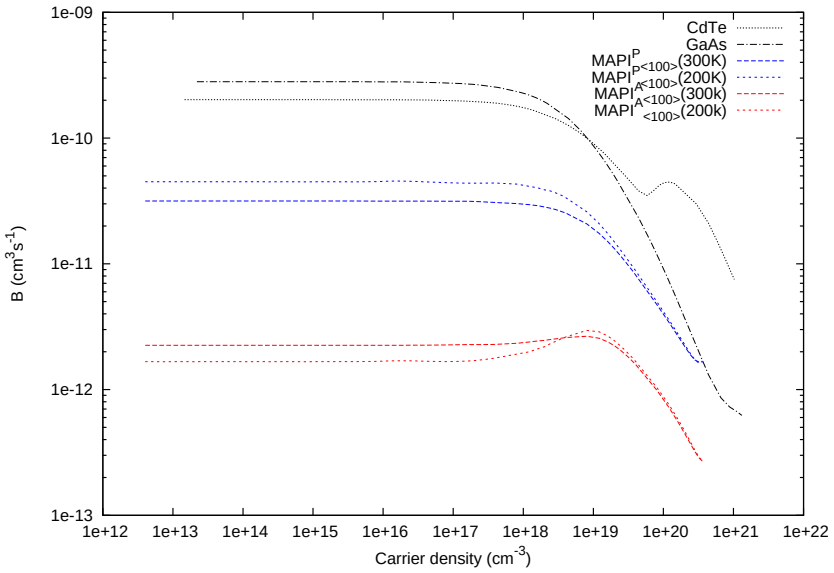

Figure 5.3: Calculated radiative recombination coefficients for CdTe, GaAs, $\text{MAPI}^{A}_{<100>}$ and $\text{MAPI}^{P}_{<100>}$. The Perovskite calculations where for 200K and 300K to demonstrate the different trends for the two configurations.

Experimental values at room temperature are displayed in table 5.1. These measurements vary widely, presumably owing to the competition of B with other, non-radiative, recombination paths. The presence of these pathways will depend strongly on how the material is fabricated, and so the smallest measured B value is probably the most reliable, and the most directly comparable to our calculations. We calculate B to be $\sim$ 100 times smaller in $MAPI^{A}_{<100>}$ and $\sim$ 10 times smaller in $MAPI^{P}_{<100>}$ than the direct gap semiconductors CdTe and GaAs, but larger than the fully indirect Si. This finding is directly due to the presence of SOC as calculations without SOC result in comparable values to that of CdTe and GaAs [129]. MAPI resembles an indirect gap semiconductor for radiative carrier recombination, and a direct gap semiconductor for absorption.

Compound	Experimental(10^{-12}cm^{3}s^{-1})	QSGW factor
$MAPI^{P}_{<100>}$	See text	27.2
$MAPI^{A}_{<100>}$	See text	1.93
CdTe [162–164]	100-5100	195
GaAs [159–161, 163]	130-1300	267
Si [151, 152]	0.001-0.01	

Table 5.1: Experimental and QSGW values for B at room temperature with $n = 10^{17}$cm^{-3}. As the absorption and recombination processes in silicon are extremely dependent on phonon contributions the calculation of radiative recombination coefficient for silicon is omitted here.

The magnitude of B increases as the $\vec{k}$-space overlap between electron and hole distribution functions increases. This causes the rate of bi-molecular recombination in $MAPI^{A}_{<100>}$ to depend on external parameters in an unusual manner. For example, increasing temperature smears f_c and f_v over a wider band of $\vec{k}$ for fixed photoexcited carrier densities, causing B to increase with T. The temperature dependence of B in GaAs and CdTe (Fig. 5.4) is weaker and of opposite sign to $MAPI^{A}_{<100>}$. Further, in $MAPI^{A}_{<100>}$ bi-molecular recombination will increase with photoexcited carrier density once the electron pockets begin to fill up and overlap (n $\approx 10^{18}$

cm^{-3} in Fig. 5.3), in sharp contrast to CdTe and GaAs. Only at high carrier concentrations when a significant fraction of electrons and holes overlap does B in MAPI become comparable to B in CdTe, where it also adopts the conventional behaviour and begins to decrease with increasing carrier densities. The potential existence of both spin texture phases along with strong carrier density and therefore laser-fluency, global fits to time resolved data may not be reliable method to infer B or lifetime (Equation 5.12). The variation of B with carrier density will make high fluency transients multi-exponential and break the expected relationship between light-emission and carrier-density sensitive experimental probes.

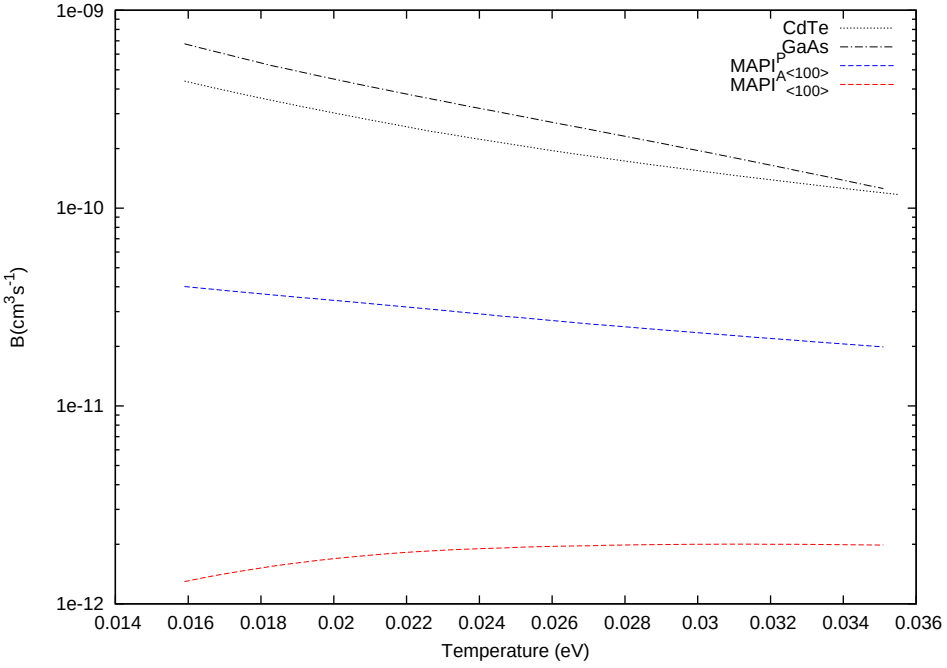

Figure 5.4: Temperature dependent B coefficient calculated for CdTe, GaAs, $MAPI^{A}_{<100>}$ and $MAPI^{P}_{<100>}$. $MAPI^{A}_{<100>}$ shows the opposite trend with increasing temperature compared to the other three set of data.

For photoexcitation densities n $< 10^{17}$ cm^{-3} ($n = p$), we find $B = 1.93 \times 10^{-12}$ cm$^3 s^{-1}$ for MAPI$^A_{<100>}$ and $B = 2.72 \times 10^{-11}$ for MAPI$^P_{<100>}$ at room temperature. These are the charge carrier densities relevant for device operation in sunlight. As B is fairly constant below this charge carrier density, we can use Equation 5.12 to derive a lifetime of order 0.1-10 μs. This lifetime is consistent with values reported in the literature for single crystal samples under 1 and 0.1 sun intensity [69, 147, 148].

There are limited temperature dependent TRPL data available. Most data are for polycrystalline films, whereas our results would be best compared to single crystal measurements. Yet it has been observed that the carrier lifetime is highly temperature sensitive at low fluence while being temperature insensitive at high fluence [148]. The increase in minority carrier lifetime with decreasing sample temperature can be directly explained by a contraction of the Fermi-Dirac distribution near the spin-split band minima.

In this work so far only MAPI in an idealised static structure has been considered. In reality, the high temperature phase of MAPI is cubic on average only; the dipolar molecules between cages continually rotate, the cages flex and tilt. Second-order Jahn-Teller deformations of the octahedral due to the Pb 6s lone pair directly distort the lead iodide bonds, generating local electric fields near the atomic core region where spin-orbit coupling is high. Recent molecular-dynamics simulations by Etienne *et al.* suggest that the conduction band splitting persists in the presence of disorder [174].

If the material has true inversion symmetry, as MAPI is believed to in the orthorhombic phase below 162 K, no directional electric fields can exist, and so the spin-split indirect-gap should vanish. In such case the radiative carrier recombination lifetimes are expected to be significantly smaller than those found in MAPI$^A_{<100>}$.

To assess the effect of dynamic disorder, *ab initio* molecular dynamics at 300 K with $2\times2\times2$ supercells were performed by Frost *et al.*. Such supercells are able to accurately describe the phonon modes both at the Γ point and the Brillouin zone boundary; these k-points contain the important low-energy vibrational modes responsible for disorder. 100 realisations were extracted, each temporally separated by 2.5 ps, collected after an initial equilibration period. The $\vec{k}$-space splitting of these 100 structures were calculated by Scott McKechnie. Given the increased computational cost of this larger structure (96 versus 12 atoms), the electronic properties were calculated within the local density approximation (LDA) including spin-orbit coupling. It

was found that between molecular dynamics snapshots, the spin-split band extrema and effective masses fluctuate. This may explain the observed reduction in mobility as a function of temperature, in the temperature regime where the organic moieties are increasingly disordered. The average band minima spin-split from the high symmetry point decreases slightly from 0.043Å^{-1} for pseudo-cubic $\text{MAPI}_{<100>}$ to 0.03Å^{-1}. This suggest that although $\text{MAPI}_{<100>}$ has an exaggerated splitting compared to MD structures which are more representative of the bulk material, the recombination rates should be comparable.

Chapter 6

Conclusions

6.1 Summary

In this dissertation the electronic and optical properties of organic-inorganic hybrid Perovskites were studied and compared with experimental data. A range of properties including band gaps, optical absorptions and minority carrier lifetimes were discussed within the context of photovoltaic applications. The research in this thesis aimed to find the origins and mechanisms behind the high power conversion efficiencies (PCE) obtained through hybrid Perovskite solar cells.

Ab initio calculations have shown that through variation of constituent ions within hybrid Perovskites a wide range of physical properties can be tuned. Quasi-particle self-consistent GW (QSGW) calculations showed that the band gap of lead halide hybrid Perovskites ($APbX_3$ where A=$[NH_3CH_3]$, $[CH(NH_2)_2]$ and X=Cl, Br, I) can be increased by including lighter halides at the X site. The same could be achieved by substitution of smaller molecules at the A site. This trend is attributed to the decrease in the metal-halide bond length in hybrid Perovskites with smaller organic molecules or lighter halide ions. The calculated band gaps for room temperature structures range from 1.63eV for $[CH(NH_2)_2]PbI_3$ (FAPI) to 3.44eV for $[NH_3CH_3]PbCl_3$ (MAPC). Only FAPI and MAPI are suitable for single-junction solar cells because of their smaller optical gaps, while MAPB and MAPC are more suitable for tandem architectures where semiconductors of various band gap energies are used to surpass the QS limit.

An interesting aspect of the band structures of lead based hybrid Perovskites is the influence of the spin-orbit coupling (SOC). Owing to the heavy nature of lead, SOC affects the band structure significantly. It narrows the band gap by as much as 1eV. In some early works based on local and semi-local density functionals, band gaps calculated without SOC were fortuitously close to the experimental values [1]. The good agreement between experimental data and these early calculations was due to the cancellation of errors from the underestimation of LDA and the overestimation caused by the lack of SOC. Additionally, relativistic effects in the form of the Rashba splitting perturb the valence and conduction band edges of the Perovskites which lack centrosymmetry. As the Rashba splitting parameters for the lowest conduction band (lead based) and highest valence band (iodine based) differ in magnitude, hybrid Perovskites possess indirect band gaps. The energy splitting of the conduction bands can ranges between 0-100meVs, this difference depends on the chemical composition and crystal structure.

Surprisingly, these solution processed Perovskites with their indirect optical band gaps have shown great absorption over visible spectrum, comparable to that of well established direct band gap semiconductors such as GaAs and CdTe. This is a great advantage for solar cell materials as it allows the use of thinner absorber layers without compromising on PCE. This potentially allows for a multi-junction all hybrid Perovskite solar cell which exhibits strong absorption across the solar spectrum.

The QSGW optical calculations performed on $MAPbX_3$ where X=Cl, Br or I were compared with experimental data and showed good agreement within the limits of the theory used. The comparison between the theoretical and experimental data showed an increase in excitonic effects with lighter halide ions. As the excitonic binding energy is extremely low in MAPI, excitonic effects are also minimal, resulting in a slight blue shift within the absorption spectrum. This effect is due to the random phase approximation used in QSGW approach and has been discussed, at length, by Louie and Rohlfing in ref. [139]. The increase in the excitonic nature with lighter halides is attributed to the reduced static polarisation of the ions. The sharp absorption edge of MAPI has previously been assigned as an excitonic excitation, however there is partial contribution from the perturbation of the band edge due to the Rashba interaction. More accurate theoretical data and perhaps better agreement with experimental data requires the inclusion of electron-hole contributions. It would be interesting to perform QSGW+BSE calculations on hybrid Perovskites, however due to the good agreement with experimental data

very little change is expected, specially for MAPI and FAPI. At the time of these calculations, an all electron GW implementation which included Bethe-Salpeter equation, did not exist [175]. Very recently Brian Cunningham has implemented the BSE in the Questaal package we use (informed through private communication), but we have not yet applied this level of theory to these systems.

One of the most fascinating aspects of hybrid Perovskites has been high internal quantum efficiency and the extremely long radiative-recombination lifetimes observed in a number of the halide Perovskites. These features are particularly unusual as hybrid Perovskite solar cells are often solution processed, which is a synthesis method that typically results in large defects density and poor PCEs. However, such defects seem to be absent in these cells. Additionally, the lifetimes are similar to those observed in high quality indirect band gap semiconductors. The radiative recombination rate of these materials was investigated through an *ab initio* method relating the imaginary part of the dielectric function to the total rate of radiative recombination which was derived and implemented as part of this thesis. In this thesis it is found that the spin-split nature of the conduction and valence bands results in the segregation of electrons and holes within reciprocal space. Research on a Perovskite and other structures with distorted ions, have shown that there can exist configurations of atomic displacements, where the Rashba parameters (α_R in equation 3.48) for the conduction and valence bands have opposite signs, that is conduction and valence bands of same spin are shifted in opposite directions. The lifetime calculations show that in such cases the radiative recombination rate in MAPI can be up to two orders of magnitude smaller than that of CdTe and GaAs. This finding is remarkable as it shows that such long carrier lifetimes are an intrinsic feature of lead based hybrid Perovskites.

The theoretical investigation of the electronic and optical properties of hybrid Perovskites performed here, indicate the fundamental characteristics of a material suitable for high PCE solar cells. These materials have shown strong absorption of the visible spectrum along with extremely long diffusion lengths due to the minority carrier lifetimes.

6.2 Future Directions

Intermediate band solar cells

The extremely long carrier lifetimes in lead based hybrid Perovskites may make it possible to create an intrinsic intermediate band solar cell (IBSC). This photovoltaic device architecture relies on a state within the band gap, which allows the two step excitation of electrons from the valence band to higher conduction bands (figure 6.1). The introduction of an intermediate band is aimed to surpass the Shockley-Queisser limit (discussed in chapter 3); in fact Luque and Marti calculated that such cells can achieve efficiencies as high as 63.1% [176]. IBSC can be created through a number of methods including quantum dots (QD) and the intentional inclusion of mid gap defects [177, 178]. One of the issues with IBSC devices is the increase in the rates of radiative and non-radiative recombination due to the introduction of the mid gap states [179].

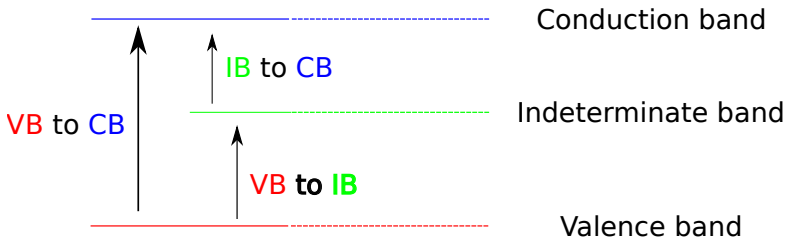

Figure 6.1: Schematic diagram of energy states in an IBSC. In an IBSC electrons are initially promoted from the valence band (VB) to an intermediate band (IB) and the to the conduction band (CB) [180].

The idea behind lead based hybrid Perovskite IBSC would be to utilise the lowest conduction band as the intermediate band, while collecting excited electrons from the second set of conduction bands (as shown in figure 6.2) [181]. In this configuration the slow rate of recombination would allow a build up of electrons in the lowest conduction bands which can then be promoted to the second set of conduction bands. Although the energy differences between the three bands in MAPI are not ideal for maximum efficiency, it can be used as a test case for proof of concept; furthermore higher efficiencies maybe achievable through other hybrid Perovskites.

Preliminary calculations performed by Scott McKechnie have shown that the VBM and CBM are not only at different positions in reciprocal space, but the second lowest conduction band minima occupy different positions to both VBM and CBM as well (as shown inf figure 6.2). This characteristic may form an intrinsic photon ratchet which will reduce the recombination from IB to the VB and from the CB to the IB and the VB.

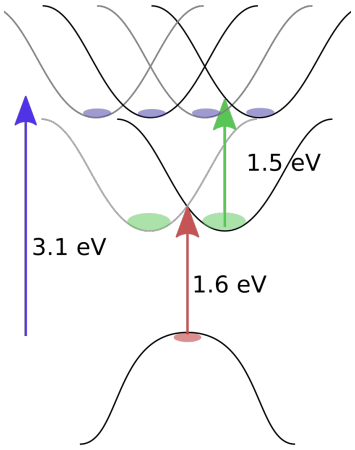

Figure 6.2: The band structure of MAPI for IBSC. Here the lowest conduction band would act as an intrinsic intermediate band.

One aspect of continuation of the research provided in this thesis is to investigate the properties of MAPI for IBSC architecture. This involves the calculation of absorption and recombination rates from IB to the CB and VB to CB.

V-VI-VII Semiconductors

Lead based hybrid Perovskites solar cells can be produced using cheap solution processing methods, additionally all the constituents elements are earth abundant. Such features combined with high recorded PCE should makes these cells highly desirable. However, lead based hybrid Perovskites have two major drawbacks which have significantly slowed their commercial realisation, these drawbacks are: the instability of these compounds under working conditions and within ambient atmosphere and the inclusion of lead, which is a toxic heavy metal. Due to these reasons there is currently active ongoing research to increase the stability of these compounds

through passivation and encapsulation. However, the device lifetimes of high performing cells are still significantly below that of established photovoltaic technologies such as Si and GaAs. There have also been many attempts at removing lead, however such devices are yet to achieve efficiencies comparable to those of lead based Perovskites, furthermore the existence of Sn^{2+} oxidation state which lowers the stability of devices remains a challenge. The higher PCE is perhaps due to the long carrier lifetimes in lead based hybrid Perovskites which are due to the presence of lead (a heavy element), an internal electric field and the lack of centrosymmetry. As the origin of the long lifetimes maybe due to the Rashba splitting, it should be substituted by comparably heavy elements.

As a result of the disadvantages mentioned, it is possible that Perovskite photovoltaic solar cells may not be able to challenge established PV cells such as silicon. However, lead based hybrid Perovskites may have introduced an entirely new direction of material research for photovoltaic cells, namely the search for compounds with non-toxic heavy elements that have large lattice-induced polarisation fields and are susceptible to breaking inversion symmetry, or alternatively, materials which have an indirect fundamental gap slightly lower in energy than the direct optical gap. Such features can mimic the Rashba splitting in MAPI which may give it its extraordinary lifetimes. To this end, Butler *et al.* have investigated a group of V-VI-VII semiconductors, which appear to have similar properties as lead based hybrid Perovskites. Initial band structure calculations have shown that BiSI and BiSeI have indirect band gaps a few k_BT lower than the direct optical band gaps, similar to that of MAPI [182, 183]. A number of non-Bismuth based members of this family have also been investigated recently, possessing larger band gaps more suitable for tandem cells [184].

As a further future direction to continue the work of this thesis, the radiative recombination rates in V-VI-VII will be investigated. The radiative recombination rate will be calculated for compounds with the most promising features. These include the band gap and its nature, that is if the direct-indirect nature is present. Additionally the effective masses and absorption coefficients will be taken into account. Much like hybrid Perovskites V-VI-VII semiconductors' properties can be tuned through variation of the constituent ions and potentially a wide range of compounds can be investigated. The aim of this approach would be to find more stable compounds which do not include toxic elements and share opto-electronic properties similar to those of MAPI or desirable for PV applications.

Appendix A

Carrier Recombination Dynamic

To obtain the radiative recombination coefficient or lifetime the following parameters are used

$$n = n_0 + \Delta n \tag{A.1}$$

$$p = p_0 + \Delta p \tag{A.2}$$

$$R(B,n,p) = Bnp = B(n_0 + \Delta n)(p_0 + \Delta p) \tag{A.3}$$

where n and p are the total electron and hole density with n_0 and p_0 being the background doping density and Δn and Δp are the photo-generated carrier densities. $R(B,n,p)$ and B are the radiative recombination rate and coefficient respectively. and the rate equation for the carrier densities is given by

$$\frac{\partial \Delta n(t)}{\partial t} = -R(B,n,p) \tag{A.4}$$

High Doping, Low Injection

In the case of high hole doping the total radiative recombination rate s given by

$$R(B,n,p) = Bnp = B\Delta n(p_0 + \Delta p) \tag{A.5}$$

and hence

$$\frac{\partial \Delta n(t)}{\partial t} = -R(B,n,p) = B\Delta n P_0 + B\Delta n \Delta p \tag{A.6}$$

and for low injection rate

$$\frac{\partial \Delta n(t)}{\partial t} = -R(B,n,p) = B\Delta n P_0 \tag{A.7}$$

as $P_o >> \Delta p$, giving the time dependent photogenrated density as

$$\Delta n(t) = \Delta n(0) \exp(-\frac{t}{\tau}) \tag{A.8}$$

with $\tau = \frac{1}{BP_0}$.

Low Doping, High Injection

In the case of a material under high excitation fluencies and low hole doping the total recombination rate is given as

$$R(B, n, p) = Bnp = B\Delta n(p_0 + \Delta p) \tag{A.9}$$

and hence

$$\frac{\partial \Delta n(t)}{\partial t} = -R(B, n, p) = B\Delta n\Delta p \tag{A.10}$$

as $\Delta p >> P_o$, this is appropriate for materials with extremely low doping and intrinsic materials (no doping). In such case the time dependent carrier density is given as

$$\Delta n(t) = \Delta n(0) \exp(-\frac{t}{\tau}) \tag{A.11}$$

with the carrier lifetime being $\tau = \frac{1}{B\delta p}$.

Appendix B

Non-local Contribution to Optical Matrix Elements

The dipole matrix element can be calculated through

$$P_{i,f} = \lim_{q\to 0} \frac{1}{q} \langle c, \mathbf{k}+\mathbf{q}| \, e^{i\mathbf{q}\cdot\mathbf{r}} \, |v, \mathbf{k}\rangle \tag{B.1}$$

in this form the $\lim_{q\to 0}$ must be taken numerically which is not desirable. Through the relation of the length operator and the velocity operator, the expression above can be rewritten within the momentum gauge as

$$P_{i,f} = \frac{1}{m_e \omega} \langle c, \mathbf{k}| \, \hat{\mathbf{e}} \cdot \mathbf{p} \, |v, \mathbf{k}\rangle \tag{B.2}$$

as discussed previously. However them momentum gauge has is only valid for local potentials, as the momentum operator does not include the non-local contributions to the velocity

$$\mathbf{v} = \frac{\mathbf{p}}{m} + \frac{i}{\hbar}[V^{NL}(\mathbf{r}, \mathbf{r}'), \mathbf{r}] \tag{B.3}$$

it is however possible to approximate the non-local contribution, if an assumption can be made that the density calculated from non-local potentials (hybrid functionals, GW , etc.) is similar to that calculated with a local potential (LDA). If such assumption holds we can simply write

$$\lim_{q\to 0} \frac{1}{q} \langle \psi^*{}_c, \vec{k}+\vec{q}| \exp(i\vec{q}\cdot\vec{r}) \, |\psi^*_{v,\vec{k}}\rangle = \lim_{q\to 0} \frac{1}{q} \langle \psi^*_c \, |\psi^0_c\rangle \, \langle \psi^0_v| \, |\psi^*_v\rangle \, \langle \psi^0_{c\cdot\vec{k}+\vec{q}}| \exp(i\vec{q}\cdot\vec{r}) \, |\psi^0_{v,\vec{k}}\rangle| \tag{B.4}$$

where * superscripts indicate non-local eigenfunctions and eigenvalues while 0 superscripts represent local counterparts. In the right hand side of the expression above the dipole moment is calculated for local eigenfunctions only and as such the expression can be rewritten in the momentum gauge

$$\lim_{q\to 0}\frac{1}{q}\left\langle\psi_c^*\right|\left.\psi_c^0\right\rangle\left\langle\psi_v^0\right|\left.\psi_v^*\right\rangle\left\langle\psi^0_{c,\vec{k}+\vec{q}}\right|\exp(i\vec{q}\cdot\vec{r})\left|\psi^0_{v,\vec{k}}\right\rangle| = \frac{1}{m}\left\langle\psi_c^*\right|\left.\psi_c^0\right\rangle\left\langle\psi_v^*\right|\left.\psi_v^0\right\rangle\frac{\left\langle\psi_c^0\right|\hat{e}\cdot\vec{p}\left|\psi_v^0\right\rangle}{E_c^0-E_v^0} \quad \text{(B.5)}$$

this equation can simply be written as

$$\begin{aligned}\frac{1}{m}\left\langle\psi_c^*\right|\left.\psi_c^0\right\rangle\left\langle\psi_v^*\right|\left.\psi_v^0\right\rangle\frac{\left\langle\psi_c^0\right|\hat{e}\cdot\vec{p}\left|\psi_v^0\right\rangle}{E_c^0-E_v^0} &= \frac{1}{m}\left\langle\psi_c^*\right|\left.\psi_c^0\right\rangle\left\langle\psi_v^*\right|\left.\psi_v^0\right\rangle\frac{\left\langle\psi_c^0\right|\hat{e}\cdot\vec{p}\left|\psi_v^0\right\rangle}{E_c^*-E_v^*}\frac{E_c^*-E_v^*}{E_c^0-E_v^0}\\ &= \frac{1}{m}\left\langle\psi_c^*\right|\left.\psi_c^0\right\rangle\left\langle\psi_v^*\right|\left.\psi_v^0\right\rangle\frac{\left\langle\psi_c^0\right|\hat{e}\cdot\vec{p}\left|\psi_v^0\right\rangle}{E_c^*-E_v^*}S^* = |P_{cv}^*|\end{aligned}$$

where $|P_{cv}^*|$ is a new effective dipole matrix. In the case where the densities of the local and non-local systems are identical, this approximation becomes exact. As the the two densities deviate, the error will become greater.

Appendix C

Brillouin Zone Labelling

The band structures plotted in this thesis follow the guide lines provided by ref [127]. Here Latin letters are assigned to points on the surface of the Brillouin Zone while Greek letters are assigned to points within the Brillouin Zone.

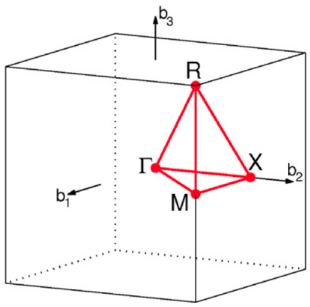

Figure C.1: Brillouin zone labelling for the pseudo-cubic band structures [127].

The labelling of the point for the pseudo-cubic case are shown in figure C.1, the tetragonal and orthorhombic labelling are shown in figure C.2.

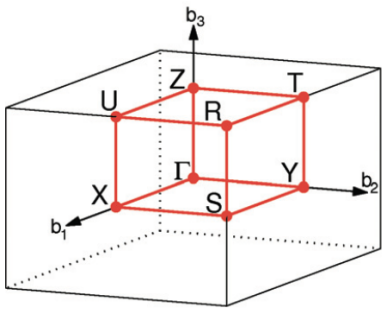

Figure C.2: Brillouin zone labelling for tetragonal/orthorhombic [127].

The method of calculation for each point within the Brillouin zone is outlined in reference [127]. These guide lines are used to adopt the convention used by the wider community.

Bibliography

[1] A. M. A. Leguy, P. Azarhoosh, M. I. Alonso, M. Campoy-Quiles, O. J. Weber, J. Yao, D. Bryant, M. T. Weller, J. Nelson, A. Walsh, M. van Schilfgaarde, and P. R. F. Barnes, "Experimental and theoretical optical properties of methylammonium lead halide perovskites," *Nanoscale*, vol. 8, pp. 6317–6327, 2016.

[2] BP, *Statistical Review of World Energy*. London: BP, 2016.

[3] REN21, *Renewables 2016 Global Status Report*. Paris: REN21 Secretariat, 2016.

[4] D. M. Le Floch, B. Bereiter, T. Blunier, J. M. Barnola, U. Siegenthaler, D. Raynaud, J. Jouzel, H. Fischer, K. Kawamura, and T. Stocker, "Dome c 800,000-year record." European Project for Ice Coring in Antarctica (EPICA), 2012.

[5] IPCC, *Climate Change 2013: The Physical Science Basis. Contribution of Working Group I to the Fifth Assessment Report of the Intergovernmental Panel on Climate Change*. Cambridge, United Kingdom and New York, NY, USA: Cambridge University Press, 2013.

[6] IEA-PVS Reporting Countries, Becquerel Institute (BE), RTS Corporation (JP), "2016 snapshot of global photovoltaic markets," tech. rep., International Energy Agency, 2016.

[7] National Renewable Energy Laboratory, "Research cell record efficiency chart,`https://www.nrel.gov/pv/assets/images/efficiency-chart.png`," 2017. [Online; accessed 9-July-2017].

[8] A. Kojima, K. Teshima, Y. Shirai, and T. Miyasaka, "Organometal halide perovskites as visible-light sensitizers for photovoltaic cells," *Journal of the American Chemical Society*, vol. 131, no. 17, pp. 6050–6051, 2009. PMID: 19366264.

[9] Science News, "Newcomer juices up the race to harness sunlight," *Science*, vol. 342, p. 1438, 2013.

[10] Feature News, "365 days: the year in science," *Nature*, vol. 504, p. 357, 2013.

[11] W. S. Yang, J. H. Noh, N. J. Jeon, Y. C. Kim, S. Ryu, J. Seo, and S. I. Seok, "High-performance photovoltaic perovskite layers fabricated through intramolecular exchange," *Science*, vol. 348, no. 6240, pp. 1234–1237, 2015.

[12] E. Becquerel, "Mémoire sur les effets électriques produits sous l'influence des rayons solaires," *Comptes Rendus*, vol. 9, p. 561, 1839.

[13] J. Nelson, *The Physics of Solar Cells*. Imperial College press, 2003.

[14] W. Shockley and H. J. Queisser, "Detailed balance limit of efficiency of p-n junction solar cells," *Journal of Applied Physics*, vol. 32, no. 3, pp. 510–519, 1961.

[15] F. Dimroth, T. N. D. Tibbits, M. Niemeyer, F. Predan, P. Beutel, C. Karcher, E. Oliva, G. Siefer, D. Lackner, P. Fuß-Kailuweit, A. W. Bett, R. Krause, C. Drazek, E. Guiot, J. Wasselin, A. Tauzin, and T. Signamarcheix, "Four-junction wafer-bonded concentrator solar cells," *IEEE Journal of Photovoltaics*, vol. 6, pp. 343–349, Jan 2016.

[16] M. Green, *Third Generation Photovoltaics: Advanced Solar Energy Conversion*. Physics and astronomy online library, Springer, 2003.

[17] D. König, K. Casalenuovo, Y. Takeda, G. Conibeer, J. Guillemoles, R. Patterson, L. Huang, and M. Green, "Hot carrier solar cells: Principles, materials and design," *Physica E: Low-dimensional Systems and Nanostructures*, vol. 42, no. 10, pp. 2862 – 2866, 2010. 14th International Conference on Modulated Semiconductor Structures.

[18] Y. Okada, N. J. Ekins-Daukes, T. Kita, R. Tamaki, M. Yoshida, A. Pusch, O. Hess, C. C. Phillips, D. J. Farrell, K. Yoshida, N. Ahsan, Y. Shoji, T. Sogabe, and J.-F. Guillemoles, "Intermediate band solar cells: Recent progress and future directions," *Applied Physics Reviews*, vol. 2, no. 2, p. 021302, 2015.

[19] K. T. Butler, M. P. W. E. Lamers, A. W. Weeber, and J. H. Harding, "Molecular dynamics studies of the bonding properties of amorphous silicon nitride coatings on crystalline silicon," *Journal of Applied Physics*, vol. 110, no. 12, p. 124905, 2011.

[20] M. W. Lamers, K. T. Butler, J. H. Harding, and A. Weeber, "Interface properties of a-SiNx:H/Si to improve surface passivation," *Solar Energy Materials and Solar Cells*, vol. 106, pp. 17 – 21, 2012. SiliconPV.

[21] V. M. Fthenakis, H. C. Kim, and E. Alsema, "Emissions from photovoltaic life cycles," *Environmental Science & Technology*, vol. 42, no. 6, pp. 2168–2174, 2008. PMID: 18409654.

[22] H. J. Snaith, "Perovskites: The emergence of a new era for low-cost, high-efficiency solar cells," *The Journal of Physical Chemistry Letters*, vol. 4, no. 21, pp. 3623–3630, 2013.

[23] J.-H. Im, C.-R. Lee, S.-W. Lee, Jin-Wook and, and N.-G. Park, "6.5% efficient perovskite quantum-dot-sensitized solar cell," *Nanoscale*, vol. 3, pp. 4088–4093, 2011.

[24] H.-S. Kim, J.-W. Lee, N. Yantara, P. P. Boix, S. A. Kulkarni, S. Mhaisalkar, M. GrÃd̓tzel, and N.-G. Park, "High efficiency solid-state sensitized solar cell-based on submicrometer rutile tio2 nanorod and $CH_3NH_3PbI_3$ perovskite sensitizer," *Nano Letters*, vol. 13, no. 6, pp. 2412–2417, 2013. PMID: 23672481.

[25] M. M. Lee, J. Teuscher, T. Miyasaka, T. N. Murakami, and H. J. Snaith, "Efficient hybrid solar cells based on meso-superstructured organometal halide perovskites," *Science*, vol. 338, no. 6107, pp. 643–647, 2012.

[26] J. H. Heo, S. H. Im, J. H. Noh, T. N. Mandal, C.-S. Lim, J. A. Chang, Y. H. Lee, H.-j. Kim, A. Sarkar, N. K., M. Gratzel, and S. I. Seok, "Efficient inorganic-organic hybrid heterojunction solar cells containing perovskite compound and polymeric hole conductors," *Nat Photon*, vol. 7, pp. 486–491, Jun 2013. Article.

[27] M. Liu, M. B. Johnston, and H. J. Snaith, "Efficient planar heterojunction perovskite solar cells by vapour deposition," *Nature*, vol. 501, pp. 395–398, Sep 2013. Letter.

[28] K. Xiong, W. Liu, S. J. Teat, L. An, H. Wang, T. J. Emge, and J. Li, "New hybrid lead iodides: From one-dimensional chain to two-dimensional layered perovskite structure," *Journal of Solid State Chemistry*, vol. 230, pp. 143 – 148, 2015.

[29] D. B. Mitzi, K. Liang, and S. Wang, "Synthesis and characterization of $[NH_2C(I)NH_2]_2ASnI_5$ with a = iodoformamidinium or formamidinium: The chemistry of

cyanamide and tin(ii) iodide in concentrated aqueous hydriodic acid solutions," *Inorganic Chemistry*, vol. 37, no. 2, pp. 321–327, 1998.

[30] L. Dou, A. B. Wong, Y. Yu, M. Lai, N. Kornienko, S. W. Eaton, A. Fu, C. G. Bischak, J. Ma, T. Ding, N. S. Ginsberg, L.-W. Wang, A. P. Alivisatos, and P. Yang, "Atomically thin two-dimensional organic-inorganic hybrid perovskites," *Science*, vol. 349, no. 6255, pp. 1518–1521, 2015.

[31] L. Wang, K. Wang, and B. Zou, "Pressure-induced structural and optical properties of organometal halide perovskite-based formamidinium lead bromide," *The Journal of Physical Chemistry Letters*, vol. 7, no. 13, pp. 2556–2562, 2016. PMID: 27321024.

[32] K. A. Müller, W. Berlinger, and F. Waldner, "Characteristic structural phase transition in perovskite-type compounds," *Phys. Rev. Lett.*, vol. 21, pp. 814–817, Sep 1968.

[33] R. D. Shannon, "Revised effective ionic radii and systematic studies of interatomic distances in halides and chalcogenides," *Acta Crystallographica Section A*, vol. 32, pp. 751–767, Sep 1976.

[34] V. M. Goldschmidt, "Die gesetze der krystallochemie," *Naturwissenschaften*, vol. 14, no. 21, pp. 477–485, 1926.

[35] E. K. H. Salje, M. C. Gallardo, J. Jiménez, F. J. Romero, and J. del Cerro, "The cubic-tetragonal phase transition in strontium titanate: excess specific heat measurements and evidence for a near-tricritical, mean field type transition mechanism," *Journal of Physics: Condensed Matter*, vol. 10, no. 25, p. 5535, 1998.

[36] M. Johnsson and P. Lemmens, *Crystallography and Chemistry of Perovskites*. John Wiley & Sons Ltd, 2007.

[37] M. Yashima and R. Ali", "Structural phase transition and octahedral tilting in the calcium titanate perovskite catio$_3$," *Solid State Ionics*, vol. 180, no. "2 - 3", pp. 120 – 126, 2009.

[38] A. Kudo and Y. Miseki, "Heterogeneous photocatalyst materials for water splitting," *Chem. Soc. Rev.*, vol. 38, pp. 253–278, 2009.

[39] T. He, Q. Huang, A. P. Ramirez, Y. Wang, K. A. Regan, N. Rogado, M. A. Hayward, M. K. Haas, J. S. Slusky, K. Inumara, H. W. Zandbergen, N. P. Ong, and R. J. Cava, "Superconductivity in the non-oxide perovskite mgcni3," *Nature*, vol. 411, pp. 54–56, May 2001.

[40] G. Xing, N. Mathews, S. S. Lim, N. Yantara, X. Liu, D. Sabba, M. Grätzel, S. Mhaisalkar, and T. C. Sum, "Low-temperature solution-processed wavelength-tunable perovskites for lasing," *Nat Mater*, vol. 13, pp. 476–480, May 2014. Letter.

[41] K.-I. Kobayashi, T. Kimura, H. Sawada, K. Terakura, and Y. Tokura, "Room-temperature magnetoresistance in an oxide material with an ordered double-perovskite structure," *Nature*, vol. 395, pp. 677–680, Oct 1998.

[42] S. Nagane, U. Bansode, O. Game, S. Chhatre, and S. Ogale, "$CH_3NH_3PbI_{(3-x)}(BF_4)_x$: molecular ion substituted hybrid perovskite," *Chem. Commun.*, vol. 50, pp. 9741–9744, 2014.

[43] E. Mosconi, A. Amat, M. K. Nazeeruddin, M. GrÃČâĆňtzel, and F. De Angelis, "First-principles modeling of mixed halide organometal perovskites for photovoltaic applications," *The Journal of Physical Chemistry C*, vol. 117, no. 27, pp. 13902–13913, 2013.

[44] N. Pellet, P. Gao, G. Gregori, T.-Y. Yang, M. K. Nazeeruddin, J. Maier, and M. Grätzel, "Mixed-organic-cation perovskite photovoltaics for enhanced solar-light harvesting," *Angewandte Chemie International Edition*, vol. 53, no. 12, pp. 3151–3157, 2014.

[45] H. L. Wells, "über die cäsium- und kalium-bleihalogenide," *Zeitschrift fÃijr anorganische Chemie*, vol. 3, no. 1, pp. 195–210, 1893.

[46] C. K. MOLLER, "Crystal structure and photoconductivity of caesium plumbohalides," *Nature*, vol. 182, pp. 1436–1436, Nov 1958.

[47] D. Z. Weber, "$CH_3NH_3SnBr_xI_{3-x}$ (x = 0 - 3) , ein sn(ii)-system mit kubischer perowskitstruktur," *Naturforsch*, vol. 33b, pp. 862–865, 1998.

[48] D. Z. Weber, "NH_3CH_3PbX3, ein pb(ii)-system mit kubische perowskitstruktur," *Naturforsch*, vol. 33b, pp. 1443–1445, 1998.

[49] D. Yang, J. Lv, X. Zhao, Q. Xu, Y. Fu, Y. Zhan, A. Zunger, and L. Zhang, "Functionality-directed screening of pb-free hybrid organic-inorganic perovskites with desired intrinsic photovoltaic functionalities," *Chemistry of Materials*, vol. 29, no. 2, pp. 524–538, 2017.

[50] W. Travis, E. N. K. Glover, H. Bronstein, D. O. Scanlon, and R. G. Palgrave, "On the application of the tolerance factor to inorganic and hybrid halide perovskites: a revised system," *Chem. Sci.*, vol. 7, pp. 4548–4556, 2016.

[51] G. Kieslich, S. Sun, and A. K. Cheetham, "Solid-state principles applied to organic-inorganic perovskites: new tricks for an old dog," *Chem. Sci.*, vol. 5, pp. 4712–4715, 2014.

[52] C. C. Stoumpos, L. Frazer, D. J. Clark, Y. S. Kim, S. H. Rhim, A. J. Freeman, J. B. Ketterson, J. I. Jang, and M. G. Kanatzidis, "Hybrid germanium iodide perovskite semiconductors: Active lone pairs, structural distortions, direct and indirect energy gaps, and strong nonlinear optical properties," *Journal of the American Chemical Society*, vol. 137, no. 21, pp. 6804–6819, 2015. PMID: 25950197.

[53] W.-J. Xu, K.-P. Xie, Z.-F. Xiao, W.-X. Zhang, and X.-M. Chen, "Controlling two-step phase transitions and dielectric responses by a-site cations in two perovskite-like coordination polymers," *Crystal Growth & Design*, vol. 16, no. 12, pp. 7212–7217, 2016.

[54] J. M. Frost, K. T. Butler, F. Brivio, C. H. Hendon, M. van Schilfgaarde, and A. Walsh, "Atomistic origins of high-performance in hybrid halide perovskite solar cells," *Nano Letters*, vol. 14, no. 5, pp. 2584–2590, 2014. PMID: 24684284.

[55] K. X. Steirer, P. Schulz, G. Teeter, V. Stevanovic, M. Yang, K. Zhu, and J. J. Berry, "Defect tolerance in methylammonium lead triiodide perovskite," *ACS Energy Letters*, vol. 1, no. 2, pp. 360–366, 2016.

[56] W.-J. Yin, T. Shi, and Y. Yan, "Unusual defect physics in ch3nh3pbi3 perovskite solar cell absorber," *Applied Physics Letters*, vol. 104, no. 6, p. 063903, 2014.

[57] W.-J. Yin, T. Shi, and Y. Yan, "Unusual defect physics in ch3nh3pbi3 perovskite solar cell absorber," *Applied Physics Letters*, vol. 104, no. 6, p. 063903, 2014.

[58] E. L. Unger, E. T. Hoke, C. D. Bailie, W. H. Nguyen, A. R. Bowring, T. Heumuller, M. G. Christoforo, and M. D. McGehee, "Hysteresis and transient behavior in current-voltage measurements of hybrid-perovskite absorber solar cells," *Energy Environ. Sci.*, vol. 7, pp. 3690–3698, 2014.

[59] J. Burschka, N. Pellet, S.-J. Moon, R. Humphry-Baker, P. Gao, M. K. Nazeeruddin, and M. Grätzel, "Sequential deposition as a route to high-performance perovskite-sensitized solar cells," *Nature*, vol. 499, pp. 316–319, Jul 2013. Letter.

[60] B. Yang, O. Dyck, J. Poplawsky, J. Keum, A. Puretzky, S. Das, I. Ivanov, C. Rouleau, G. Duscher, D. Geohegan, and K. Xiao, "Perovskite solar cells with near 100% internal quantum efficiency based on large single crystalline grains and vertical bulk heterojunctions," *Journal of the American Chemical Society*, vol. 137, no. 29, pp. 9210–9213, 2015. PMID: 26156790.

[61] M. T. Weller, O. J. Weber, P. F. Henry, A. M. Di Pumpo, and T. C. Hansen, "Complete structure and cation orientation in the perovskite photovoltaic methylammonium lead iodide between 100 and 352 k," *Chem. Commun.*, vol. 51, pp. 4180–4183, 2015.

[62] T. Baikie, Y. Fang, J. M. Kadro, M. Schreyer, F. Wei, S. G. Mhaisalkar, M. Graetzel, and T. J. White, "Synthesis and crystal chemistry of the hybrid perovskite $(CH_3NH_3)PbI_3$,"

[63] S. A. Kulkarni, T. Baikie, P. P. Boix, N. Yantara, N. Mathews, and S. Mhaisalkar, "Band-gap tuning of lead halide perovskites using a sequential deposition process," *J. Mater. Chem. A*, vol. 2, pp. 9221–9225, 2014.

[64] E. L. Unger, A. R. Bowring, C. J. Tassone, V. L. Pool, A. Gold-Parker, R. Cheacharoen, K. H. Stone, E. T. Hoke, M. F. Toney, and M. D. McGehee, "Chloride in lead chloride-derived organo-metal halides for perovskite-absorber solar cells," *Chemistry of Materials*, vol. 26, no. 24, pp. 7158–7165, 2014.

[65] A. M. A. Leguy, J. M. Frost, A. P. McMahon, V. G. Sakai, W. Kockelmann, C. Law, X. Li, F. Foglia, A. Walsh, B. C. O'Regan, J. Nelson, J. T. Cabral, and P. R. F. Barnes, "The dynamics of methylammonium ions in hybrid organic-inorganic perovskite solar cells," *Nature Communications*, vol. 6, p. 7124, 2015.

[66] M. T. Weller, O. J. Weber, J. M. Frost, and A. Walsh, "Cubic perovskite structure of black formamidinium lead iodide, α-$[HC(NH_2)_2]PbI_3$, at 298 k," *The Journal of Physical Chemistry Letters*, vol. 6, no. 16, pp. 3209–3212, 2015.

[67] C. Roldan-Carmona, P. Gratia, I. Zimmermann, G. Grancini, P. Gao, M. Graetzel, and M. K. Nazeeruddin, "High efficiency methylammonium lead triiodide perovskite solar cells: the relevance of non-stoichiometric precursors," *Energy Environ. Sci.*, vol. 8, pp. 3550–3556, 2015.

[68] Y. Bi, E. M. Hutter, Y. Fang, Q. Dong, J. Huang, and T. J. Savenije, "Charge carrier lifetimes exceeding 15μs in methylammonium lead iodide single crystals," *The Journal of Physical Chemistry Letters*, vol. 7, no. 5, pp. 923–928, 2016. PMID: 26901658.

[69] Q. Dong, Y. Fang, Y. Shao, P. Mulligan, J. Qiu, L. Cao, and J. Huang, "Electron-hole diffusion lengths $>$ 175 μm in solution-grown $CH_3NH_3PbI_3$ single crystals," *Science*, vol. 347, no. 6225, pp. 967–970, 2015.

[70] Q. Dong, Y. Fang, Y. Shao, P. Mulligan, J. Qiu, L. Cao, and J. Huang, "Electron-hole diffusion lengths $>$ 175 Îijm in solution-grown ch3nh3pbi3 single crystals," *Science*, vol. 347, no. 6225, pp. 967–970, 2015.

[71] F. Hao, C. C. Stoumpos, D. H. Cao, R. P. H. Chang, and M. G. Kanatzidis, "Lead-free solid-state organic-inorganic halide perovskite solar cells," *Nat Photon*, vol. 8, pp. 489–494, Jun 2014. Article.

[72] Y. Takahashi, H. Hasegawa, Y. Takahashi, and T. Inabe, "Hall mobility in tin iodide perovskite ch3nh3sni3: Evidence for a doped semiconductor," *Journal of Solid State Chemistry*, vol. 205, pp. 39 – 43, 2013.

[73] G. E. Eperon, S. D. Stranks, C. Menelaou, M. B. Johnston, L. M. Herz, and H. J. Snaith, "Formamidinium lead trihalide: a broadly tunable perovskite for efficient planar heterojunction solar cells," *Energy Environ. Sci.*, vol. 7, pp. 982–988, 2014.

[74] A. Amat, E. Mosconi, E. Ronca, C. Quarti, P. Umari, M. K. Nazeeruddin, M. Grätzel, and F. De Angelis, "Cation-induced band-gap tuning in organohalide perovskites: Interplay

of spin-orbit coupling and octahedra tilting," *Nano Letters*, vol. 14, no. 6, pp. 3608–3616, 2014. PMID: 24797342.

[75] C. C. Stoumpos, C. D. Malliakas, and M. G. Kanatzidis, "Semiconducting tin and lead iodide perovskites with organic cations: Phase transitions, high mobilities, and near-infrared photoluminescent properties," *Inorganic Chemistry*, vol. 52, no. 15, pp. 9019–9038, 2013. PMID: 23834108.

[76] B. Conings, J. Drijkoningen, N. Gauquelin, A. Babayigit, J. D'Haen, L. D'Olieslaeger, A. Ethirajan, J. Verbeeck, J. Manca, E. Mosconi, F. D. Angelis, and H.-G. Boyen, "Intrinsic thermal instability of methylammonium lead trihalide perovskite," *Advanced Energy Materials*, vol. 5, no. 15, pp. 1500477–n/a, 2015. 1500477.

[77] S. Colella, E. Mosconi, P. Fedeli, A. Listorti, F. Gazza, F. Orlandi, P. Ferro, T. Besagni, A. Rizzo, G. Calestani, G. Gigli, F. De Angelis, and R. Mosca, "$MAPbI_{3-x}Cl_x$ mixed halide perovskite for hybrid solar cells: The role of chloride as dopant on the transport and structural properties," *Chemistry of Materials*, vol. 25, no. 22, pp. 4613–4618, 2013.

[78] K. Cao, H. Li, S. Liu, J. Cui, Y. Shen, and M. Wang, ""$MAPbI_{3-x}Br_x$ mixed halide perovskites for fully printable mesoscopic solar cells with enhanced efficiency and less hysteresis"," *"Nanoscale"*, vol. "8", pp. "8839–8846", "2016".

[79] B. A. Rosales, L. Men, S. D. Cady, M. P. Hanrahan, A. J. Rossini, and J. Vela, "Persistent dopants and phase segregation in organolead mixed-halide perovskites," *Chemistry of Materials*, vol. 28, no. 19, pp. 6848–6859, 2016.

[80] N.-G. Park, "Perovskite solar cells: an emerging photovoltaic technology," *Materials Today*, vol. 18, no. 2, pp. 65 – 72, 2015.

[81] M. Saliba, T. Matsui, J.-Y. Seo, K. Domanski, J.-P. Correa-Baena, M. K. Nazeeruddin, S. M. Zakeeruddin, W. Tress, A. Abate, A. Hagfeldt, and M. Gratzel, "Cesium-containing triple cation perovskite solar cells: improved stability, reproducibility and high efficiency," *Energy Environ. Sci.*, vol. 9, pp. 1989–1997, 2016.

[82] N. J. Jeon, J. H. Noh, W. S. Yang, Y. C. Kim, S. Ryu, J. Seo, and S. I. Seok, "Compositional engineering of perovskite materials for high-performance solar cells," *Nature*, vol. 517, pp. 476–480, Jan 2015. Letter.

[83] F. Hao, C. C. Stoumpos, R. P. H. Chang, and M. G. Kanatzidis, "Anomalous band gap behavior in mixed sn and pb perovskites enables broadening of absorption spectrum in solar cells," *Journal of the American Chemical Society*, vol. 136, no. 22, pp. 8094–8099, 2014. PMID: 24823301.

[84] J. "Liu, G. Wang, Z. Song, X. He, K. Luo, Q. Ye, C. Liao, and J. Mei, ""$FAPb_{1-x}Sn_xI_3$ mixed metal halide perovskites with improved light harvesting and stability for efficient planar heterojunction solar cells"," *"J. Mater. Chem. A"*, vol. "5", pp. "9097–9106", "2017".

[85] L. Zhang and P. H.-L. Sit, "Ab initio study of interaction of water, hydroxyl radicals, and hydroxide ions with $CH_3NH_3PbI_3$ and $CH_3NH_3PbBr_3$ surfaces," *The Journal of Physical Chemistry C*, vol. 119, no. 39, pp. 22370–22378, 2015.

[86] J. S. Manser, M. I. Saidaminov, J. A. Christians, O. M. Bakr, and P. V. Kamat, "Making and breaking of lead halide perovskites," *Accounts of Chemical Research*, vol. 49, no. 2, pp. 330–338, 2016. PMID: 26789596.

[87] K. Domanski, J.-P. Correa-Baena, N. Mine, M. K. Nazeeruddin, A. Abate, M. Saliba, W. Tress, A. Hagfeldt, and M. Grätzel, "Not all that glitters is gold: Metal-migration-induced degradation in perovskite solar cells," *ACS Nano*, vol. 10, no. 6, pp. 6306–6314, 2016. PMID: 27187798.

[88] N. Ashcroft and N. Mermin, *Solid State Physics*. Brooks Cole, 1976.

[89] R. M. Martin, *Electronic Structure: Basic Theory and Practical Methods*. Cambridge, 2008.

[90] R. G. Parr and W. Yang, *Density Functional Theory of Atoms and Molecules*. Oxford, 1989.

[91] M. Born and R. Oppenheimer, "Zur quantentheorie der molekeln," *Annalen der Physik*, vol. 389, no. 20, pp. 457–484, 1927.

[92] J. M. Combes, P. Duclos, and R. Seiler, *The Born-Oppenheimer Approximation*, pp. 185–213. Boston, MA: Springer US, 1981.

[93] C. Kittel, *Introduction to solid state physics*. Wiley, 1953.

[94] P. Hohenberg and W. Kohn, "Inhomogeneous electron gas," *Phys. Rev.*, vol. 136, pp. B864–B871, Nov 1964.

[95] W. Kohn and L. J. Sham, "Self-consistent equations including exchange and correlation effects," *Phys. Rev.*, vol. 140, pp. A1133–A1138, Nov 1965.

[96] E. Brémond, M. Savarese, N. Q. Su, A. J. Pérez-Jiménez, X. Xu, J. C. Sancho-García, and C. Adamo, "Benchmarking density functionals on structural parameters of small-/medium-sized organic molecules," *Journal of Chemical Theory and Computation*, vol. 12, no. 2, pp. 459–465, 2016. PMID: 26730741.

[97] M. Levy, J. P. Perdew, and V. Sahni, "Exact differential equation for the density and ionization energy of a many-particle system," *Phys. Rev. A*, vol. 30, pp. 2745–2748, Nov 1984.

[98] V. I. Anisimov and Y. A. Izyumov, *Electronic Structure of Strongly Correlated Materials*. Springer, 2010.

[99] J. P. Perdew, J. A. Chevary, S. H. Vosko, K. A. Jackson, M. R. Pederson, D. J. Singh, and C. Fiolhais, "Atoms, molecules, solids, and surfaces: Applications of the generalized gradient approximation for exchange and correlation," *Phys. Rev. B*, vol. 46, pp. 6671–6687, Sep 1992.

[100] D. C. Langreth and M. J. Mehl, "Beyond the local-density approximation in calculations of ground-state electronic properties," *Phys. Rev. B*, vol. 28, pp. 1809–1834, Aug 1983.

[101] J. Heyd, G. E. Scuseria, and M. Ernzerhof, "Hybrid functionals based on a screened coulomb potential," *The Journal of Chemical Physics*, vol. 118, no. 18, pp. 8207–8215, 2003.

[102] K. Kim and K. D. Jordan, "Comparison of density functional and mp2 calculations on the water monomer and dimer," *The Journal of Physical Chemistry*, vol. 98, no. 40, pp. 10089–10094, 1994.

[103] N. Ferré, M. Filatov, and M. Huix-Rotllant, *Density-Functional Methods for Excited States*. Springer, 2015.

[104] G. Strinati, “"application of the green's functions method to the study of the optical properties of semiconductors",” *"La Rivista del Nuovo Cimento (1978-1999)"*, vol. "11", no. "12", pp. "1–86", "1988".

[105] L. Hedin and S. Lundqvist, “Effects of electron-electron and electron-phonon interactions on the one-electron states of solids,” in *Solid State Physics* (D. T. Frederick Seitz and H. Ehrenreich, eds.), vol. 23 of *Solid State Physics*, pp. 1 – 181, Academic Press, 1970.

[106] L. Hedin, “New method for calculating the one-particle green's function with application to the electron-gas problem,” *Phys. Rev.*, vol. 139, pp. A796–A823, Aug 1965.

[107] C. D. Valentin, S. Botti, and M. Cococcioni, *First Principles Approaches to Spectroscopic Properties of Complex Materials*. Springer, 2014.

[108] D. Bohm and D. Pines, “A collective description of electron interactions. i. magnetic interactions,” *Phys. Rev.*, vol. 82, pp. 625–634, Jun 1951.

[109] D. Pines and D. Bohm, “A collective description of electron interactions: Ii. collective vs individual particle aspects of the interactions,” *Phys. Rev.*, vol. 85, pp. 338–353, Jan 1952.

[110] D. Bohm and D. Pines, “A collective description of electron interactions: Iii. coulomb interactions in a degenerate electron gas,” *Phys. Rev.*, vol. 92, pp. 609–625, Nov 1953.

[111] A. Stan, N. E. Dahlen, and R. van Leeuwen, “Levels of self-consistency in the gw approximation,” *The Journal of Chemical Physics*, vol. 130, no. 11, p. 114105, 2009.

[112] M. van Schilfgaarde, T. Kotani, and S. Faleev, “Quasiparticle self-consistent *gw* theory,” *Phys. Rev. Lett.*, vol. 96, p. 226402, Jun 2006.

[113] T. Kotani, M. van Schilfgaarde, and S. V. Faleev, “Quasiparticle self-consistent *gw* method: A basis for the independent-particle approximation,” *Phys. Rev. B*, vol. 76, p. 165106, Oct 2007.

[114] M. Cardona and P. Y. Yu, *Fundamentals of Semiconductors*. Springer, 1995.

[115] R. Winkler, *Origin of Spin-Orbit Coupling Effects*. Springer, 2003.

[116] E. Rashba, "Properties of semiconductors with an extremum loop. 1. cyclotron and combinational resonance in a magnetic field perpendicular to the plane of the loop," *Sov. Phys. Solid State*, vol. 2, pp. 1109–1122, 1960.

[117] Y. A. Bychkov and E. I. Rasbha, "Properties of a 2d electron gas with lifted spectral degeneracy," *P. Zh. Eksp. Teor. Fiz.*, vol. 39, p. 66, 1984.

[118] D. Awschalom, D. Loss, and N. Samarth, *Semiconductor Spintronics and Quantum Computation*. Springer, 2002.

[119] J. S. Toll, "Causality and the dispersion relation: Logical foundations," *Phys. Rev.*, vol. 104, pp. 1760–1770, Dec 1956.

[120] R. Asahi, W. Mannstadt, and A. J. Freeman, "Optical properties and electronic structures of semiconductors with screened-exchange lda," *Phys. Rev. B*, vol. 59, pp. 7486–7492, Mar 1999.

[121] R. Del Sole and R. Girlanda, "Optical properties of semiconductors within the independent-quasiparticle approximation," *Phys. Rev. B*, vol. 48, pp. 11789–11795, Oct 1993.

[122] F. Brivio, A. B. Walker, and A. Walsh, "Structural and electronic properties of hybrid perovskites for high-efficiency thin-film photovoltaics from first-principles," *APL Materials*, vol. 1, no. 4, p. 042111, 2013.

[123] K. T. Butler, J. M. Frost, and A. Walsh, "Band alignment of the hybrid halide perovskites $CH_3NH_3PbCl_3$, $CH_3NH_3PbBr_3$ and $CH_3NH_3PbI_3$," *Mater. Horiz.*, vol. 2, pp. 228–231, 2015.

[124] J. Perdew, A. Ruzsinszky, G. Csonka, O. Vydrov, G. Scuseria, L. Constantin, X. Zhou, and K. Burke, "Restoring the density-gradient expansion for exchange in solids and surfaces," *Physical Review Letters*, vol. 100, 4 2008.

[125] G. Kresse and J. Furthmüller, "Efficient iterative schemes for ab initio total-energy calculations using a plane-wave basis set," *Phys. Rev. B*, vol. 54, pp. 11169–11186, Oct 1996.

[126] Questaal package, "`https://www.questaal.org`," 2017. [Online; accessed 9-July-2017].

[127] W. Setyawan and S. Curtarolo, "High-throughput electronic band structure calculations: Challenges and tools," *Computational Materials Science*, vol. 49, no. 2, pp. 299 – 312, 2010.

[128] F. Brivio, K. T. Butler, A. Walsh, and M. van Schilfgaarde, "Relativistic quasiparticle self-consistent electronic structure of hybrid halide perovskite photovoltaic absorbers," *Phys. Rev. B*, vol. 89, p. 155204, Apr 2014.

[129] A. Filippetti, P. Delugas, and A. Mattoni, "Radiative recombination and photoconversion of methylammonium lead iodide perovskite by first principles: Properties of an inorganic semiconductor within a hybrid body," *The Journal of Physical Chemistry C*, vol. 118, no. 43, pp. 24843–24853, 2014.

[130] E. Mosconi, A. Amat, M. K. Nazeeruddin, M. GrÃđtzel, and F. De Angelis, "First-principles modeling of mixed halide organometal perovskites for photovoltaic applications," *The Journal of Physical Chemistry C*, vol. 117, no. 27, pp. 13902–13913, 2013.

[131] A. Mattoni, A. Filippetti, M. I. Saba, and P. Delugas, "Methylammonium rotational dynamics in lead halide perovskite by classical molecular dynamics: The role of temperature," *The Journal of Physical Chemistry C*, vol. 119, no. 30, pp. 17421–17428, 2015.

[132] F. Brivio, J. M. Frost, J. M. Skelton, A. J. Jackson, O. J. Weber, M. T. Weller, A. R. Goñi, A. M. A. Leguy, P. R. F. Barnes, and A. Walsh, "Lattice dynamics and vibrational spectra of the orthorhombic, tetragonal, and cubic phases of methylammonium lead iodide," *Phys. Rev. B*, vol. 92, p. 144308, Oct 2015.

[133] C. Quarti, E. Mosconi, J. M. Ball, V. D'Innocenzo, C. Tao, S. Pathak, H. J. Snaith, A. Petrozza, and F. De Angelis, "Structural and optical properties of methylammonium lead iodide across the tetragonal to cubic phase transition: implications for perovskite solar cells," *Energy Environ. Sci.*, vol. 9, pp. 155–163, 2016.

[134] T. Dittrich, C. Awino, P. Prajongtat, B. Rech, and M. C. Lux-Steiner, "Temperature dependence of the band gap of ch3nh3pbi3 stabilized with pmma: A modulated surface

photovoltage study," *The Journal of Physical Chemistry C*, vol. 119, no. 42, pp. 23968–23972, 2015.

[135] J. M. Frost, K. T. Butler, and A. Walsh, "Molecular ferroelectric contributions to anomalous hysteresis in hybrid perovskite solar cells," *APL Materials*, vol. 2, no. 8, p. 081506, 2014.

[136] K. Tanaka, T. Takahashi, T. Ban, T. Kondo, K. Uchida, and N. Miura", ""comparative study on the excitons in lead-halide-based perovskite-type crystals {$CH_3NH3PbBr_3$} {$CH_3NH3PbI_3$} "," *"Solid State Communications "*, vol. "127", no. "9 - 10", pp. "619 – 623", "2003". "".

[137] L. Leppert, S. E. Reyes-Lillo, and J. B. Neaton, "Electric field- and strain-induced rashba effect in hybrid halide perovskites," *The Journal of Physical Chemistry Letters*, vol. 7, no. 18, pp. 3683–3689, 2016. PMID: 27577732.

[138] S. De Wolf, J. Holovsky, S.-J. Moon, P. Löper, B. Niesen, M. Ledinsky, F.-J. Haug, J.-H. Yum, and C. Ballif, "Organometallic halide perovskites: Sharp optical absorption edge and its relation to photovoltaic performance," *The Journal of Physical Chemistry Letters*, vol. 5, no. 6, pp. 1035–1039, 2014. PMID: 26270984.

[139] M. Rohlfing and S. G. Louie, "Electron-hole excitations and optical spectra from first principles," *Phys. Rev. B*, vol. 62, pp. 4927–4944, Aug 2000.

[140] A. Miyata, A. Mitioglu, P. Plochocka, O. Portugall, J. T.-W. Wang, S. D. Stranks, H. J. Snaith, and R. J. Nicholas, "Direct measurement of the exciton binding energy and effective masses for charge carriers in organic-inorganic tri-halide perovskites," *Nat Phys*, vol. 11, pp. 582–587, Jul 2015. Article.

[141] K. Galkowski, A. Mitioglu, A. Miyata, P. Plochocka, O. Portugall, G. E. Eperon, J. T.-W. Wang, T. Stergiopoulos, S. D. Stranks, H. J. Snaith, and R. J. Nicholas, "Determination of the exciton binding energy and effective masses for methylammonium and formamidinium lead tri-halide perovskite semiconductors," *Energy Environ. Sci.*, vol. 9, pp. 962–970, 2016.

[142] J. Even, L. Pedesseau, and C. Katan, "Analysis of multivalley and multibandgap absorption and enhancement of free carriers related to exciton screening in hybrid perovskites," *The Journal of Physical Chemistry C*, vol. 118, no. 22, pp. 11566–11572, 2014.

[143] N. Sestu, M. Cadelano, V. Sarritzu, F. Chen, D. Marongiu, R. Piras, M. Mainas, F. Quochi, M. Saba, A. Mura, and G. Bongiovanni, "Absorption f-sum rule for the exciton binding energy in methylammonium lead halide perovskites," *The Journal of Physical Chemistry Letters*, vol. 6, no. 22, pp. 4566–4572, 2015. PMID: 26517760.

[144] A. Kumar, N. K. Kumawat, P. Maheshwari, and D. Kabra, "Role of halide anion on exciton binding energy and disorder in hybrid perovskite semiconductors," in *2015 IEEE 42nd Photovoltaic Specialist Conference (PVSC)*, pp. 1–4, June 2015.

[145] J. S. Manser and P. V. Kamat, "Band filling with free charge carriers in organometal halide perovskites," *Nat Photon*, vol. 8, pp. 737–743, Sep 2014. Article.

[146] J. A. Christians, J. S. Manser, and P. V. Kamat, "Multifaceted excited state of $CH_3NH_3PbI_3$. charge separation, recombination, and trapping," *The Journal of Physical Chemistry Letters*, vol. 6, no. 11, pp. 2086–2095, 2015. PMID: 26266507.

[147] D. Shi, V. Adinolfi, R. Comin, M. Yuan, E. Alarousu, A. Buin, Y. Chen, S. Hoogland, A. Rothenberger, K. Katsiev, Y. Losovyj, X. Zhang, P. A. Dowben, O. F. Mohammed, E. H. Sargent, and O. M. Bakr, "Low trap-state density and long carrier diffusion in organolead trihalide perovskite single crystals," *Science*, vol. 347, no. 6221, pp. 519–522, 2015.

[148] S. D. Stranks, V. M. Burlakov, T. Leijtens, J. M. Ball, A. Goriely, and H. J. Snaith, "Recombination kinetics in organic-inorganic perovskites: Excitons, free charge, and subgap states," *Phys. Rev. Applied*, vol. 2, p. 034007, Sep 2014.

[149] S. D. Stranks, G. E. Eperon, G. Grancini, C. Menelaou, M. J. P. Alcocer, T. Leijtens, L. M. Herz, A. Petrozza, and H. J. Snaith, "Electron-hole diffusion lengths exceeding 1 micrometer in an organometal trihalide perovskite absorber," *Science*, vol. 342, no. 6156, pp. 341–344, 2013.

[150] E. M. Hutter, M. C. Gelvez-Rueda, A. Osherov, V. Bulovic, F. C. Grozema, S. D. Stranks, and T. J. Savenije, "Direct-indirect character of the bandgap in methylammonium lead iodide perovskite," *Nat Mater*, vol. 16, pp. 115–120, Jan 2017. Article.

[151] T. Trupke, M. A. Green, P. Würfel, P. P. Altermatt, A. Wang, J. Zhao, and R. Corkish, "Temperature dependence of the radiative recombination coefficient of intrinsic crystalline silicon," *Journal of Applied Physics*, vol. 94, no. 8, pp. 4930–4937, 2003.

[152] W. Gerlach, H. Schlangenotto, and H. Maeder, "On the radiative recombination rate in silicon," *physica status solidi (a)*, vol. 13, no. 1, pp. 277–283, 1972.

[153] J. M. Ball, M. M. Lee, A. Hey, and H. J. Snaith, "Low-temperature processed meso-superstructured to thin-film perovskite solar cells," *Energy Environ. Sci.*, vol. 6, pp. 1739–1743, 2013.

[154] S. Sun, T. Salim, N. Mathews, M. Duchamp, C. Boothroyd, G. Xing, T. C. Sum, and Y. M. Lam, "The origin of high efficiency in low-temperature solution-processable bilayer organometal halide hybrid solar cells," *Energy Environ. Sci.*, vol. 7, pp. 399–407, 2014.

[155] Y. Yamada, T. Nakamura, M. Endo, A. Wakamiya, and Y. Kanemitsu, "Photocarrier recombination dynamics in perovskite ch3nh3pbi3 for solar cell applications," *Journal of the American Chemical Society*, vol. 136, no. 33, pp. 11610–11613, 2014. PMID: 25075458.

[156] M. B. Johnston and L. M. Herz, "Hybrid perovskites for photovoltaics: Charge-carrier recombination, diffusion, and radiative efficiencies," *Accounts of Chemical Research*, vol. 49, no. 1, pp. 146–154, 2016. PMID: 26653572.

[157] W. Shockley and W. T. Read, "Statistics of the recombinations of holes and electrons," *Phys. Rev.*, vol. 87, pp. 835–842, Sep 1952.

[158] R. N. Hall, "Electron-hole recombination in germanium," *Phys. Rev.*, vol. 87, pp. 387–387, Jul 1952.

[159] G. W. 't Hooft, "The radiative recombination coefficient of gaas from laser delay measurements and effective nonradiative carrier lifetimes," *Applied Physics Letters*, vol. 39, no. 5, pp. 389–390, 1981.

[160] P. J. Bishop, M. E. Daniels, B. K. Ridley, and K. Woodbridge, "Radiative recombination in gaas/al$_x$ga$_{1-x}$as quantum wells," *Phys. Rev. B*, vol. 45, pp. 6686–6691, Mar 1992.

[161] F. Stern, "Gain-current relation for gaas lasers with n-type and undoped active layers," *IEEE Journal of Quantum Electronics*, vol. 9, pp. 290–294, February 1973.

[162] C. H. Swartz, M. Edirisooriya, E. G. LeBlanc, O. C. Noriega, P. A. R. D. Jayathilaka, O. S. Ogedengbe, B. L. Hancock, M. Holtz, T. H. Myers, and K. N. Zaunbrecher, "Radiative and interfacial recombination in cdte heterostructures," *Applied Physics Letters*, vol. 105, no. 22, p. 222107, 2014.

[163] A. Kirk, M. Dinezza, S. Liu, X. Zhao, and Y. Zhang, *CdTe vs. GaAs solar cells - A modeling case study with preliminary experimental results*, pp. 2515–2517. Institute of Electrical and Electronics Engineers Inc., 2013.

[164] X.-H. Zhao, M. J. DiNezza, S. Liu, S. Lin, Y. Zhao, and Y.-H. Zhang, "Time-resolved and excitation-dependent photoluminescence study of cdte/mgcdte double heterostructures grown by molecular beam epitaxy," *Journal of Vacuum Science & Technology B, Nanotechnology and Microelectronics: Materials, Processing, Measurement, and Phenomena*, vol. 32, no. 4, p. 040601, 2014.

[165] V. Vedra, *Modern Foundations of Quantum Optics*. Imperial College Press, 2005.

[166] R. Loudon, *The Quantum Theory of Light*. Oxford, 2000.

[167] E. Kioupakis, Q. Yan, D. Steiauf, and C. G. V. de Walle, "Temperature and carrier-density dependence of auger and radiative recombination in nitride optoelectronic devices," *New Journal of Physics*, vol. 15, no. 12, p. 125006, 2013.

[168] R. L. Milot, G. E. Eperon, H. J. Snaith, M. B. Johnston, and L. M. Herz, "Temperature-dependent charge-carrier dynamics in $CH_3NH_3PbI_3$ perovskite thin films," *Advanced Functional Materials*, vol. 25, no. 39, pp. 6218–6227, 2015.

[169] M. Kepenekian, R. Robles, C. Katan, D. Sapori, L. Pedesseau, and J. Even, "Rashba and dresselhaus effects in hybrid organic-inorganic perovskites: From basics to devices," *ACS Nano*, vol. 9, no. 12, pp. 11557–11567, 2015. PMID: 26348023.

[170] M. Kim, J. Im, A. J. Freeman, J. Ihm, and H. Jin, "Switchable s = 1/2 and j = 1/2 rashba bands in ferroelectric halide perovskites," *Proceedings of the National Academy of Sciences*, vol. 111, no. 19, pp. 6900–6904, 2014.

[171] J. Li and P. M. Haney, "Optical spintronics in organic-inorganic perovskite photovoltaics," *Phys. Rev. B*, vol. 93, p. 155432, Apr 2016.

[172] J. Li and P. M. Haney, "Circular photogalvanic effect in organometal halide perovskite $CH_3NH_3PbI_3$," *Applied Physics Letters*, vol. 109, no. 19, p. 193903, 2016.

[173] H. Maaß, H. Bentmann, C. Seibel, C. Tusche, S. V. Eremeev, T. R. F. Peixoto, O. E. Tereshchenko, K. A. Kokh, E. V. Chulkov, J. Kirschner, and F. Reinert, "Spin-texture inversion in the giant rashba semiconductor bitei," vol. 7, pp. 11621 EP –, May 2016. Article.

[174] T. Etienne, E. Mosconi, and F. De Angelis, "Dynamical origin of the rashba effect in organohalide lead perovskites: A key to suppressed carrier recombination in perovskite solar cells?," *The Journal of Physical Chemistry Letters*, vol. 7, no. 9, pp. 1638–1645, 2016. PMID: 27062910.

[175] E. E. Salpeter and H. A. Bethe, "A relativistic equation for bound-state problems," *Phys. Rev.*, vol. 84, pp. 1232–1242, Dec 1951.

[176] A. Luque and A. Martí, "Increasing the efficiency of ideal solar cells by photon induced transitions at intermediate levels," *Phys. Rev. Lett.*, vol. 78, pp. 5014–5017, Jun 1997.

[177] S. Tomic, T. Sogabe, and Y. Okada, "Quantum dot array based intermediate band solar cell: Effect of light concentration," in *2015 IEEE 42nd Photovoltaic Specialist Conference (PVSC)*, pp. 1–3, June 2015.

[178] N. S. Beattie, P. See, G. Zoppi, P. M. Ushasree, M. Duchamp, I. Farrer, D. A. Ritchie, and S. TomiÄĞ, "Quantum engineering of inas/gaas quantum dot based intermediate band solar cells," *ACS Photonics*, vol. 4, no. 11, pp. 2745–2750, 2017.

[179] J. T. Sullivan, C. B. Simmons, T. Buonassisi, and J. J. Krich, "Targeted search for effective intermediate band solar cell materials," *IEEE Journal of Photovoltaics*, vol. 5, pp. 212–218, Jan 2015.

[180] J. M. Frost, P. Azarhoosh, S. McKechnie, M. van Schilfgaarde, and A. Walsh, "A photon ratchet route to high-efficiency hybrid halide perovskite intermediate band solar cells,"

[181] S. Tomić, "Intermediate-band solar cells: Influence of band formation on dynamical processes in inas/gaas quantum dot arrays," *Phys. Rev. B*, vol. 82, p. 195321, Nov 2010.

[182] A. M. Ganose, K. T. Butler, A. Walsh, and D. O. Scanlon, "Relativistic electronic structure and band alignment of bisi and bisei: candidate photovoltaic materials," *J. Mater. Chem. A*, vol. 4, pp. 2060–2068, 2016.

[183] K. T. Butler, J. M. Frost, and A. Walsh, "Ferroelectric materials for solar energy conversion: photoferroics revisited," *Energy Environ. Sci.*, vol. 8, pp. 838–848, 2015.

[184] K. T. Butler, S. McKechnie, P. Azarhoosh, M. van Schilfgaarde, D. O. Scanlon, and A. Walsh, "Quasi-particle electronic band structure and alignment of the v-vi-vii semiconductors sbsi, sbsbr, and sbsei for solar cells," *Applied Physics Letters*, vol. 108, no. 11, p. 112103, 2016.